POTENTIAL IMPACTS OF VERTICAL CABLE SEISMIC:

MODELING, RESOLUTION AND MULTIPLE ATTENUATION

A Thesis

by

RYAN JUSTIN WILSON

Submitted to the Office of Graduate Studies of
Texas A&M University
in partial fulfillment of the requirements for the degree of

MASTER OF SCIENCE

May 2002

Major Subject: Geophysics

POTENTIAL IMPACTS OF VERTICAL CABLE SEISMIC:

MODELING, RESOLUTION AND MULTIPLE ATTENUATION

A Thesis

by

RYAN JUSTIN WILSON

Submitted to Texas A&M University
in partial fulfillment of the requirements
for the degree of

MASTER OF SCIENCE

Approved as to style and content by:

_____	_____
Luc T. Ikelle (Chair of Committee)	Joel S. Watkins (Member)
_____	_____
David B. Burnett (Member)	Andrew Hajash, Jr. (Head of Department)

May 2002

Major Subject: Geophysics

ABSTRACT

Potential Impacts of Vertical Cable Seismic: Modeling, Resolution and Multiple Attenuation. (May 2002)

Ryan Justin Wilson, B.S., Western Michigan University

Chair of Advisory Committee: Dr. Luc T. Ikelle

Vertical cable seismic methods are becoming more relevant as we require high quality and high resolution seismic data in both land and marine environments. Our goal in this thesis is to demonstrate the impacts of vertical cable surveying in these areas.

Vertical cable methods have been applied to the marine environment with encouraging results. Data quality is similar to that of traditional towed-streamer data, without the long, cumbersome towed-streamers which are difficult to maneuver in congested areas. The current marine vertical cable processing schemes tend to use primaries and receiver ghosts of primaries for imaging. Therefore, we demonstrate the ability of the current multiple attenuation algorithms developed by Ikelle (2001) to preserve either primaries or the receiver ghosts of primaries.

As we focus on land acquisition, we discover that vertical cable surveying can overcome many of the traditional problems of land seismics. In fact, our investigations lead us to believe that problems such as ground roll, guided waves and statics can be avoided almost entirely using vertical cable acquisition methods. Furthermore, land

vertical surveying is naturally suited for multi-component acquisition and time-lapse surveying.

To fully analyze the applicability of vertical cable surveys in marine and land environments, we also investigate the problem of cable spacing and sampling within each cable. We compare the resolution of vertical cable data and horizontal data by calculating the maximum angular coverage of each acquisition geometry and measuring the occurrence of each angle within this coverage, such that more occurrences means better resolution. From our investigations, we find that by using vertical cables of no more than 500 m in length at 500 m intervals, we can acquire higher resolution seismic data relative to horizontal surface methods for an image point, horizontal reflector or a dipping reflector.

The key tool used in these investigations is fully elastic finite-difference modeling. We chose this technique based on its ability to properly and accurately model the full wavefield through complex models, all the while preserving amplitudes and the phase of reflected, diffracted and converted wavefields.

To Ezra Schaibly, may I follow in your footsteps and make you proud.

ACKNOWLEDGMENTS

I would like to take this opportunity to directly thank Dr. Luc T. Ikelle, chair of my committee, for his constant guidance and encouragement throughout my research. His time and efforts are greatly appreciated.

I would also like to express my gratitude to my committee members, Dr. Joel Watkins and Mr. David Burnett, for their engaging comments and valuable time.

I probably would not be writing this if it were not for the constant support from my family. Foremost, I would like to thank my wife, who took care of not only Grayling and myself, but also everything else. My parents and brother were also instrumental in my capacity to complete and compile this thesis successfully. And last, but not least, the rest of my family and friends, many thanks to you all.

I wish to thank the former and current CASP members who provided technical support and fond memories and all the sponsors of the CASP project that made this and other research possible.

TABLE OF CONTENTS

CHAPTER Page

CHAPTER Page

LIST OF FIGURES

FIGURE Page

FIGURE Page

FIGURE Page

FIGURE Page

FIGURE Page

LIST OF TABLES

TABLE Page

CHAPTER I

INTRODUCTION

MOTIVATION AND OBJECTIVES

Exploration and production of hydrocarbons are becoming increasingly more difficult as we pursue reservoirs in more geologically complex areas. New seismic acquisition technologies like vertical cable surveying are required to compliment existing ones. Furthermore, as seismic is being used more and more in production environments, including areas congested by offshore drilling and other production facilities, the vertical cable acquisition geometry which does not require towing streamers offers an attractive alternative to the current technology.

Vertical cable acquisition first took hold in the marine setting. Works done by Havig and Krail (1996), Krail (1997,1994), Leach (1999), and Ward (1997) stimulated interest in vertical cable surveying by demonstrating that high quality marine seismic data can be obtained from vertical cable acquisition methods. However, the impact of this technology for marine exploration and production is yet to be fully established. Some components of the processing flow of vertical cable data are still open to debate. For instance, the problem of multiple attenuation will need to be re-addressed for the vertical cable geometry. We will propose a solution here.

This thesis follows the style and format of Geophysics.

In addition to adapting the current processing flow to vertical cable, it is important to analyze the issues of resolution associated with vertical cable coverage. We will conduct this resolution analysis in this thesis.

As mentioned earlier, vertical cable acquisition was originally designed for the marine environment. However, we discover during our investigations for this thesis, that applications of vertical cable surveying can have even more drastic impacts on seismic data quality in the land environment. In this thesis, we will demonstrate that problems such as groundroll and other guided wave energy which tend to dominate land seismic data and complicate its processing can be avoided altogether by adequately selecting the position of the cables and receivers. Furthermore, multi-component data can be easily recorded, making land vertical cable an attractive solution compared to surface land acquisition. These two issues and others will be discussed to point out the potential impacts of vertical cables in land acquisition and processing.

In summary, our objectives of this thesis are three-fold:

1) We discuss relative resolutions of seismic imaging between vertical cable methods and traditional horizontal acquisition methods like towed streamer, ocean bottom cable and land surface seismic.

2) We demonstrate a method of attenuating multiples, receiver ghosts and/or primaries in vertical cable data.

3) We propose to extend vertical cable surveying to land and demonstrate that such acquisition can lead to high quality data by avoiding recording most of the groundroll energy.

SCOPE OF THIS THESIS

Finite-difference modeling

We will pursue the objectives outlined above in a multi-chapter approach. Our entire discussions and analysis are based on synthetic data generated by finite-difference methods (Madariaga, 1976; Virieux, 1984, 1986; Levander, 1988). Hence, we will begin by introducing our finite-difference modeling capabilities. Our software is based on the full elastic wave equations. We will demonstrate with some simple examples the capability of this software to accurately model primaries, multiples, converted wave energy, groundroll, and guided waves.

Vertical cable resolution vs. surface resolution

To fully analyze the applicability of vertical cable surveying, the fundamental problem of spacing between cables and sampling within the cable must be addressed. In Chapter III, we will discuss these sampling issues by posing the problem as that of finding the spacing between cables and the distribution of receivers within the cables which allows us to image at least as well as surface seismic surveying.

Multiple and receiver ghost attenuation of marine vertical cable data

As discussed earlier, the vertical cable geometry requires us to revisit the data processing, in particular, multiple attenuation of marine vertical cable data. This subject still requires strong attention as time and time again, multiples have plagued both the data processor and seismic interpreter. We begin by introducing the events we record in

seismic surveys and assign specific nomenclature. Primary and multiple events, as well as source and receiver ghosts are discussed, as the vertical cable geometry requires we treat these events in a different manner relative to the streamer survey. We then apply the current inverse scattering multiple attenuation algorithms discussed by Ikelle and Weglein, 1996; Ikelle, 1999; and Ikelle, 2001 to the vertical cable data. We follow with numeric examples generated using our finite-difference software to demonstrate the demultiple process.

Land vertical cable seismic

The inherent differences in marine and land settings lead us to a separate discussion of land vertical cable surveys. Traditionally land seismic data has been poor due to the near surface geologic conditions. Primarily, ground roll and other guided wave energy contribute significantly to the poor data quality often associated with land data. In Chapter V, we propose vertical cable surveying on land to overcome these problems.

More background information on vertical cable acquisition

Vertical cable seismic surveys involve multiple receiver arrays deployed in a vertical position. This geometry can be seen in Figure 1. In a marine setting, the vertical cables, equipped with hydrophones, are deployed in a grid pattern and anchored to the seafloor. A buoyancy sphere holds the receiver cables in the vertical position. Data is recorded on a recording buoy tethered to each cable. One or multiple

seismic vessels are used to generate seismic sources near the surface in a densely spaced grid pattern. A familiar vertical cable experiment involves a single vertical receiver array, namely, a vertical seismic profile survey (VSP). Thus, we will begin the discussion on vertical cable data by revisiting the familiar VSP experiment.

VSP surveys are typically conducted to obtain high-resolution seismic data around the borehole to compliment surface seismic data. Acquiring VSP data involves positioning a receiver array down into a borehole while initiating an energy source at the surface. Since the receivers in the VSP experiment are oriented vertically, the energy arriving at the sensors is classified as up-going or down-going energy or wavefields. A schematic of seismic events associated with the vertical receiver array illustrates this point in Figure 2. For a zero-offset VSP experiment, the direct wave traveling from the source to the receivers is the first event to arrive and is part of the down-going wavefield. Reflected energy arriving from interfaces below the receiver array is classified as part of the up-going wavefield. The events recorded on the seismogram will have opposite slopes corresponding to the up and down-going wavefields. Figure 3 is a shot gather generated from finite-difference modeling simulating a VSP experiment. The up-going wavefield corresponds to a positive slope and the down-going wavefield corresponds to a negative slope.

Vertical cable surveys can be considered a multi-survey, multi-offset VSP experiment. Figure 4 is a shot gather produced from finite-difference modeling simulating a 2D marine vertical cable survey utilizing four vertical cables. Each vertical

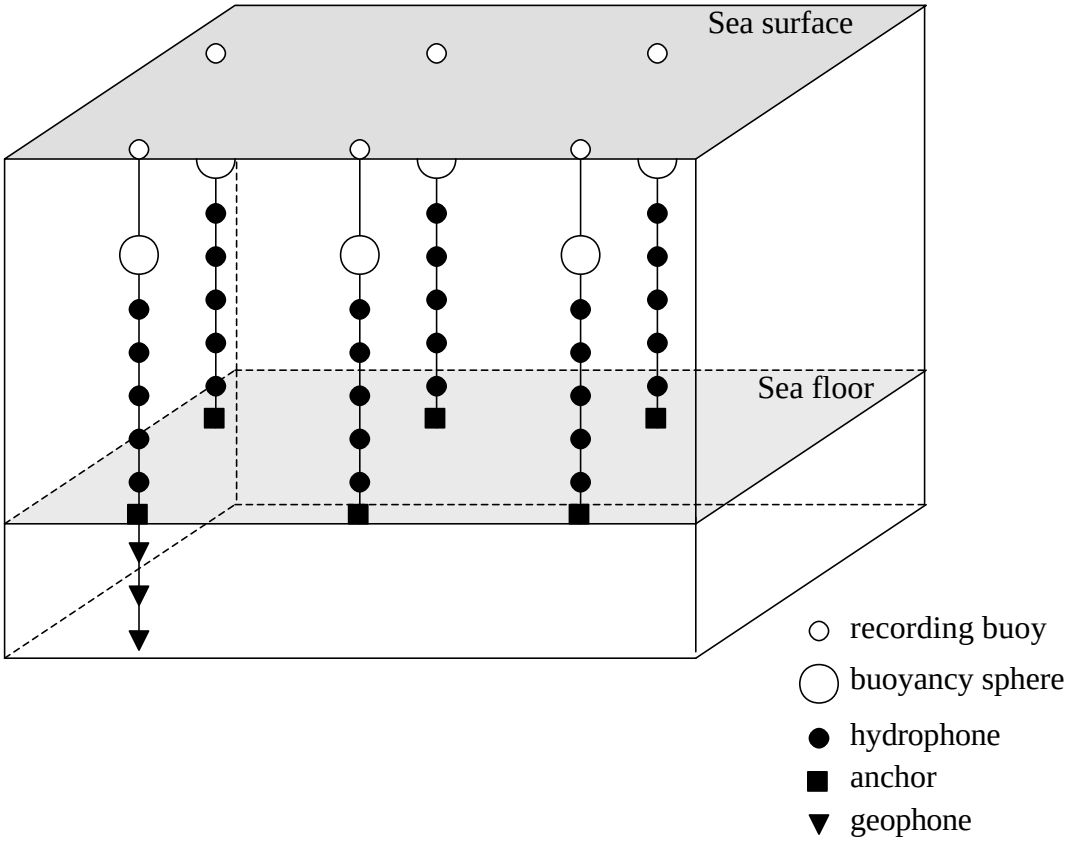

Figure 1. Vertical cable acquisition geometry. The cable to the left shows how geophones could be extended below the sea floor within boreholes.

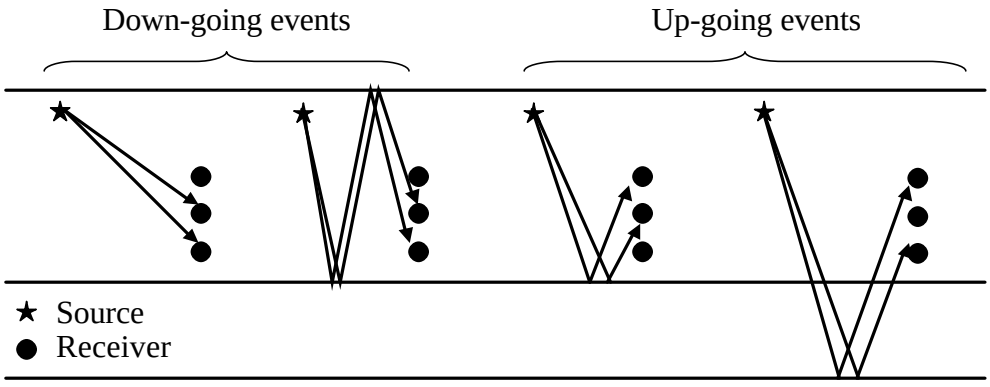

Figure 2. Raypaths associated with down-going and up-going events in a vertical receiver array experiment.

cable has 60 receivers, spanning from 125 to 496 m water depth. The receivers are located within the water column. Essentially, a single shot gather for a vertical cable survey is similar to four independent VSP surveys. Again, the down-going and up-going wavefields are clearly distinguishable on the seismograms.

The obvious difference between a VSP and vertical cable survey is the use of many vertical receiver arrays and the number and density of source positions. Furthermore, VSP surveys are typically a developmental seismic survey in which one is trying to calibrate surface data with well data immediately adjacent to the borehole. Vertical cable surveys are designed for large-scale exploration, just as streamer surveys are. Hence, it is desirable to make some comparisons of vertical cable surveying with surface methods.

The towed-streamer method has been the preferred choice of seismic data acquisition in marine environments. Figure 5 shows the geometry of the towed-streamer method. A seismic vessel tows multiple receiver cables or streamers. The seismic vessel sails parallel lines while firing an air gun array and recording seismic data. Since both the source and receivers are contained within the water column, only compressional waves are detected at the sensors, similar to marine vertical cable surveys. The difference between these acquisition geometries is their imaging resolution, or angular coverage from image points. This difference in vertical cable and streamer data imaging resolution are fully discussed in Chapter III.

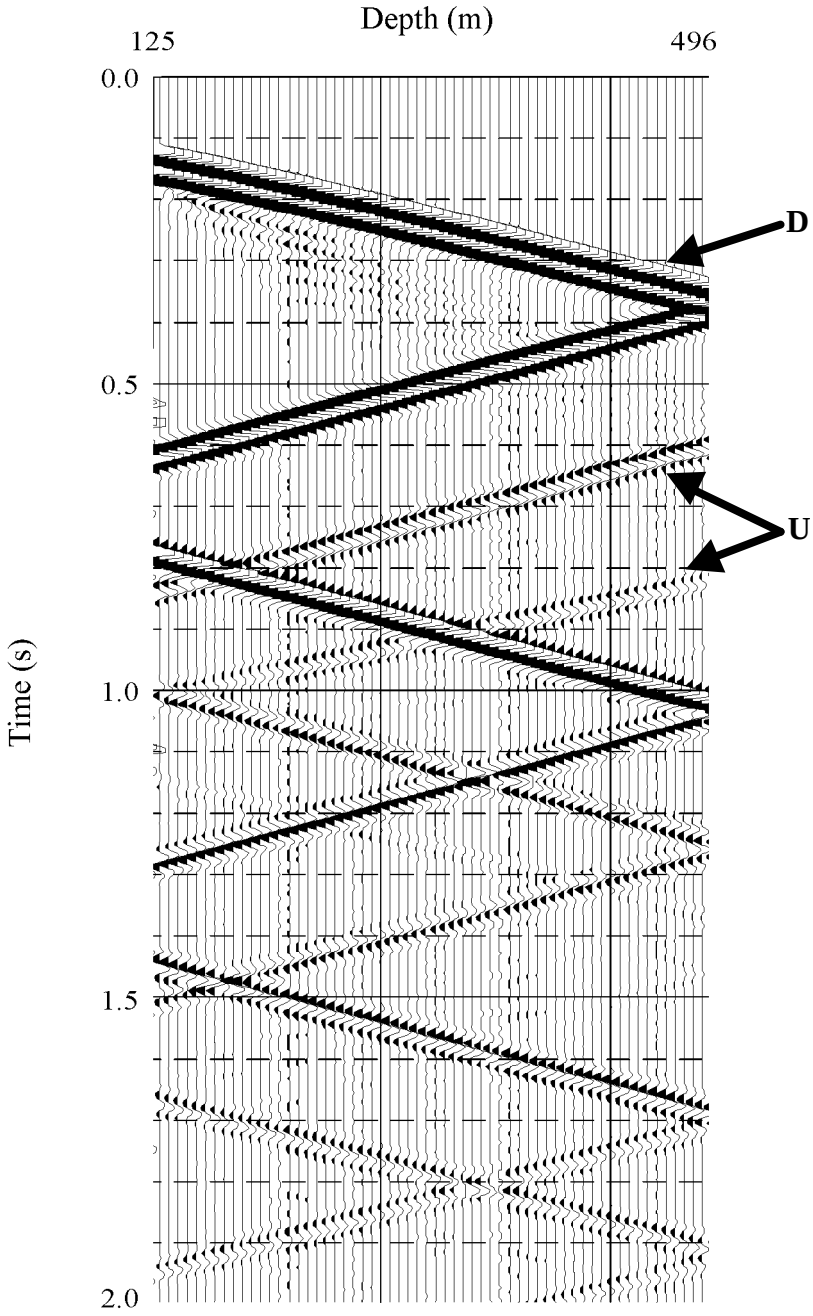

Figure 3. VSP shot gather. Up-going and down-going energy is clearly distinguishable. D denotes downgoing events and U denotes upgoing events.

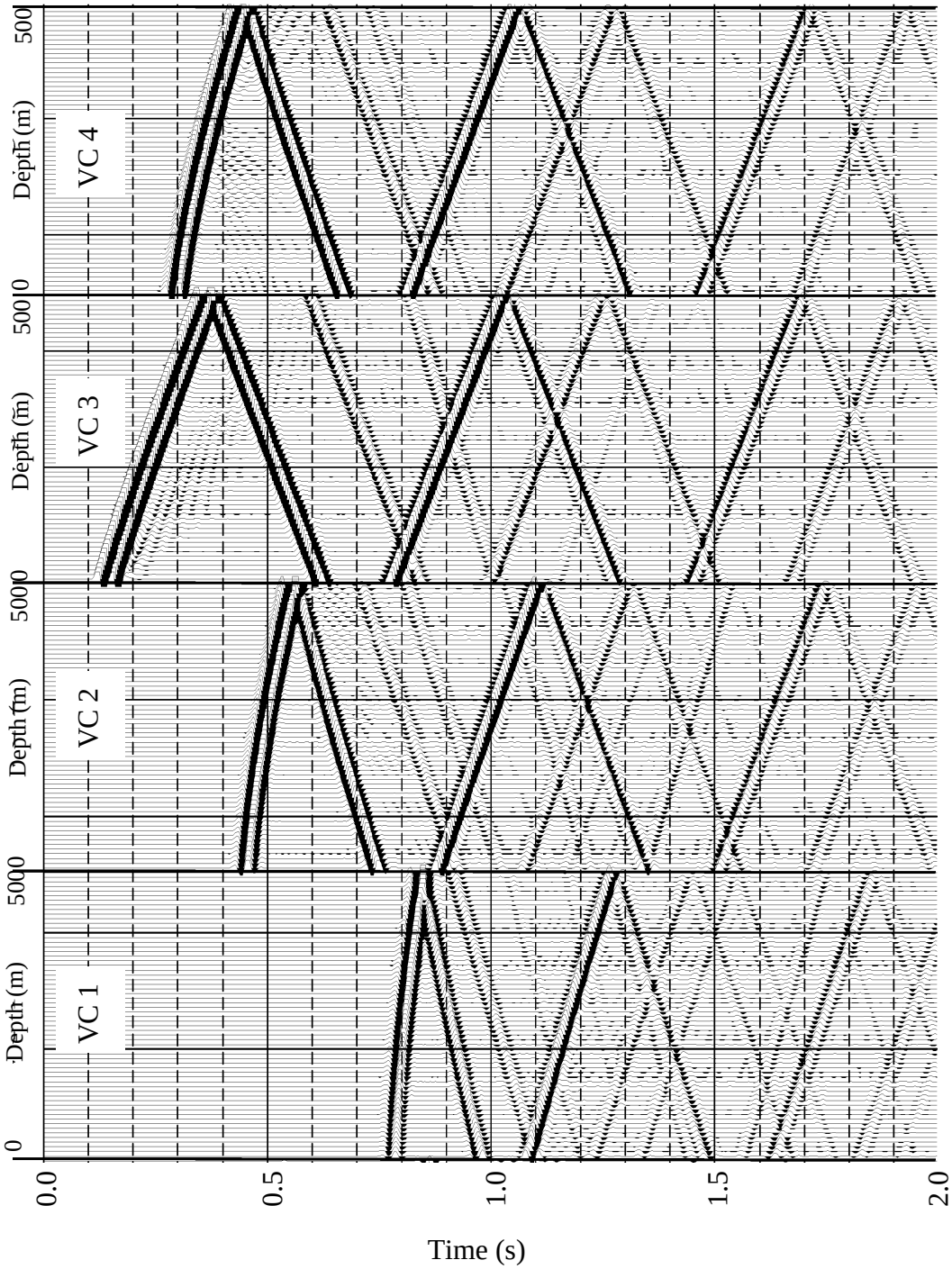

Figure 4. Shot gather simulating a vertical cable survey using four cables.

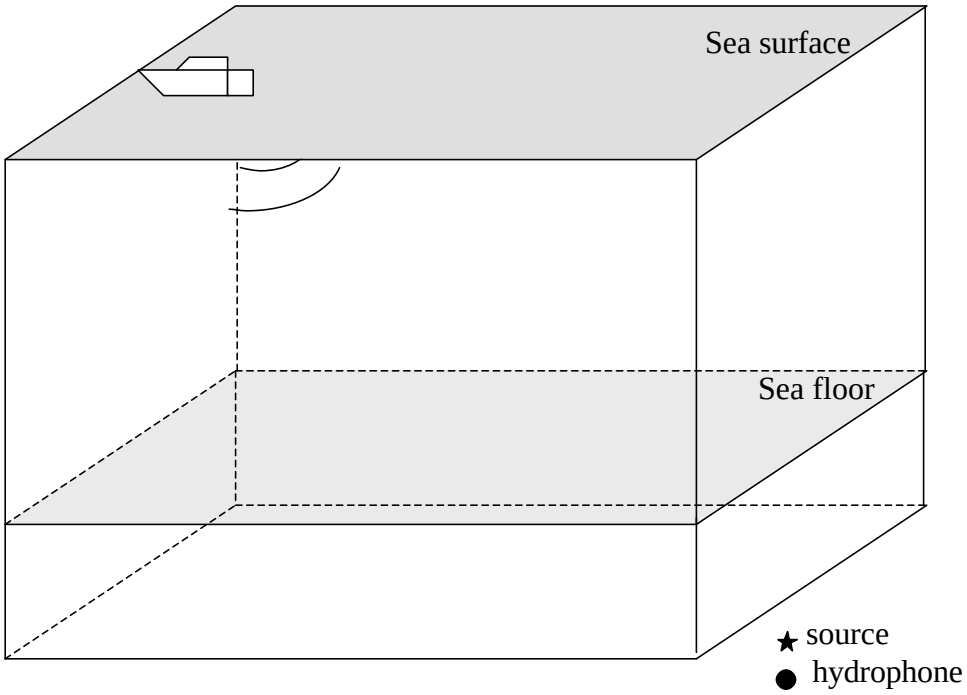

Figure 5. Traditional towed-streamer acquisition geometry. Only P-waves are generated and recorded.

CHAPTER II

FINITE-DIFFERENCE MODELING

INTRODUCTION

Several approaches to numerically modeling the seismic response of the earth exist. They range from reflectivity methods (e.g., Frasier, 1970), to ray tracing methods (e.g., Chapman, 1971), to finite-difference techniques (e.g. Madariaga, 1976; Virieux 1984, 1986; and Levander, 1988). The finite-difference techniques are by far most accurate way of simulating elastic wave propagation through complex media provided that the grid spacing is chosen properly; finite-difference modeling (FDM) can accurately predict travel times and amplitudes of primaries, multiples, converted waves and diffractions, and hence, closely simulate the real earth's response.

The finite-difference technique consists of solving partial differential equations which govern the wave motion. The derivatives are approximated by a truncated Taylor series whose accurateness depends essentially on the sampling of the geological model. Our objective in this chapter is to validate the accuracy of the CASP finite-difference software used throughout this thesis. We will start be recalling the wave equations and reviewing the finite-difference techniques.

Elastic wave equations

The elastic wave equations used in our finite-difference software are as follows:

$$r\,\frac{\partial u_t}{\partial t} = \frac{\partial t_{xx}}{\partial x} + \frac{\partial t_{xz}}{\partial z}, \qquad (1)$$

$$r\,\frac{\partial w_t}{\partial t} = \frac{\partial t_{zx}}{\partial x} + \frac{\partial t_{zz}}{\partial z}, \qquad (2)$$

$$t_{xx} = (l + 2m)\frac{\partial u}{\partial x} + l\,\frac{\partial w}{\partial z}, \qquad (3)$$

$$t_{zx} = m\left(\frac{\partial u}{\partial z} + \frac{\partial w}{\partial x}\right), \qquad (4)$$

and

$$t_{zz} = (l + 2m)\frac{\partial w}{\partial z} + l\,\frac{\partial u}{\partial x}. \qquad (5)$$

In these equations, u_t and w_t are the horizontal and vertical particle velocity respectively, u and w are the horizontal and vertical displacement components respectively, t_{xx}, t_{zx}, and t_{zz} are the stress tensors, r is the density, l and m are the Lame parameters. Notice that these equations require partial derivatives with respect to space and time. The finite-difference technique that we will discuss later essentially consists of approximating these derivatives The Lame parameters are related to P and S-wave velocities by

$$l = r\left(V_p^2 - 2V_s^2\right) \tag{6}$$

and

$$m = rV_s^2. \tag{7}$$

Poisson's ratio (s), which is a measure of rigidity, is given by

$$s = \frac{l}{2(l+m)}\ . \tag{8}$$

With the constraint that s varies only between 0.0 and 0.5, where low values corresponding to hard, rigid materials and high values corresponding to soft, unconsolidated materials. When V_s equals zero, as is the case for fluids, s equals 0.5.

FINITE-DIFFERENCE TECHNIQUES

The finite-difference method operates by replacing the derivatives in an equation by finite differences. If we consider a function, $f(x)$, its Taylor's Theorem expansion about x can be written as

$$f(x+h) = f(x) + hf'(x) + \frac{h^2}{2} f''(x) + \frac{h^3}{6} f'''(x) + \ldots, \tag{9}$$

or, alternatively,

$$f(x-h) = f(x) - hf'(x) + \frac{h^2}{2} f''(x) - \frac{h^3}{6} f'''(x) + \ldots \tag{10}$$

Here, h is the spatial increment. If h is small, the higher-order terms will become negligible. If we truncate the series in equations (9) and (10) after the third term, the first derivative of $f(x)$ can be solved by

$$f'(x) = \frac{1}{h}[f(x+h) - f(x)] - \frac{h}{2} f''(x_1) \qquad (11)$$

and

$$f'(x) = \frac{1}{h}[f(x) - f(x+h)] - \frac{h}{2} f''(x_2), \qquad (12)$$

respectively, where $\frac{h}{2} f''(x)$ is the truncation error term. Equations (3) and (4) lead to the finite-difference approximations

$$f'(x) \approx \frac{1}{h}[f(x+h) - f(x)] \qquad (13)$$

and

$$f'(x) \approx \frac{1}{h}[f(x) - f(x-h)] \qquad (14)$$

The expressions contained in the [] on the right hand side of equations (13) and (14) are called finite differences. Equations (13) and (14) are considered first-order accurate with an error of $O(h)$ because the truncation error term is first order with respect to *h*.

Alternatively, the truncation and subtraction of equations (9) and (10) yields

$$f'(x) = \frac{1}{2h}\left[f(x+h) - f(x-h) \right] - \frac{h^2}{6}\left[f'''(y) \right], \qquad (15)$$

where $y = x_1 + x_2$. This leads to the second-order approximation

$$f'(x) \approx \frac{1}{2h}[f(x+h) - f(x-h)], \qquad (16)$$

with error $O(h^2)$ (truncation error term is second order, h^2). This approximation is more precise and favorable compared to the approximations in equations (13) and (14). By

retaining terms in the Taylor expansion series, higher-order approximations are possible and precision increases. References to higher-order approximations can be visited in Bayliss et al. (1986), Dablain (1986), and Levander (1988).

Finite-difference implementation

Our FDM software which is based on the elastic wave equation requires finite-difference computations with respect to time and space. For the temporal derivatives, we use a second-order approximation given by

$$f'(t) \approx \frac{1}{2\Delta t}\left[f(t+\Delta t) - f(t-\Delta t)\right]. \qquad (17)$$

For the spatial derivatives, we use a fourth-order approximation given by

$$f'(x) \approx \frac{1}{2\Delta x}\left[f(x+\Delta x) - f(x-\Delta x)\right] - \frac{\Delta x^2}{6} f'''(x). \qquad (18)$$

This scheme is referred to as a $O(\Delta t^2, \Delta x^4)$, where Δt is the temporal increment and Δx is the spatial increment. Higher-order derivatives are possible because no terms of the spatial derivatives contain material properties. The material properties are defined at each location and scale the properties according to the above equations. Higher-order finite-difference approximations improve precision and reduce the spatial sampling necessary to accurately simulate wave propagation, therefore reducing computation time and memory requirements (Levander, 1988).

The finite-difference software uses a staggered grid in both space and time (Madariaga, 1976; Virieux 1984,1986), as seen in Figure 6, to update velocity and stress calculations. The points at which the stresses are specified are halfway between the

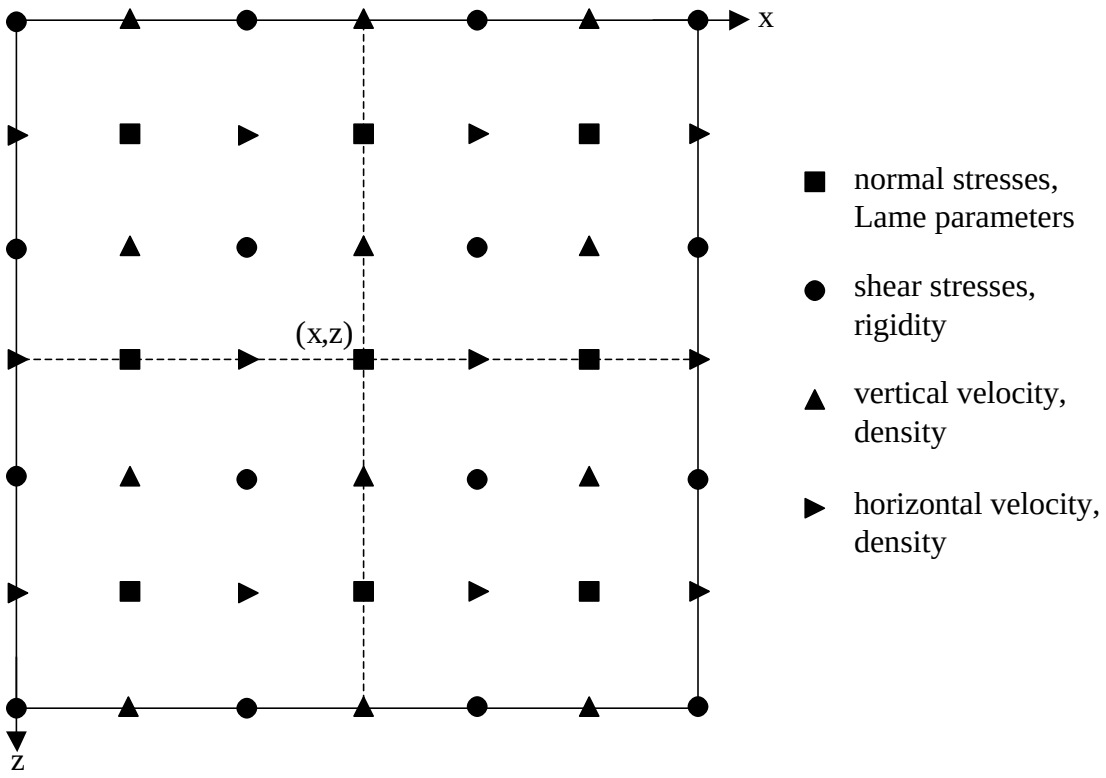

Figure 6. Finite-difference staggered grid used to update the velocity and stress calculations. The dashed line shows the vertical and horizontal velocity nodes used to update the stress calculation located at (x,z) (modified from Levander, 1988).

points at which the velocities are specified. So in one time step, both the velocity and stress component are updated. The spatial finite-difference is derived using four points adjacent to the location being updated. If the normal stress variable is being updated, the four adjacent velocity nodes are used (dashed line in Figure 6). This allows differences that are naturally centered at the required point.

The benefit of the staggered grid scheme which is used in our FDM software include (1) stability for all values of Poisson's ratio, (2) minimized grid dispersion and

grid anisotropy, (3) ability to simulate surface or buried sources, and (4) ability to simulate free-surface boundary conditions (see Levander (1988) for more discussions of these benefits).

NUMERICAL EXAMPLES

The ability to accurately simulate both travel times and amplitudes of direct waves, primary reflected waves, multiply reflected waves, converted waves, refracted waves and diffracted waves make FDM a valuable tool to geophysicists. To demonstrate the quality of our FDM software and its ability to handle complex media, we use a liquid over solid 90° corner-edge model, a solid over solid 90° corner-edge model, and a low velocity layer model as done in Kelly et al. (1976) and Virieux (1984; 1986). These models are chosen because they present a more complex wave pattern with step discontinuities that cause some modeling methods to break down. By demonstrating the ability of our fully elastic FDM software to properly simulate the wavefield in these simple models, we can justify the use of synthetic data to quantify the exploration potential of vertical cable surveying.

Liquid over solid 90° corner-edge model

Figure 7 shows the geometry of the corner-edge model and the corresponding media properties. We use an explosive source with a 30-hertz central frequency ricker wavelet as seen in Figure 8, for all modeling in this research. This means the stresses t_{xx} and t_{zz} expand spherically in (x,z) space. The source is located 1000 m from the side

boundaries and 250 m below the surface. Since we simulate an explosive source within a homogeneous medium, only compressional waves (P-waves) are generated. Seventy-three receivers (hydrophones which record pressure variations) are used at an interval spacing of 25 m. Each receiver is located 5 m below the surface. The top edge of the model simulates an air/water interface, or free-surface boundary, and the Kosloff absorbing sponge boundary conditions (Clayton and Engquist, 1977; Cerjan et. al., 1985) are used for the remaining three edges of the model. No internal boundary conditions are needed.

The wavefield snapshots in Figure 9 demonstrate the ability of the FDM software to properly retain amplitude patterns and phase relations in complex media. Snapshot A shows the compressional wavefield radiating from the explosive source at 120 ms. At 240 ms, snapshot B demonstrates the reflection from the free-surface and the advancing wavefield hitting the corner-edge. Snapshots C and D shows the reflection, diffraction, and refraction of the wavefield caused by the solid medium. Notice the compressional (P-waves) to shear wave (S-waves) conversion caused at the liquid-solid interface. Snapshot D shows the P and S-waves clearly decoupled at the interface and S-waves propagating through the lower medium. Note the ability of FDM to preserve amplitudes of diffracted and converted waves.

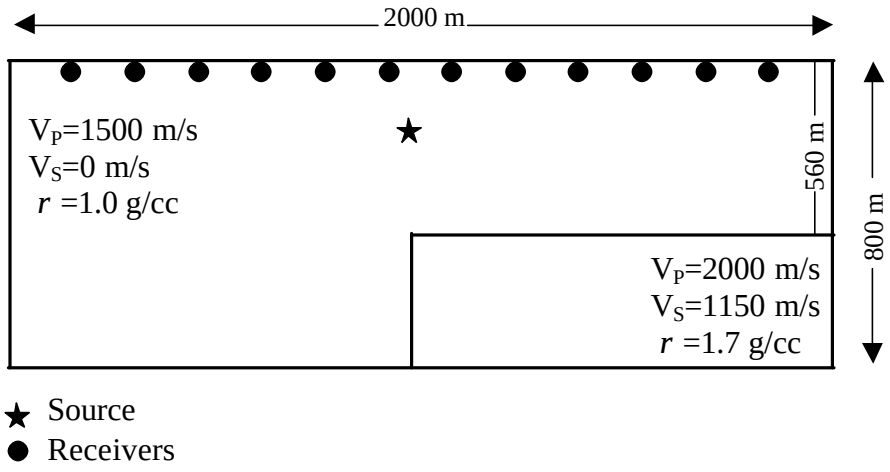

Figure 7. Liquid over solid corner-edge model used to generate synthetic seismograms and snapshots. The upper medium is acoustic with a free-surface upper boundary condition. Kosloff sponge is used at all other boundary conditions. The source is located 250 m below the surface.

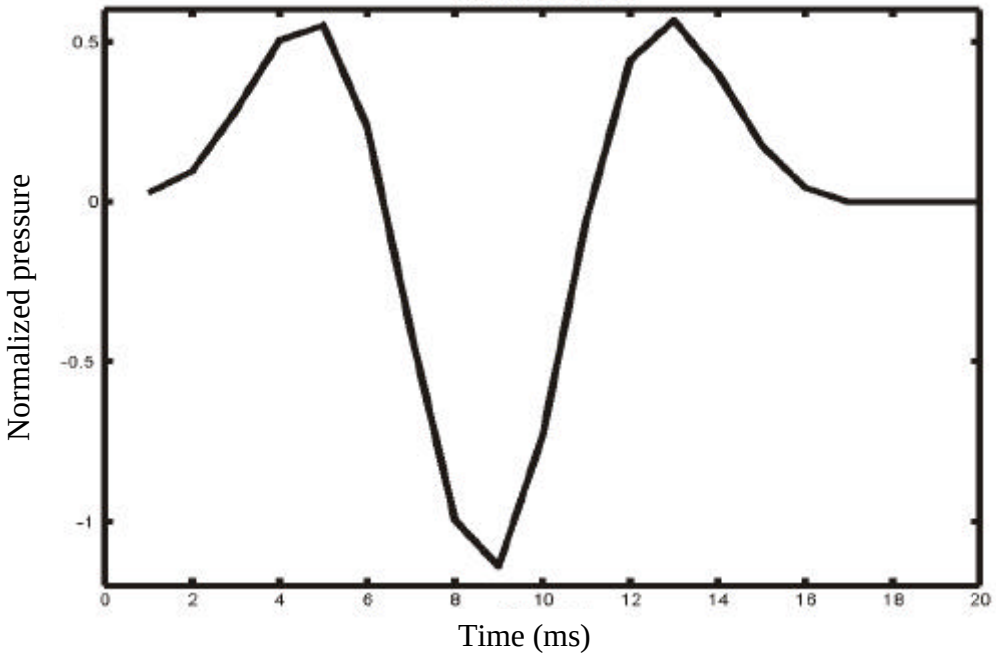

Figure 8. Source wavelet used to generate synthetic data.

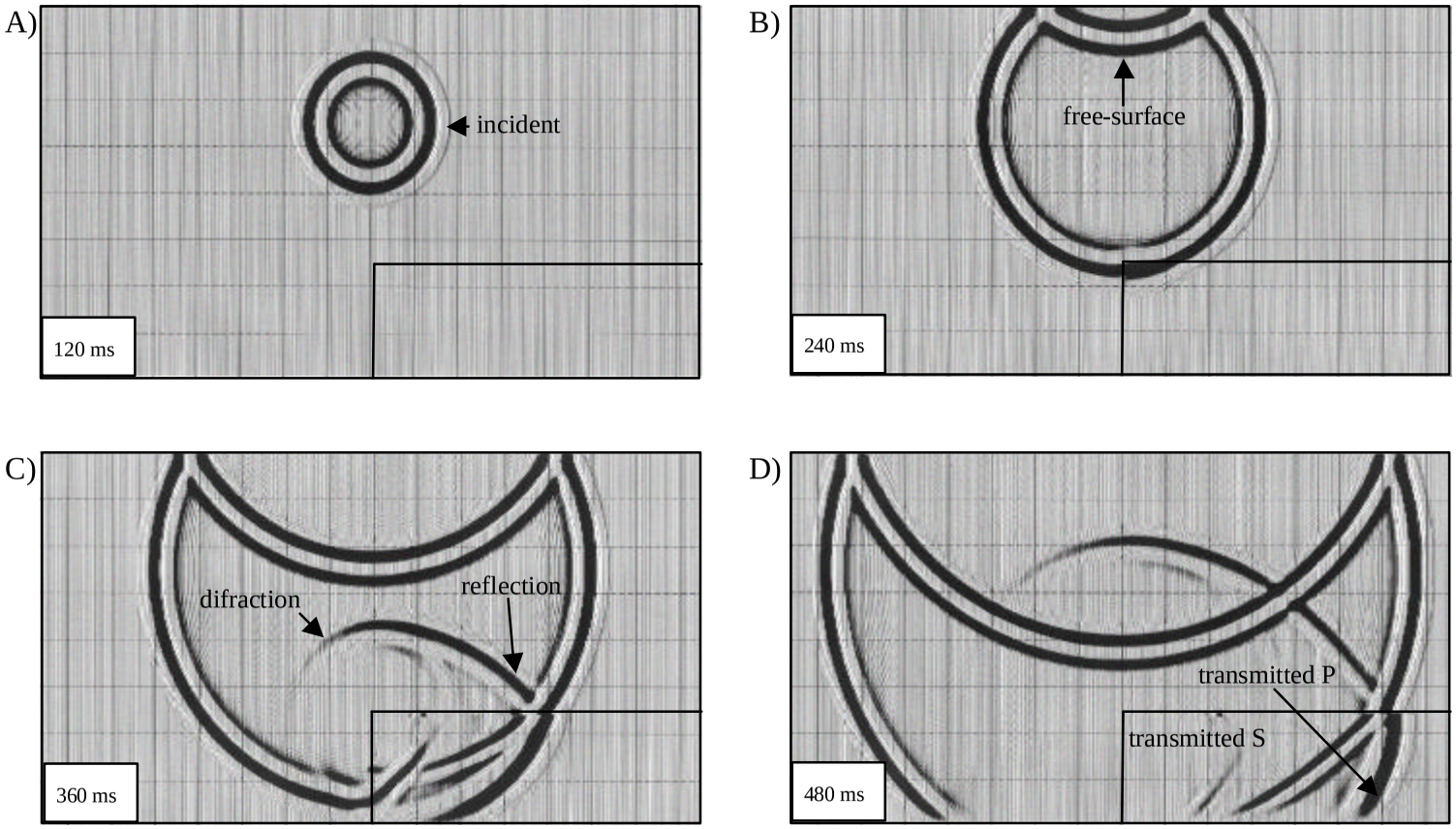

Figure 9. Snapshots showing wave propagation through liquid-over-solid 90° corner-edge model as seen in Figure 7. In snapshot A, the wavefield consists of the compressional wave radiating from the explosive source. Snapshot B shows the free-surface reflection and initial contact with the corner edge. Snapshots C and D show clear reflections from the solid media and the transmitted compressional and converted shear wavefront propagating through the solid medium. The pressure field is displayed here.

Figure 10 is the seismogram displaying the pressure field corresponding to the liquid over solid corner-edge model in Figure 7. The direct arrival (Figure 10, label D) is the energy that travels from the source directly to the receivers, with no reflections. The primary reflected wave (Figure 10, label PP1) corresponds to the energy which has experienced one upward reflection from the solid medium. The free-surface event (Figure 10, label FSE) corresponds to an event which has experienced a bounce at the air/water interface, or free surface. Notice there is a polarity reversal due to the presence of the free surface. Events PP1 and FSE have amplitude reductions associated with the diffracted wavefront generated at the sharp discontinuity at the corner-edge. Raypaths for these events are shown in Figure 11. The FDM software can accurately simulate the wavefield at these discontinuities, without any additional boundary conditions.

To check the accuracy of the FDM software, zero-offset travel times for each event were calculated using the equation $t_0=\Delta z/V_1$, where Δz is vertical distance traveled and V_1 is the P-wave velocity of the upper medium. Table 1 lists the zero-offset travel times for each event. The calculated travel times using this equation corresponds to the associated zero-offset events predicted by finite-difference modeling in Figure 10.

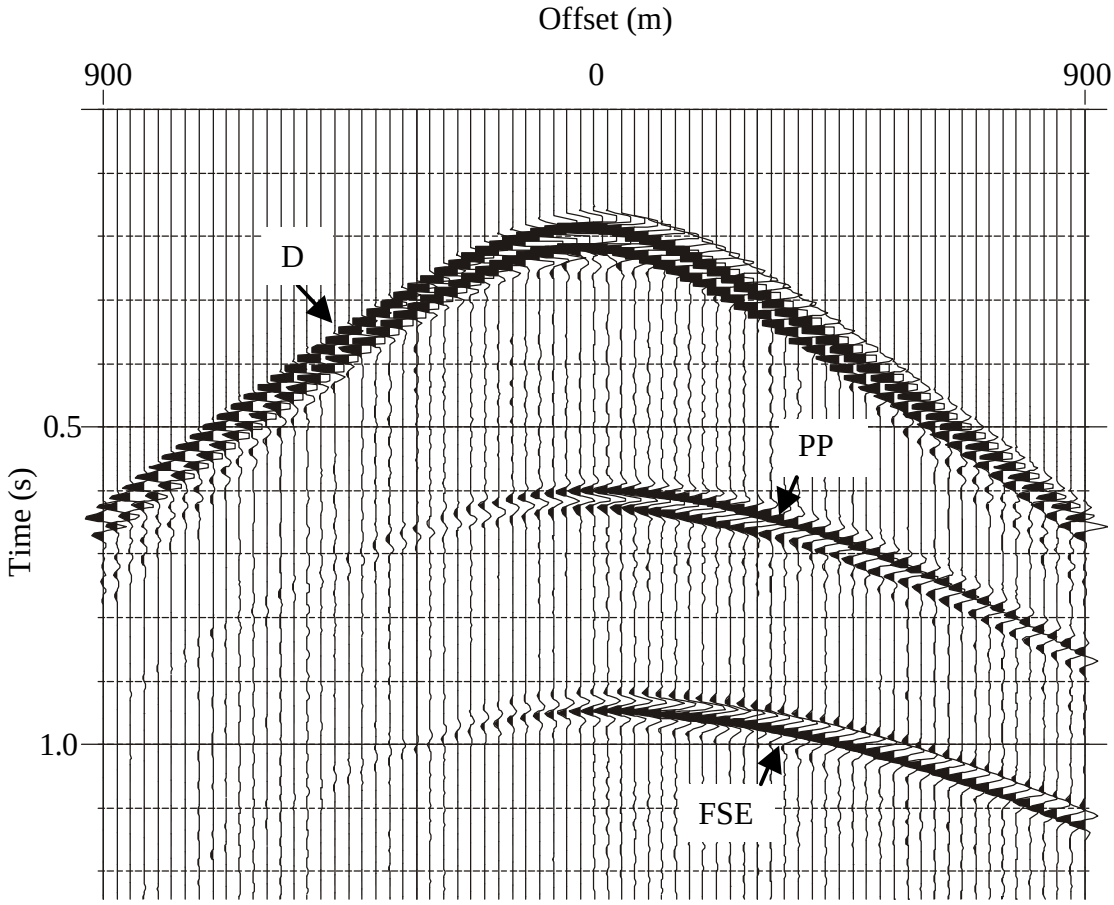

Figure 10. Seismogram corresponding to the pressure field of the liquid over solid 90° corner-edge model. Events labeled D, PP1, and FSE correspond to the direct wave, primary reflection, and free-surface event, respectively. Notice the amplitude reduction on PP1 and FSM1 due to the diffracted energy from the corner-edge.

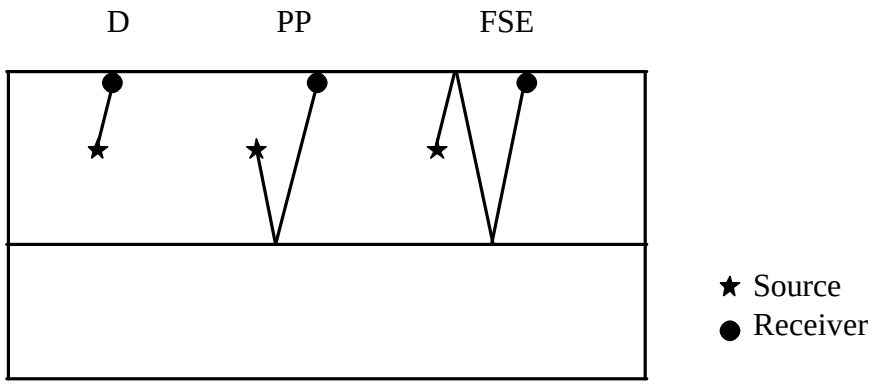

Figure 11. Raypaths associated with the events in Figure 10 and Table 1. D is the direct wave, PP is the primary reflection, and FSE is a free-surface event. Each leg of these events is built from a compressional wave.

Table 1. Zero-offset travel times for events in Figure 10.

Events	Zero-Offset Travel Time (s)
D	0.163
PP	0.576
FSE	0.910

Solid over solid 90° corner-edge model

The solid over solid corner-edge model will again demonstrate the ability of FDM to properly simulate a fully elastic model with step discontinuities and capture converted wave energy. Figure 12 shows the geometry and media properties of the solid over solid corner-edge model. Source and receiver locations are the same as the liquid

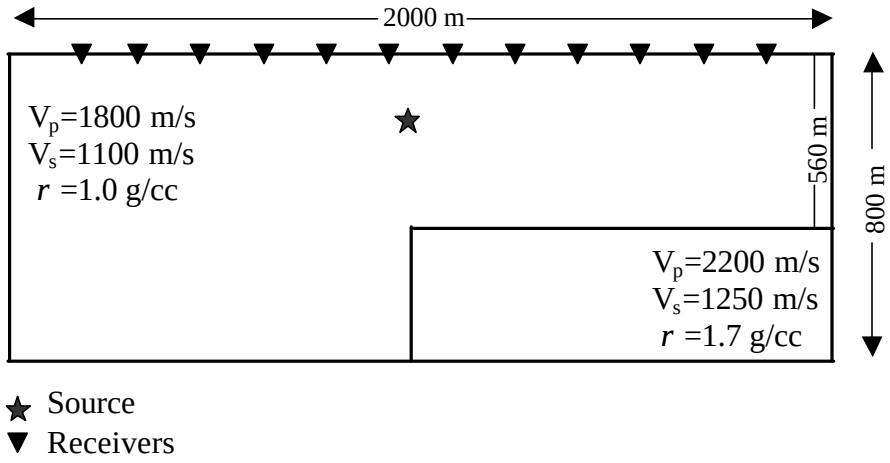

Figure 12. Solid over solid corner-edge model used to generate synthetic seismograms and snapshots. Kosloff absorbing sponge is used at all boundary conditions. The source is located 250 m below the surface.

over solid model. We simulate a two-component (2C) geophone at each receiver location to measure particle velocity in the horizontal and vertical directions. The Kosloff absorbing sponge boundary condition is applied to all edges of the model.

Figures 13 and 14 capture the wavefield associated with the solid over solid 90° corner-edge model. Snapshots A and B show the wavefield radiating outwards and striking the corner-edge. Snapshots C and D show clear P and S-wave reflections, as well as P and S-wave transmissions into the second media. It is very interesting to note the amplitudes associated with the horizontal and vertical particle motions. The wavefield corresponding to the horizontal component of particle motion shows weak reflected P-wave amplitudes compared to the wavefield of the vertical component of particle motion. There are also slight differences in the S-wave amplitudes between the

different components of particle motion. An absorbing boundary condition was applied to the top of the model to help simplify the results. Again, FDM preserves amplitudes of all wave types. These wavefield snapshots give insight on how and where to best sample the reflected energy using both horizontal and vertical components of particle motion and demonstrate the effectiveness of fully elastic FDM.

The seismograms for the solid over solid model displaying horizontal and vertical particle velocity are shown in Figures 15 and 16. Again, the direct arrival is labeled D, the primary reflection is labeled PP, and the P to S converted reflection is labeled PS. The corner-edge produces diffractions which are seen for both the PP and PS events. The raypaths corresponding to these events are shown in Figure 17

Zero-offset travel times are calculated for the solid over solid model and are shown in Table 2. Again, the calculated travel times correspond to the travel times determined by the finite-difference software.

Table 2. Zero-offset travel times for events in Figure 15.

Events	Zero-Offset Travel Time (s)
D	0.136
PP	0.481
PS	0.677

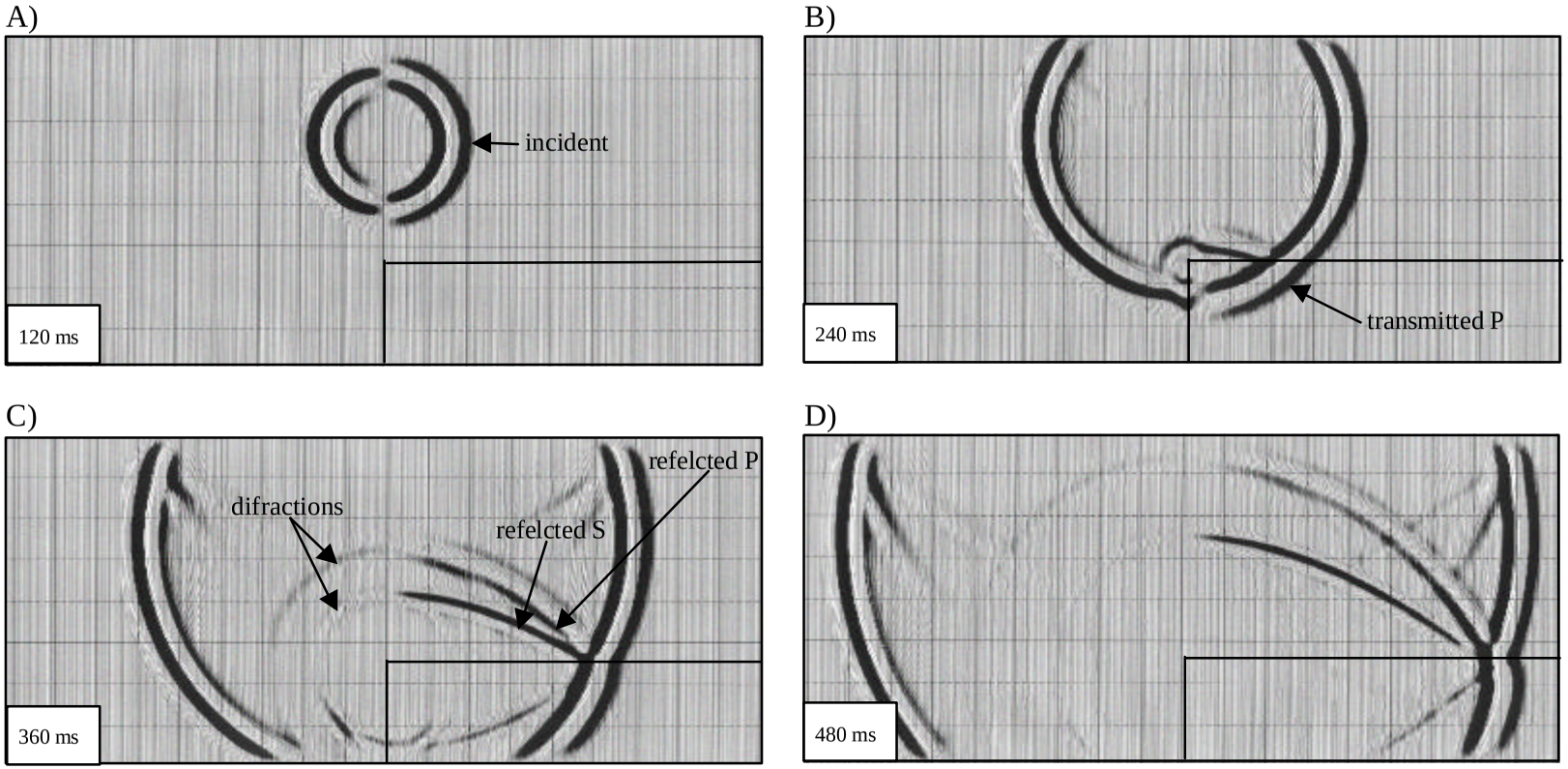

Figure 13. Snapshots showing the horizontal particle velocity wavefield propagating through solid-over-solid 90° corner-edge model as seen in Figure 12. In snapshot A, the wavefield consists of the compressional wave radiating from the explosive source. Snapshot B shows the initial contact with the corner edge. Snapshots C and D show clear compressional and shear wave reflections from the interface and headwaves propagating through the solid media.

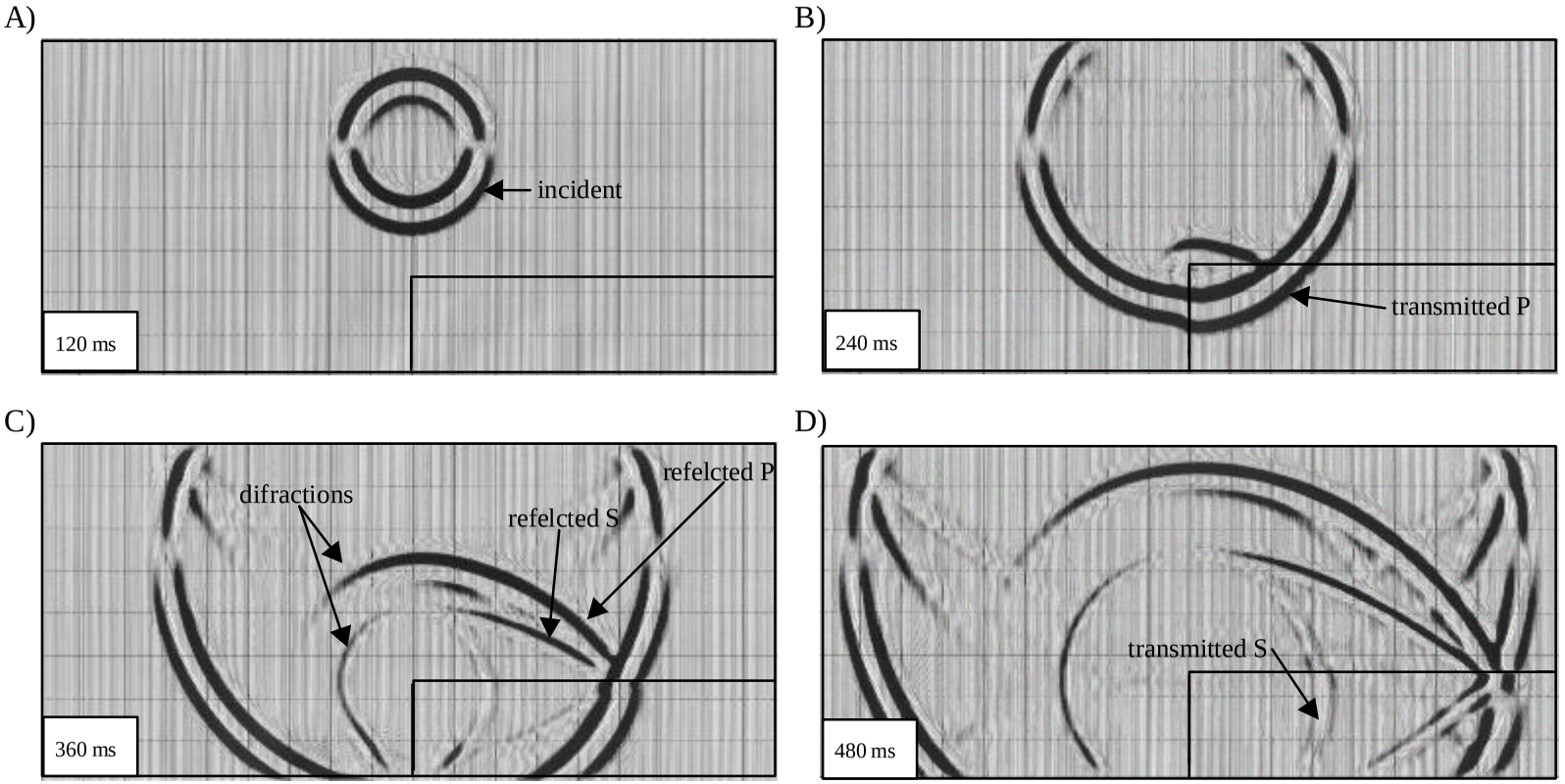

Figure 14. Snapshots showing the vertical particle velocity wavefield propagating through solid-over-solid 90° corner-edge model as seen in Figure 12. In snapshot A., the wavefield consists of the compressional wave radiating from the explosive source. Snapshot B shows the initial contact with the corner edge. Snapshots C and D show clear compressional and shear wave reflections from the interface and headwaves propagating through the solid media.

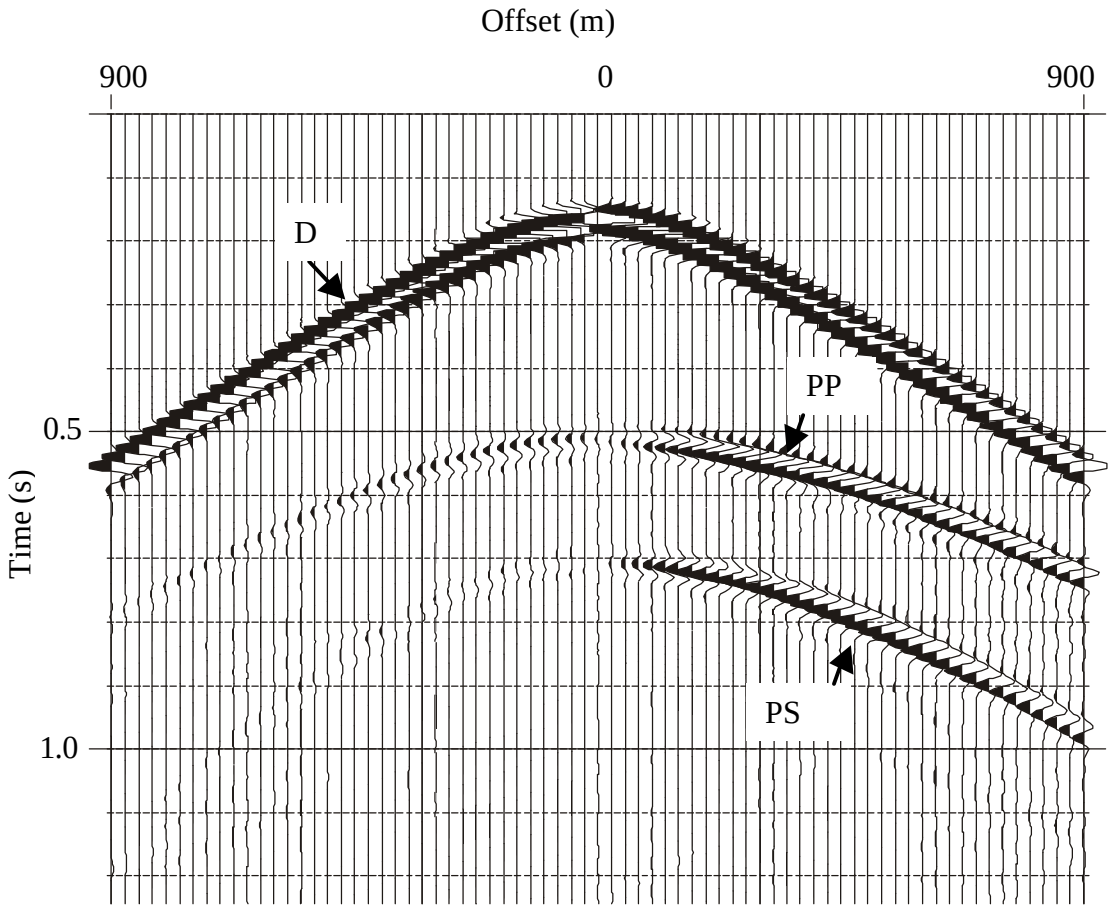

Figure 15. Seismogram corresponding to the horizontal particle velocity of the solid over solid 90° corner-edge model. Events labeled D, PP and PS correspond to the direct wave, primary reflection, and P to S converted wave, respectively. Notice the amplitude reduction on PP and PS due to the diffracted energy from the corner-edge.

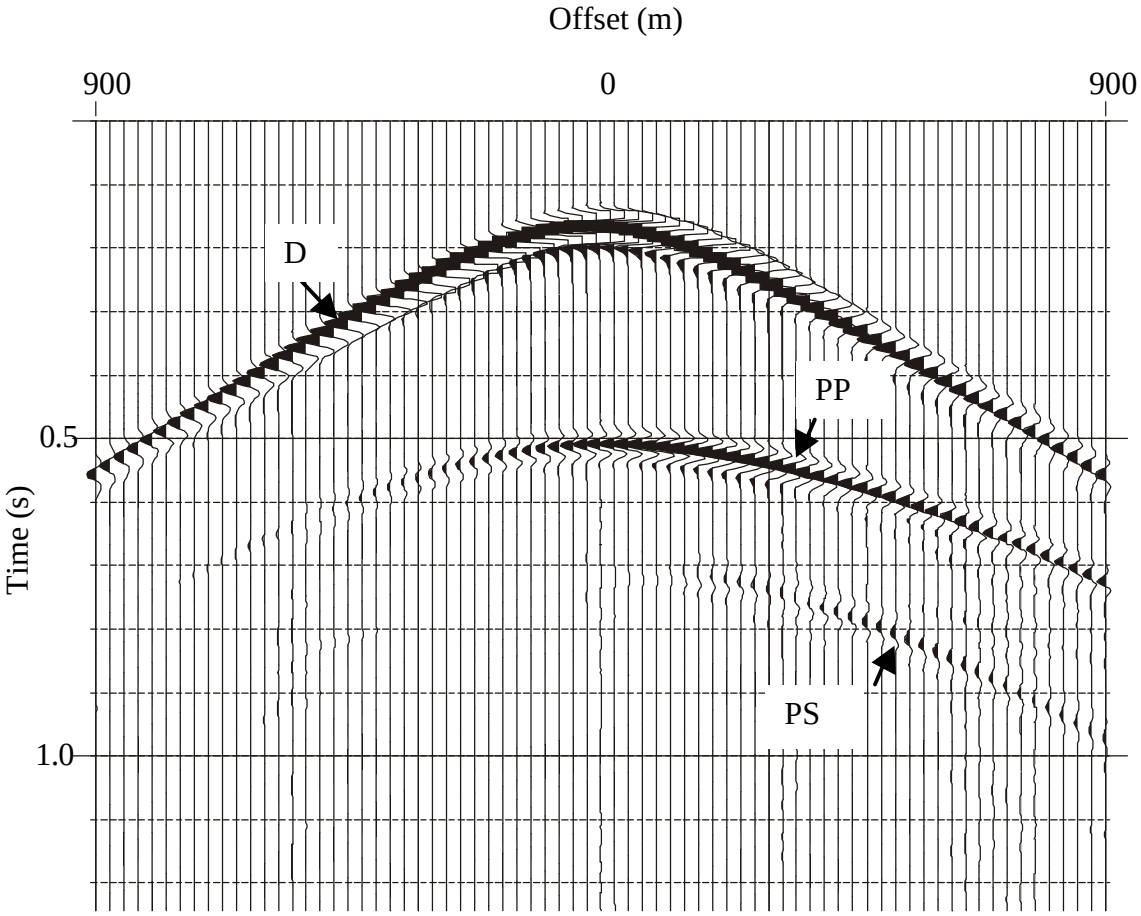

Figure 16. Seismogram corresponding to the vertical particle velocity of the solid over solid 90° corner-edge model. Events labeled D, PP and PS correspond to the direct wave, primary reflection, and P to S converted wave, respectively. Notice the amplitude reduction on PP and PS due to the diffracted energy from the corner-edge.

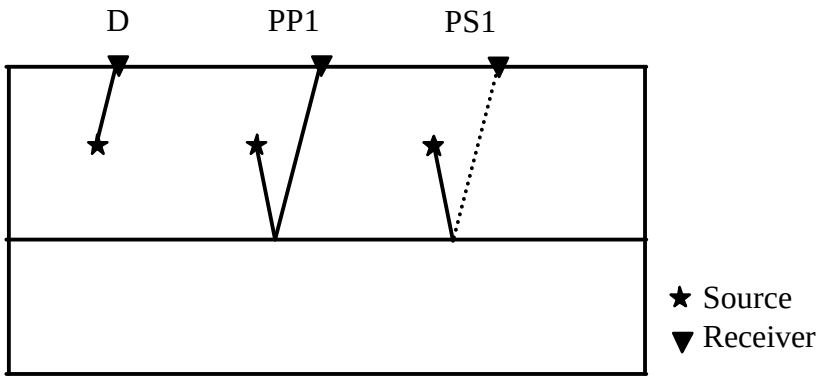

Figure 17. Raypaths associated with the events in Figures 13 and 14 and Table 2. D is the direct wave, PP is the primary reflection, and PS is the converted wave reflection. The solid line corresponds to a compressional component while the dashed line corresponds to a shear component.

Low velocity zones

FDM also allows us to simulate and analyze the effects of low velocity zones. Again, our finite-difference software is sensitive to vertical heterogeneities, thus elastic wave propagation across abrupt velocity or impedance changes can be successfully modeled. These abrupt acoustical impedance variations generate groundroll and/or guided waves. Groundroll is defined as the vertical component of the dispersive energy which travels along or near the surface and is recognized by its low frequency, strong amplitude and slow velocities. Groundroll is common in onshore seismic data and travels as a shear wave. Guided waves refer to dispersive energy trapped in the low velocity zone and guided laterally, traveling as a compressional wave. The water column bounded by a hard seafloor generally produces guided wave energy, although it is not limited to marine data.

Figure 18 shows a simple two-layer model with a large velocity contrast. The upper medium has a P-wave velocity equal to 600 m/s while the lower medium has a P-wave velocity equal to 2000 m/s. Density and shear velocity is held constant to simplify the seismograms. The source position is 10 m below the free surface and 91 receivers are positioned along the surface to record horizontal and vertical particle velocity.

Figures 19 and 20 show the vertical and horizontal components of the particle velocity, respectively. Since the groundroll travels horizontally along the surface as a shear wave, it is recorded on the vertical component of the particle velocity as seen in Figure 19. Notice the low frequency and high amplitude associated with the groundroll. Also, the move-out of the groundroll is large compared to the other seismic events

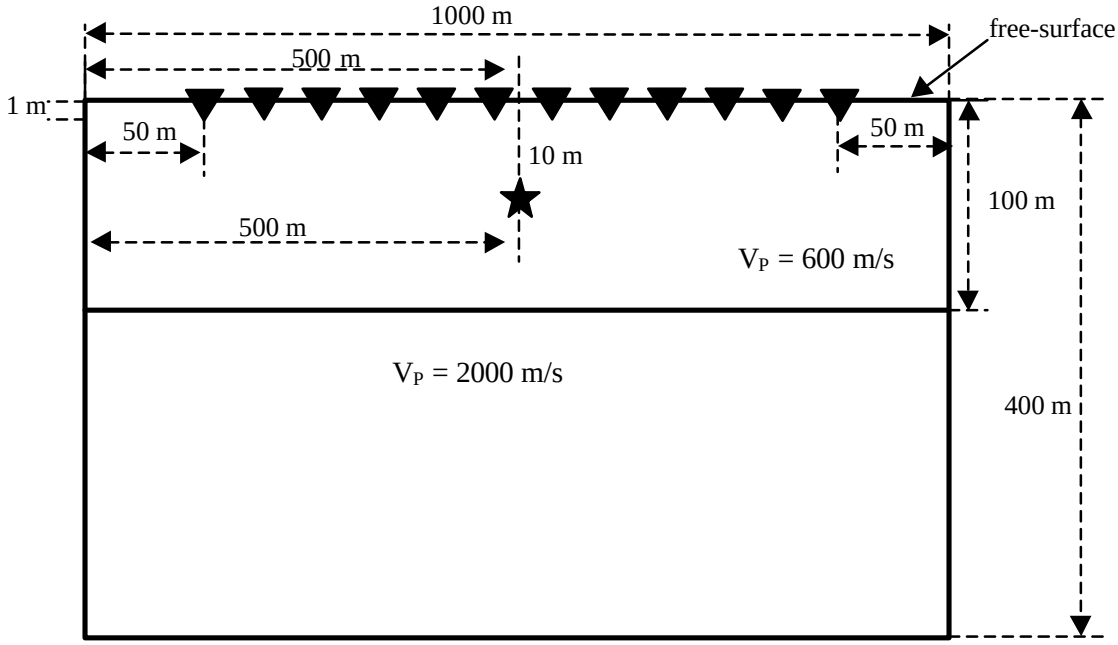

Figure 18. Low velocity layer model used to generate seismic data.

indicating its slow velocity component. Traditional onshore surface seismic surveys routinely measure the vertical particle motion at the surface, thus making groundroll a common problem. The effect of groundroll on the horizontal particle motion is diminished relative to the vertical component, as seen in Figure 20.

A more complicated model is illustrated in Figure 21 with an undulating low velocity region imitating three weathered layer zones with different properties and a faulted subsurface. The corresponding seismograms are seen in Figures 22 and 23 illustrating vertical particle velocity and horizontal particle velocity, respectively. The complexity of the seismograms is due to the large impedance boundaries and the undulating interface simulating an uneven base of weathering. Both groundroll and guided waves can be seen

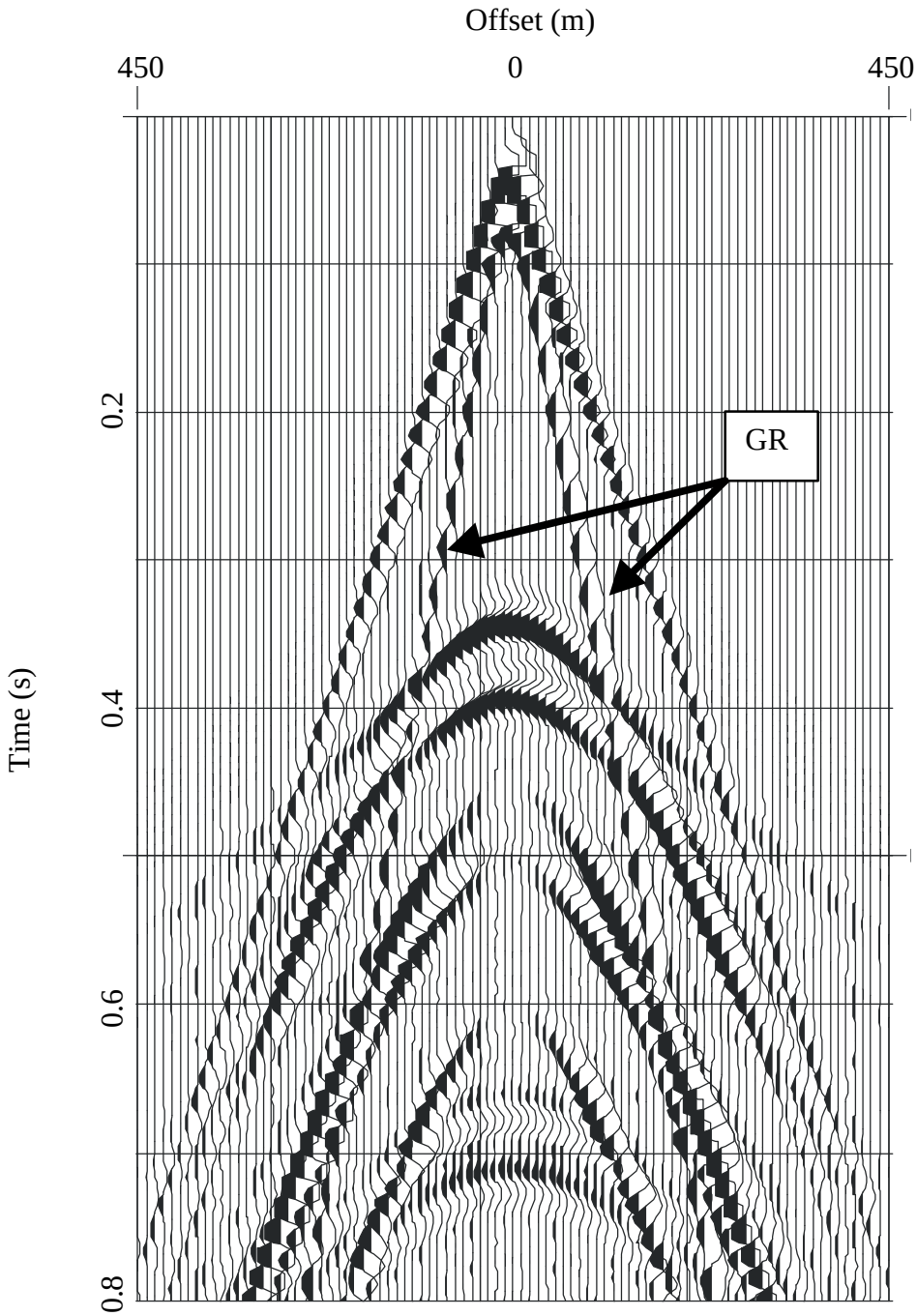

Figure 19. Seismogram displaying ground roll (GR) on the vertical component of particle velocity corresponding to the model in Figure 18.

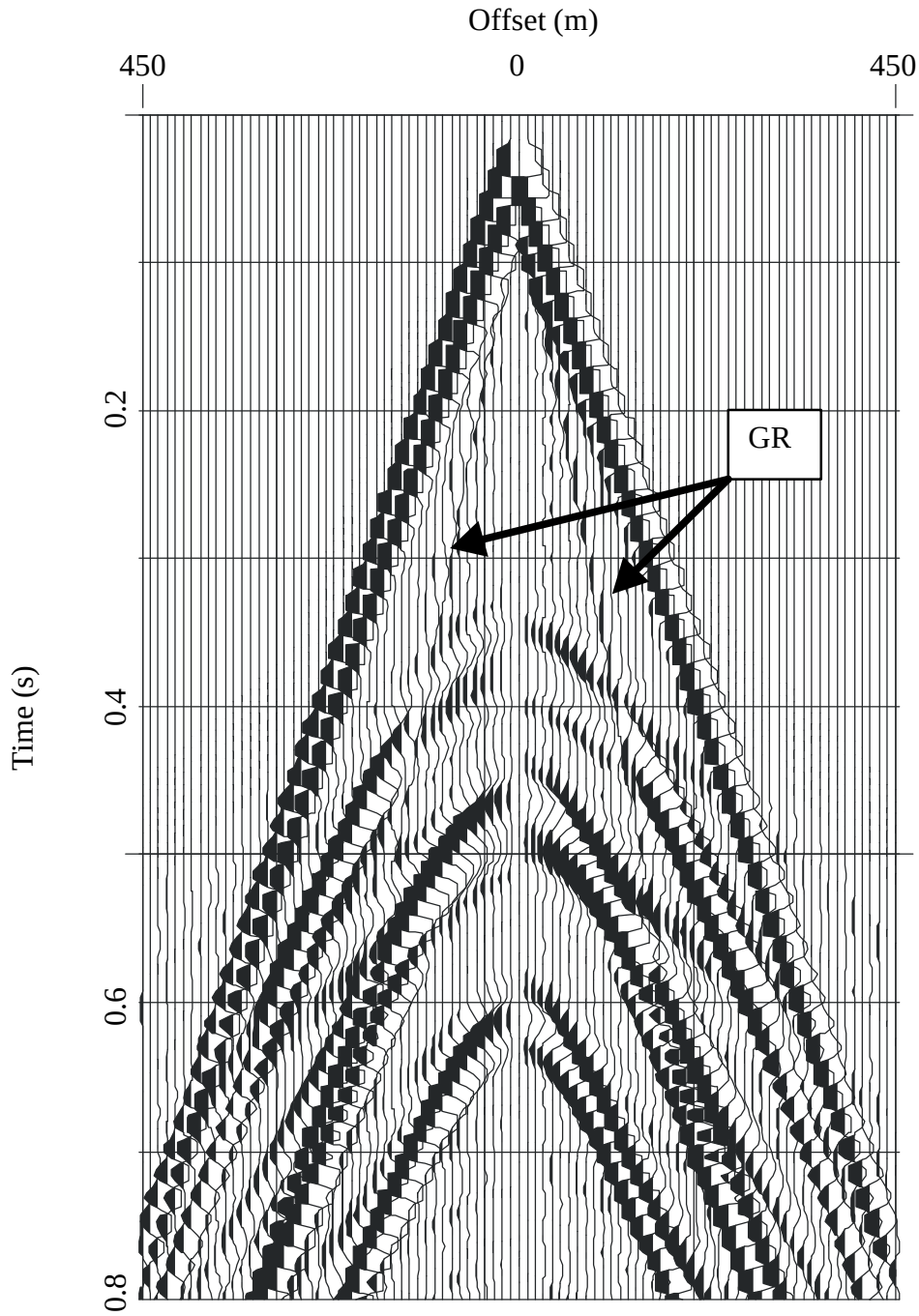

Figure 20. Seismogram displaying ground roll (GR) on the horizontal component of particle velocity corresponding to the model in Figure 18.

in the seismograms. These synthetic results are presented to demonstrate the capability of FDM to generate realistic seismic data which highly resemble real land data.

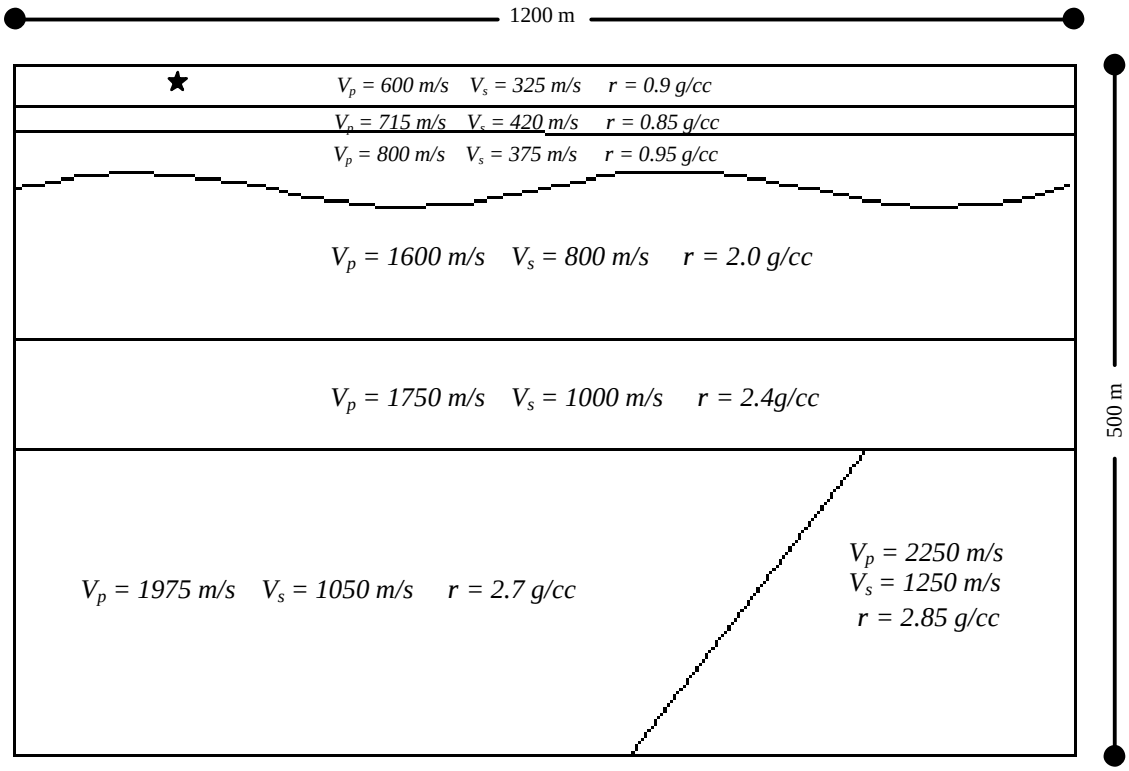

Figure 21. Complex low velocity layer model simulating an undulating base of weathering used to generate seismic data. The source is located 10 m below the surface.

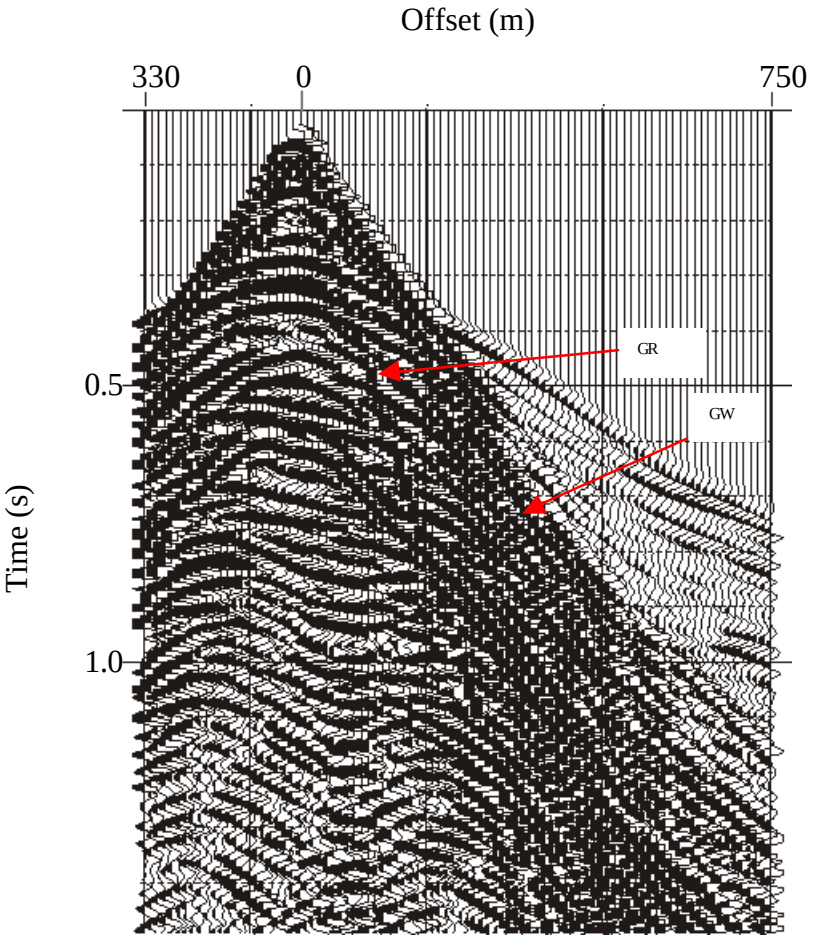

Figure 22. Seismogram displaying groundroll (GR) and guided waves (GW) on the vertical component of particle velocity corresponding to the model in Figure 21.

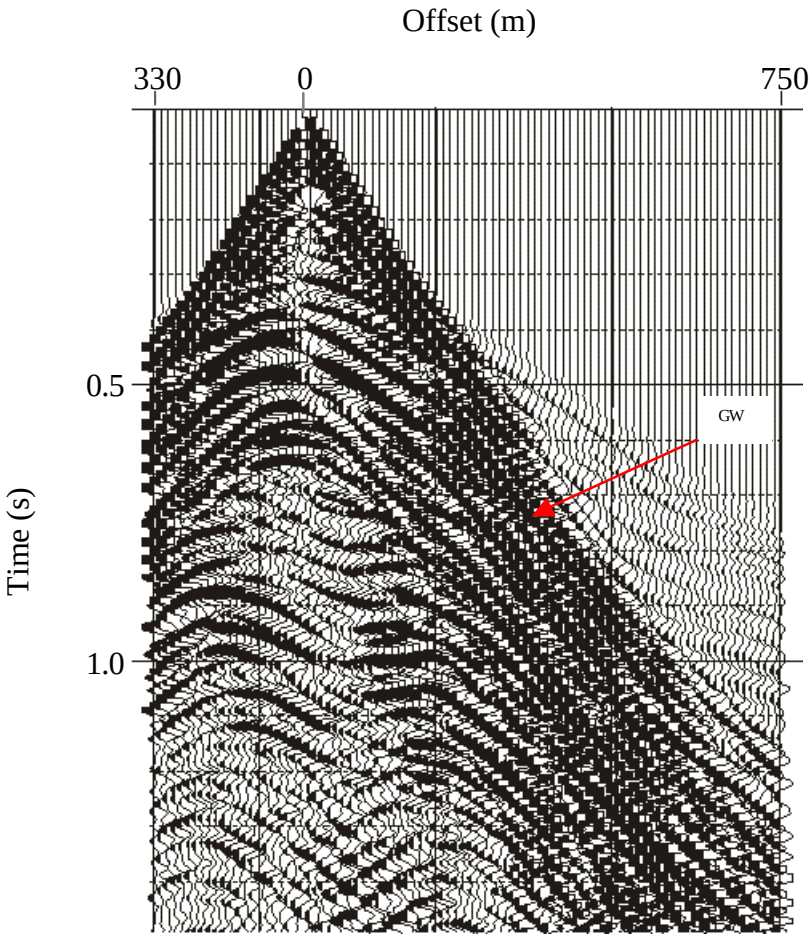

Figure 23. Seismogram displaying guided waves (GW) on the horizontal component of particle velocity corresponding to the model in Figure 21.

LIMITATIONS

Limitations do exist when using FDM. In order to implement the FDM software, the model must be broken into discrete pieces in both space and time. How the model is discritezed affects the performance of the software. The spatial and temporal increments should be small as to avoid numerical dispersion and instability, but large enough to reduce computational time. For fourth-order spatial approximations, Δx and Δz should be at least 1/8 the minimum signal wavelength to avoid numerical dispersion. The stability for the temporal increment is controlled by the following relationship

$$\Delta t < \frac{\Delta x \sqrt{3/8}}{V_{\max}}, \qquad (19)$$

where Δt is the time increment, $\Delta x = \Delta z$ is the space increment, and $V_{\max}$ is the maximum velocity present in the model.

Thus far, finite-difference modeling has been widely used as a 2-D tool. The major factor limiting 3-D application is cost and processing time. Work by Ikelle et. al. (1999a) is being done on multi-shooting, which would drastically reduce computational times, thus making 3-D finite-difference modeling a reality.

CONCLUSIONS

We have demonstrated the ability of finite-difference techniques to solve the elastic wave equations controlled by stress and velocity nodes on a staggered grid for heterogeneous media. The numerical simulations of the 90° corner-edge models and the low velocity region model show accurate results for both travel times and phase

relations. The FDM software requires no special interior boundary conditions for liquid-solid interfaces, making it ideal for modeling marine experiments and investigating the multiple problems. Also, the ability to generate wavefield snapshots aids in understanding wave propagation in complicated media. These simulations demonstrate the effectiveness and quality of finite-difference modeling and justify its use as a tool to generate seismic data to evaluate horizontal and vertical seismic surveys and test demultiple algorithms on complicated seismograms.

CHAPTER III

VERTICAL CABLE SEISMIC RESOLUTION VERSUS SURFACE SEISMIC RESOLUTION

INTRODUCTION

In this chapter, we analyze the imaging resolution between vertical cable surveys and horizontal surveys such as towed-streamer, ocean bottom cables (OBC) or land surface seismic. We will discuss three cases, a scattering point, a horizontal reflector and a dipping reflector in 2-D space. We follow with some generalization on 3-D geometries.

RESOLUTION OF VERTICAL CABLE DATA VERSUS SURFACE DATA

Imaging resolution of a point scatterer

To fully analyze the applicability of vertical cable surveys, we must discuss the fundamental problem of spacing between cables and sampling within the cable. We pose the problem of vertical cable sampling as that of finding the spacing between cables which allows us to image at least as well as surface seismic. In this subsection, we will analyze the resolution of a point scatterer at a fixed depth as seen in Figure 24.

We begin our discussion on resolution by analyzing a single image point or scattering point. Figure 25 illustrates an example of how we define angular coverage for both the surface and vertical cable survey. $q_{\max}^{S}$ is the maximum angle of reflection for

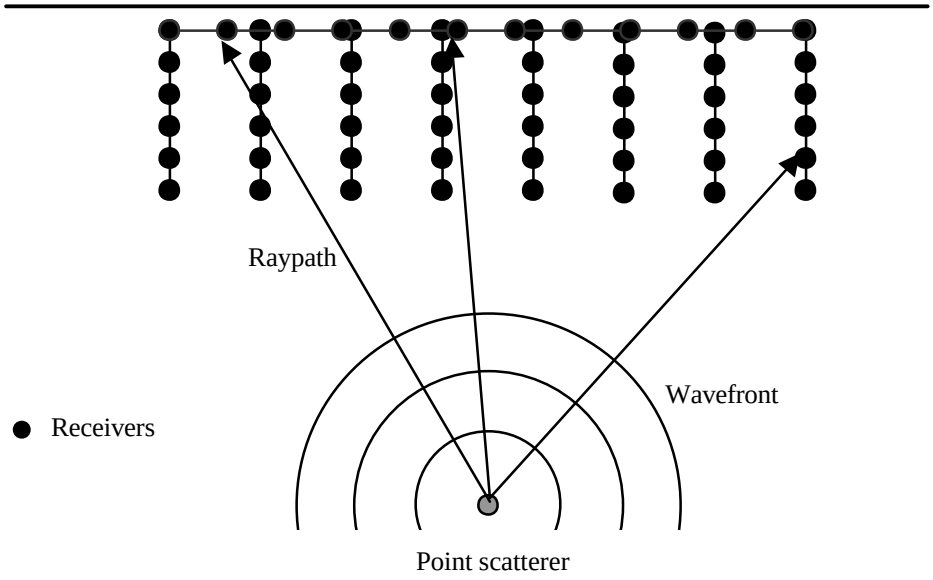

Figure 24. Model used to analyze the relative resolution of a point scatterer for a vertical cable survey and a horizontal survey. A point scatterer acts as a source position and sends out its own wavefront.

the surface array. $q^{V}_{\max}$ is the maximum angle of reflection for the vertical cables. To achieve equal or superior resolution using vertical cables, $\Delta q = q^{V}_{\max} - q^{S}_{\max}$ must be greater than zero. In addition, the ray coverage between (0, $q^{V}_{\max}$) must be sampled as densely or greater as the equivalent surface seismic in this interval. For a given image point of depth Z and cable length h, we can calculate the increased angular coverage vertical cable survey can achieve by

$$\tan(\Delta q) = \frac{hX}{Z^2 + X^2 - Zh} \ . \qquad (20)$$

So for a given $q^{S}_{\max}$ and the corresponding density coverage from the surface data, the problem becomes one of how to properly sample the wavefield using vertical cables to achieve superior coverage for a given Δq . Figure 26 compares the resolution between the surface data and vertical cable data for an image point at a depth of 2000 m. The surface survey consists of 101 shots and 101 receivers, each spaced at a 25 m interval. Receivers are static in this survey. For this surface survey, $q^{S}_{\max}$ is approximately 64° and the angular coverage is represented by the black line in Figure 26. This line was obtained by grouping all angles in the interval (0, $q^{S}_{\max}$) as a function of their occurrences. The angle was sampled every one degree.

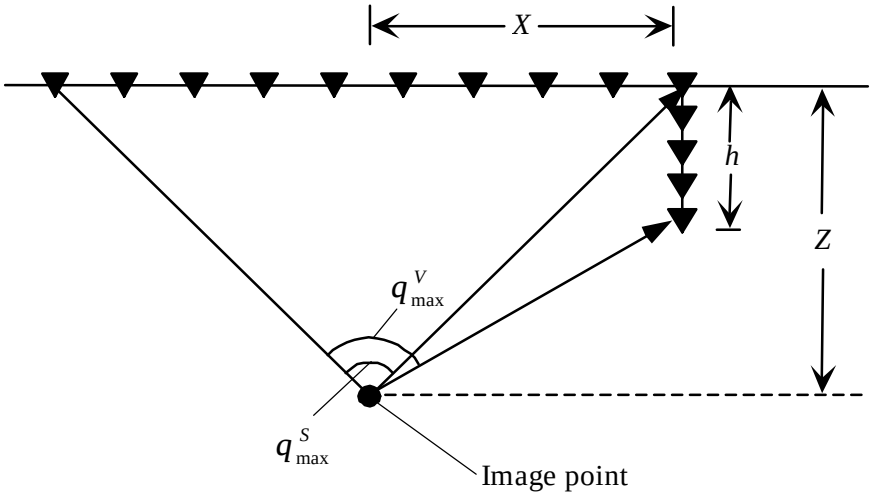

Figure 25. Schematic representation of raypaths reflected from an image point at a depth *Z*. $q^{S}_{\max}$ is the maximum angle of reflection for the surface array and $q^{V}_{\max}$ is the maximum angle of reflection for the vertical cable.

Now, we want to compare the imaging resolution of vertical cables over the same survey area. Each of the following vertical cable surveys assume a maximum borehole depth of 500 m, which at maximum would yield a $\Delta q = 7.8^{\circ}$. To achieve equivalent vertical cable coverage, 6 cables spaced every 500 m with 17 receivers spaced every 25 m were used as seen in Figure 26. If this sampling is retained within each cable but cable spacing is increased to 833 m, inadequate sampling density with respect to cable spacing results in the green line in Figure. Superior vertical cable coverage is obtained by using 8 cables spaced every 357 m, blue line in Figure 26.

We can also determine the sampling criteria assuming we keep a constant distance between cables (500 m) and only vary the sampling within the cable for a cable length of 500 m. Figure 27 shows the results of varying only the sampling within the cable. The black line represents the surface data using the parameters previously mentioned. The red line corresponds to equivalent vertical cable data using 17 receivers with a 31 m interval. Superior vertical cable coverage is obtained with 26 receivers at 20 m intervals. Using 10 receivers at 55 m intervals results in very poor coverage compared to the original surface data. The stair-step appearance of the vertical cable curves is attributed to the gap between cables. Assuming the maximum depth of the vertical cables is 500 m, then vertical cable imaging resolution is increased by decreasing the cable intervals and/or increasing the sampling density along the cables. Increasing the receiver density does not result in extreme additional costs as in land surveys or OBC surveys, only additional data storage capabilities. Therefore, it is reasonable to densely sampling along the vertical cables. The results here show we can

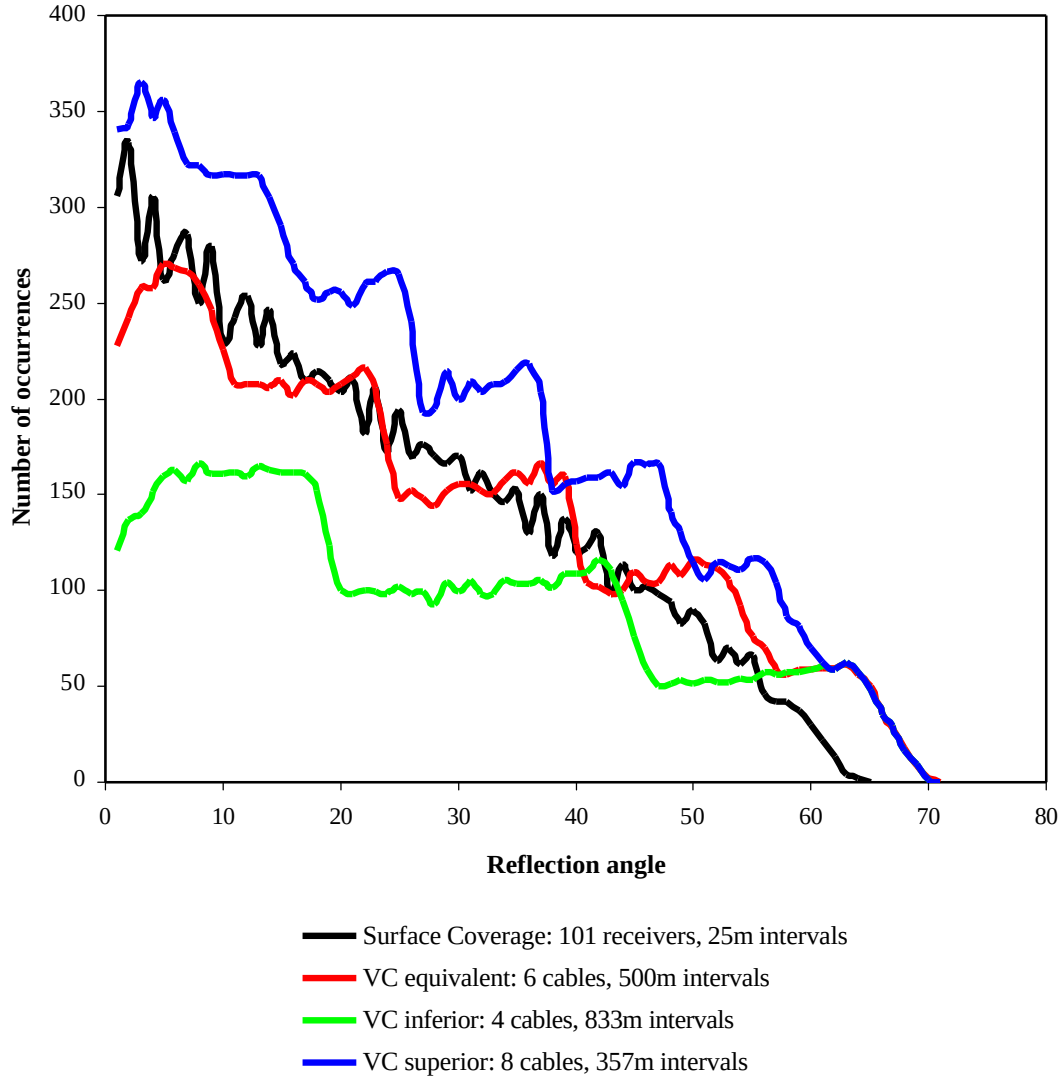

Figure 26. Angular coverage for an image point at a depth of 2000 m and simulating 101 shots spaced every 25 m for surface array and vertical arrays. For this experiment, only vertical cable spacing was varied. The receiver spacing along the vertical cables was constant, 17 receivers spaced every 25 m, and the vertical cable length was no longer than 500 m for any simulation.

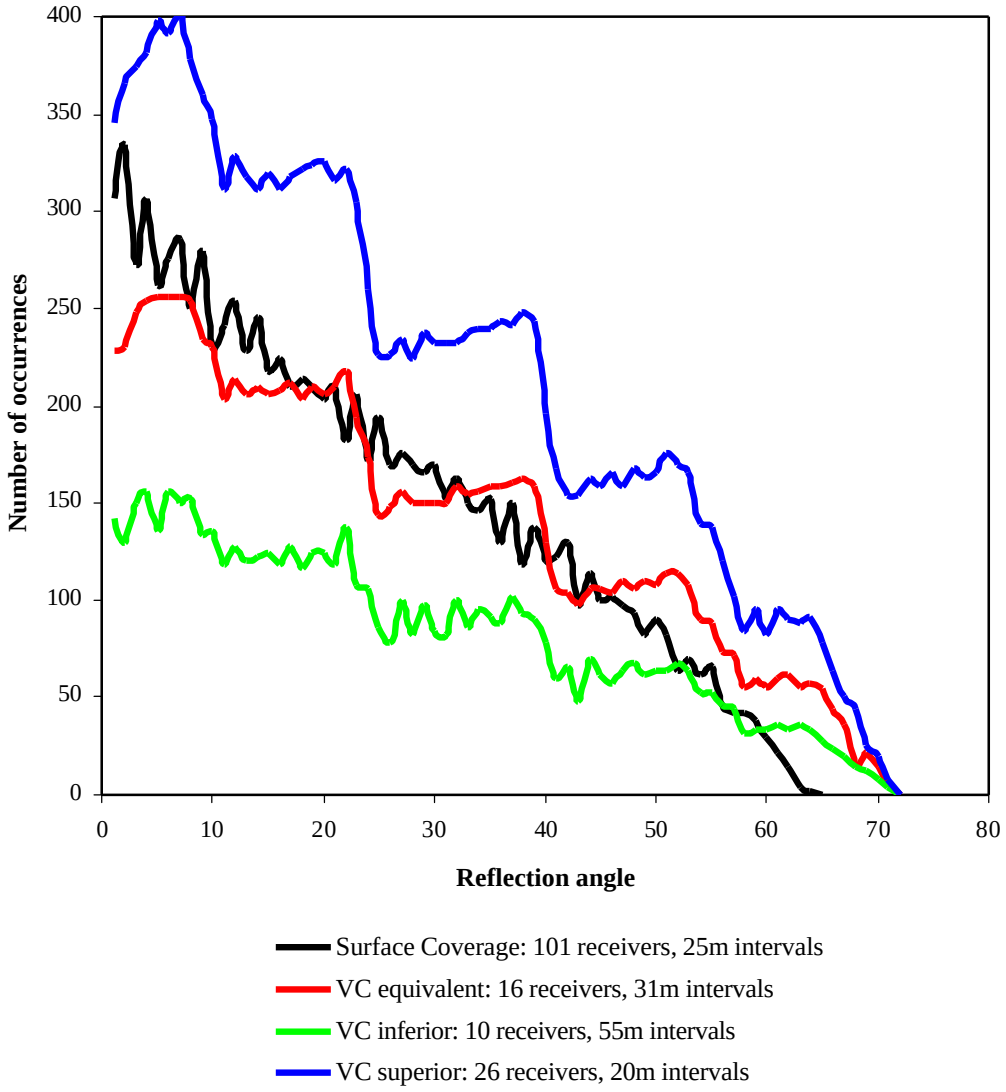

Figure 27. Angular coverage for an image point at a depth of 2000 m and simulating 101 shots spaced every 25 m for surface array and vertical arrays. For this experiment, the maximum vertical cable depth was 500 m and the cable spacing was constant, 6 cables at 500m intervals, while the sampling within cables varied.

achieve superior imaging resolution of a point scatterer over surface seismic using 500 m cables with a cable interval of 500 m and sampling adequately along each cable.

Resolution of a reflector

We would now like to analyze the relative imaging resolution of vertical cables and surface receivers for a horizontal and dipping reflector. A reflector is simply a series of closely spaced image points. Therefore, we can extend the same methodology we used for the single point scatterer to several points along a reflector. For a horizontal reflector, the image points vary only laterally. To study the resolution along this reflector, we need only to analyze several representative points which capture the lateral variation of resolution. The same is true for a dipping reflector. The resolution analysis can be done for several representative depth points along the surface to understand the difference in imaging resolution between a vertical cable survey and a horizontal survey.

Horizontal reflector

Let us start with the horizontal reflector resolution analysis. We consider the model as shown in Figure 28. 101 horizontal receivers at 25 m intervals are distributed at the surface. A source is initiated coincident with each surface receiver location. The refection surface is at a depth of 2000 m. We analyze three refection points at the following x,z coordinates: (0, 2000), (625, 2000) and (1250, 2000). For this case, the symmetry of the reflection surface allows us to limit the resolution to one side of the reflector. The dashed line in Figure 30A, B and C shows the occurrences of the various

reflection angles for the surface receivers. For the case when the image point is located at the center of the survey, (1250, 2000), the maximum imaging resolution occurs. As the point moves away from the center, the reflection angle decreases and the occurrences of the small angles increases.

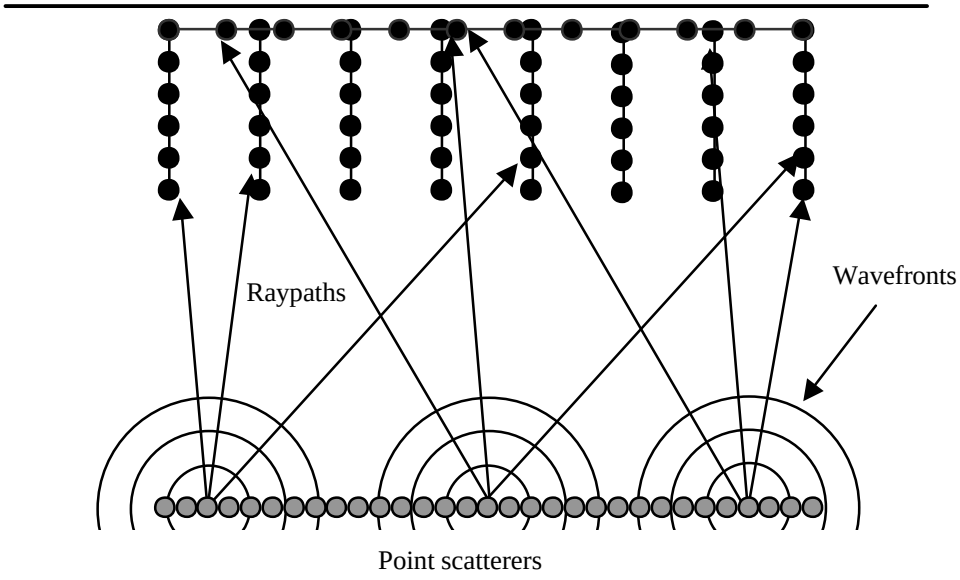

Figure 28. A series of closely spaced point scatterers or image points act as a reflection surface. Analyzing several representative points along the reflector can determine the relative imaging resolution for a vertical survey vs. a horizontal survey.

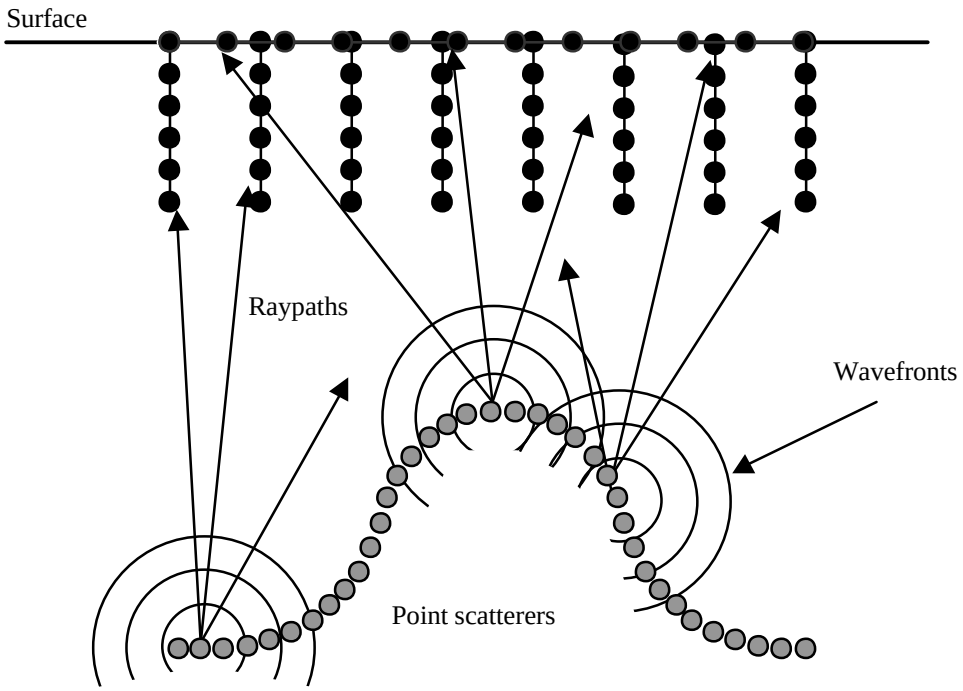

Figure 29. A series of closely spaced point scatterers or image points act as a dipping reflection surface. Analyzing several representative points along the reflector from various depths can determine the relative imaging resolution for a vertical survey vs. a horizontal survey.

Now we consider a vertical cable survey consisting of 5 cables equally distributed over the 2500 m survey area. We distribute 26 receivers along the cable at 20 m intervals, resulting in a cable length of 500 m. This geometry gives us equivalent resolution of the reflector compared to the surface survey as illustrated by the solid line in Figure 30A, B and C. The previous statements concerning surface resolution apply to the vertical cables, i.e. maximum resolution of the reflector occurs at the center of the survey. Furthermore, this analysis demonstrates that the relative resolution between the

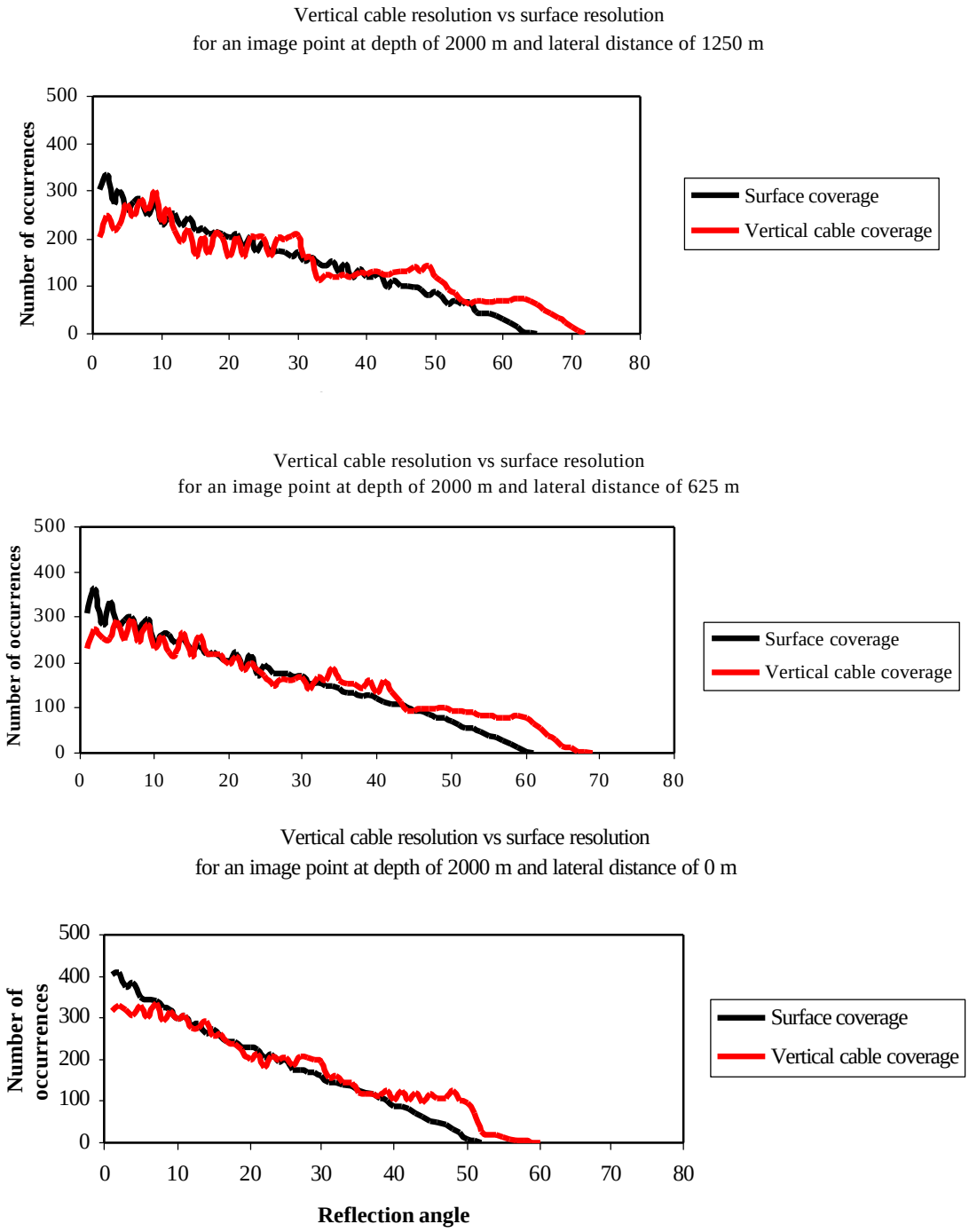

Figure 30. Imaging resolution analysis for vertical cables and surface survey for a horizontal reflector at a depth of 2000 m. The reflector can be treated as a series of image point, where then an image point analysis can be done on several representative points along the reflector. Here, we demonstrate that the relative resolution between vertical cables and surface receivers for points along a horizontal reflector remains constant.

vertical cables and surface receivers for this specific sampling density remains equivalent, regardless of reflector position. Therefore, if we increase sampling density along the vertical cables, the improvement of resolution of each image point relative to the surface survey should remain superior. Figure 31A, B and C demonstrate this concept. Here, we increase the sampling density along the vertical cables to 12.5 m, keeping the cable spacing and length the same. The dashed line represents the surface receivers as described previously. The solid line in Figure 31A, B and C illustrate the superior resolution of vertical cables compared to the surface survey; the occurrences of reflection angles for the vertical cables more than doubles that of the surface data for much of the total angular coverage. The relative imaging resolution between the vertical and horizontal surveys for each point along the reflector is preserved as in the previous case where the coverage was equivalent.

Dipping reflector

Here, we consider the image resolution of a dipping reflector as seen in Figure 29. The surface surveys remains the same, 101 horizontal receivers at 25 m intervals, and a source is again initiated coincident with each surface receiver location. To generate equivalent vertical cable data, we use the same scenario as in the horizontal reflector. The refection surface varies from a depth of 2000 m to 1000 m at its apex, simulating a salt dome. We analyze three refection points at the following x,z coordinates: (0, 2000), (625, 1500) and (1250, 1000). For this case, the symmetry of the reflection surface allows us to limit the resolution to one side of the reflector. The

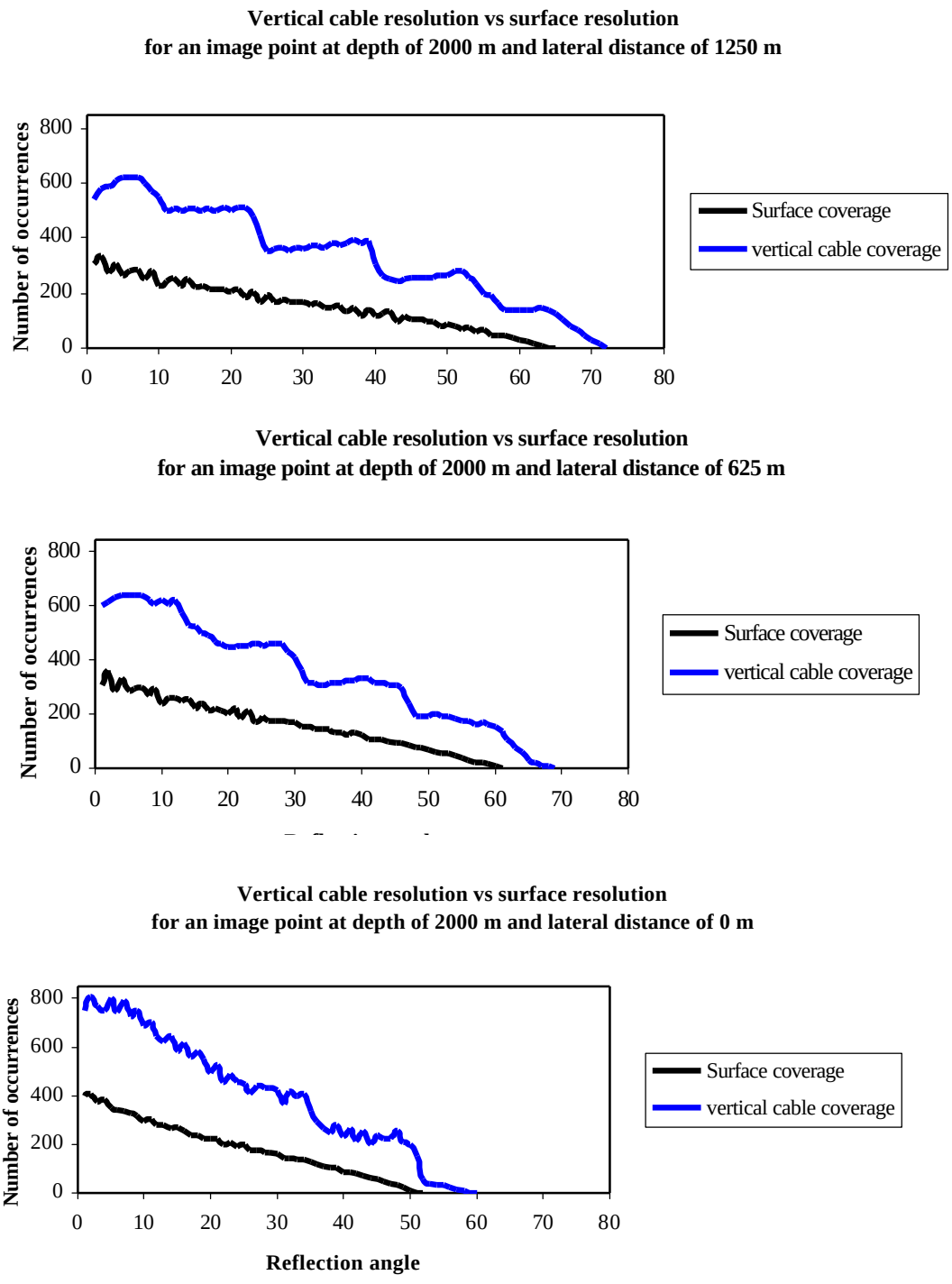

Figure 31. Imaging resolution analysis for vertical cables and surface survey for a horizontal reflector at a depth of 2000 m. Here, we demonstrate superior vertical cable resolution by using a receiver interval of 12.5 m. The relative resolution between vertical cables and surface receivers for points along a horizontal reflector remains constant.

dashed line in Figure 32A, B and C shows the occurrences of the various reflection angles for the surface receivers. The results demonstrate that as the depth of the reflection point increases, angular coverage decreases and the number of occurrences of the smaller angles increases, just as one would expect and is seen by comparing Figure 30A and B with Figure 32A and B. The relative imaging resolution of the dipping reflector stays equivalent between the vertical cables and surface survey.

Now, we increase the sampling density along the vertical cables to 12.5 m and simulate the same resolution analysis producing the data in Figure 33A, B and C. The dashed line represents the surface data and the solid line represents the vertical cable data. Again, the vertical cable data records larger angular coverage with more sampling of all angles for the dipping reflector. By comparing the results in Figure 33A and B with Figure 31A and B, we see that as the image point gets deeper, Δq becomes smaller, just as one would expect, and the relative resolution between the vertical cables and surface data becomes increasingly larger. By comparing the results in Figure 33A and B with Figure 31A and B, we see that the relative change in imaging resolution between superior vertical cable data and surface data is no longer constant for a varying image point in the vertical direction, rather it increases as depth increases, just as one would expect.

In summary, we have proposed a methodology for calculating the imaging resolution by determining the angular coverage and occurrences of each angle within that coverage for a vertical cable survey and a surface survey. We demonstrate that the imaging resolution for an image point can be superior for a vertical cable survey

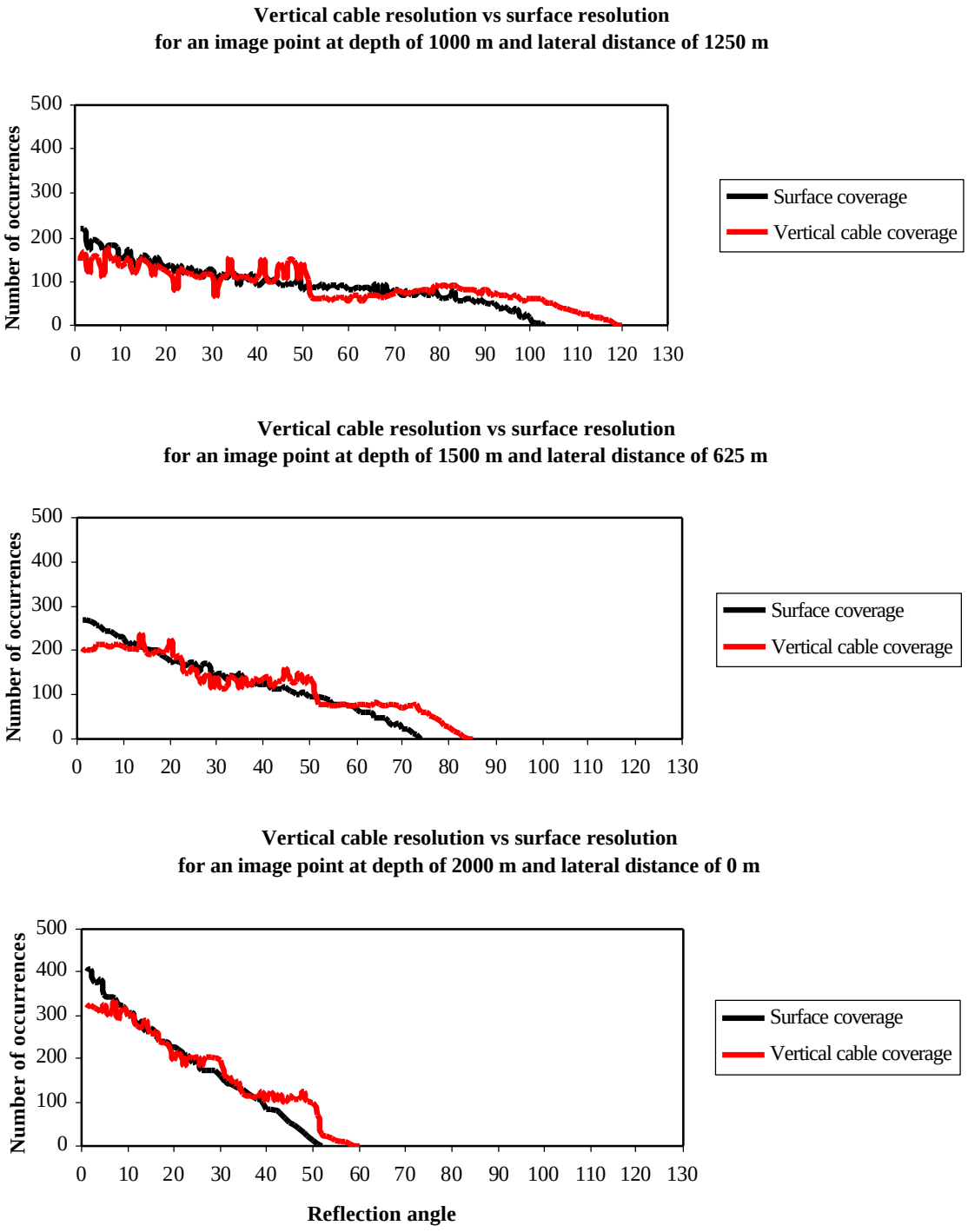

Figure 32. Imaging resolution analysis for vertical cables and surface survey for a dipping reflector showing equivalent vertical cable and surface resolution.

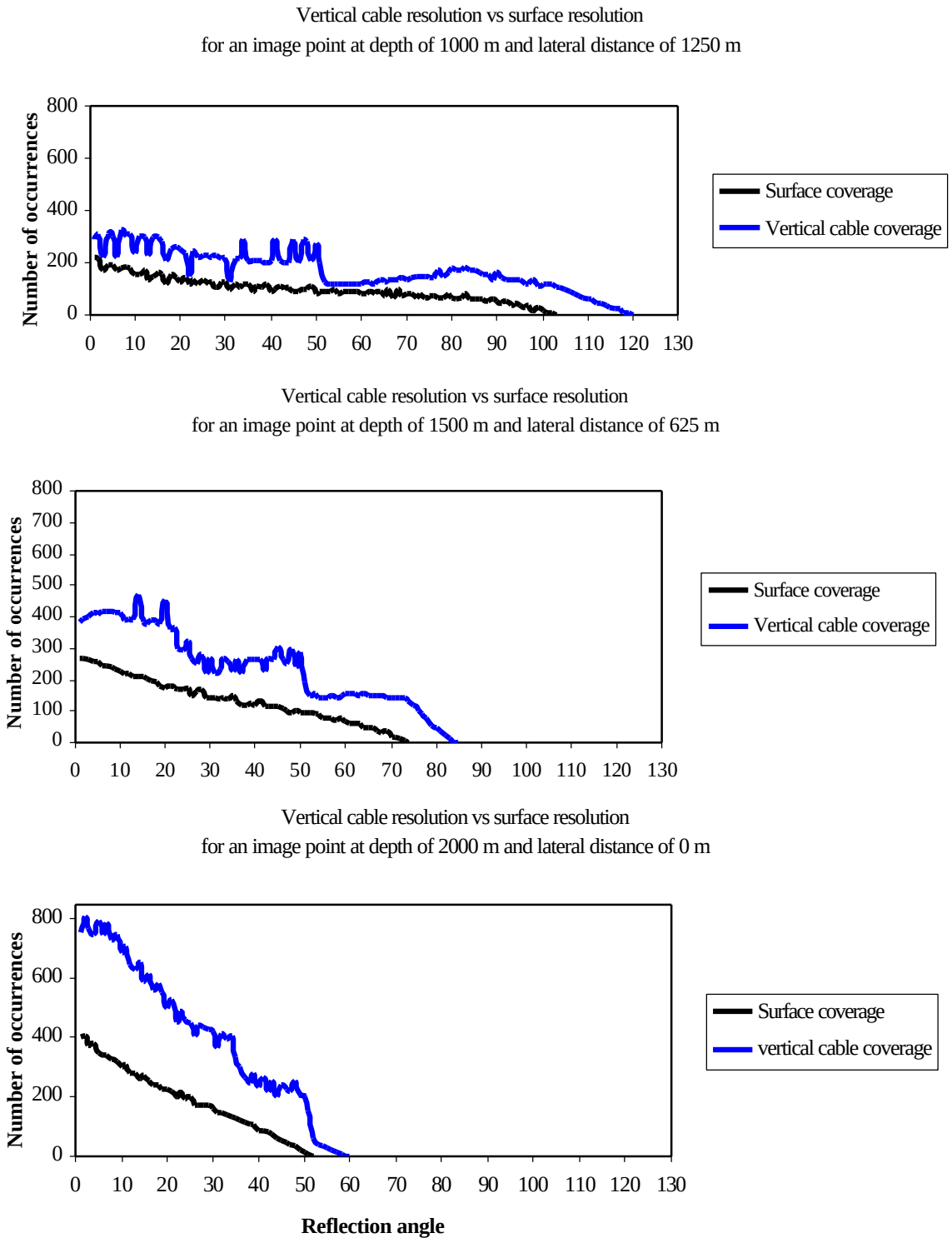

Figure 33. Imaging resolution analysis for vertical cables and surface survey for a dipping reflector using 5 vertical cables with a 12.5 m receiver interval along the 500 m long cables. The vertical cables capture larger reflection angles and more occurrences of all angles compared to the surface data.

compared to that of a surface survey. By treating a reflector as a series of closely spaced image points, we can use the same methodology to demonstrate the superior resolution of vertical cable surveys relative to surface surveys for both a horizontal reflector and a dipping reflector.

ECONOMIC IMPACT OF MARINE VERTICAL CABLES

As mentioned earlier, vertical cable also has practical and economic benefits over towed-streamer methods. In areas congested by drilling platforms and production facilities, towed-streamers are denied access or are very clumsy and cumbersome and require time to navigate through these areas. Vertical cable operations can overcome this problem because the shooting vessel does not carry streamers making it highly maneuverable compared to a seismic vessel towing streamers; thus, reducing acquisition time and costs. For instance, consider the acquisition line as seen in Figure 34 where an obstruction will not allow the surface cables to be present. What is the effect on the relative imaging resolution between vertical cable data and surface data? Using the same parameters above for the equivalent imaging for a horizontal reflector, we demonstrate the effects of removing 21 of the surface receivers from the middle of the receiver line where the surface obstruction occurs. As expected, imaging resolution for the surface data is reduced compared to the case without the obstacle as seen in Figure 35. Notice the imaging resolution of the vertical cables remains unchanged and superior compared to the surface data.

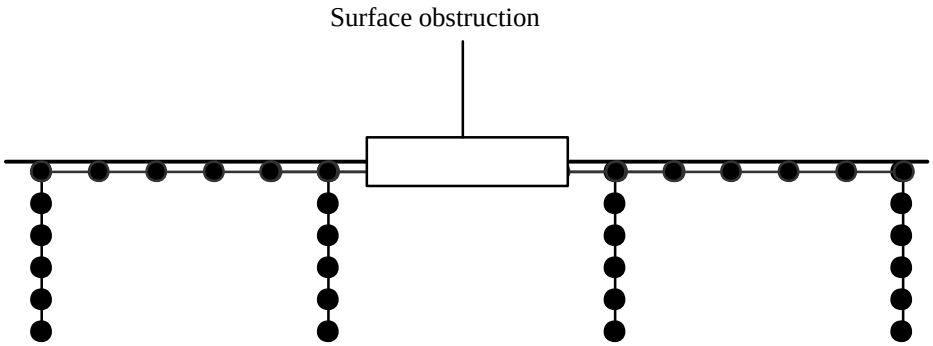

Figure 34. Surface obstruction restricting access of surface receivers.

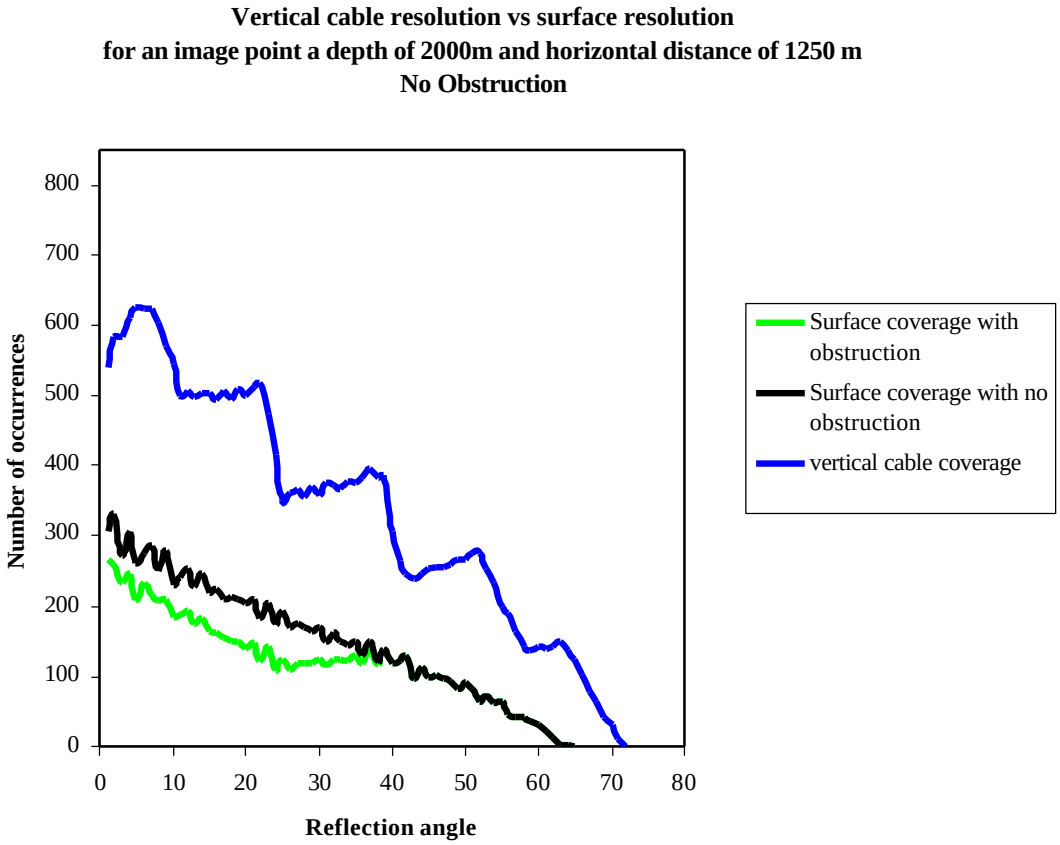

Figure 35. Imaging resolution analysis for a scenario with a surface obstruction. The number of occurrences for the low to mid reflection angles are reduced for the surface data. Notice that the vertical cable data is unchanged and superior compared to the surface data.

GENERALIZATIONS OF RESOLUTION ANALYSIS FOR 3-D GEOMETRIES

As we have demonstrated in previous sections, vertical cable surveying resolution compares very favorably to surface methods. Here, we generalize our approach and results to 3-D source and receiver configurations. We will conduct the relative resolution analysis for towed-streamer, OBC, land surface seismic and vertical cable data. As we will see, each surveying method presents different benefits and challenges, and each method will be compared to the vertical cable resolution.

We approach the resolution analysis in the same manner as the previous 2-D analysis, although now, we must add an additional angle to account for the source and receiver 3-D geometries as seen in Figure 36. The dip angle, q, for each source and receiver position is defined as

$$q = \frac{1}{2}\left(q_s + q_r\right), \tag{21}$$

where q_s is the incident angle associated with the source and scattering point and q_r is the angle defined by the raypath from the normal to the scattering point and the receiver. The azimuthal angle, f, is defined as

$$f = f_s + f_r, \tag{22}$$

where f_s is calculated by projecting the scattering point to the surface and measuring the angle created by a line connecting the scattering point and source location and f_r is calculated by measuring the angle created by a line connecting the scattering point and receiver location. We measure the occurrences of these angles at every degree for all source-receiver positions and plot them by azimuth versus angular coverage, such that

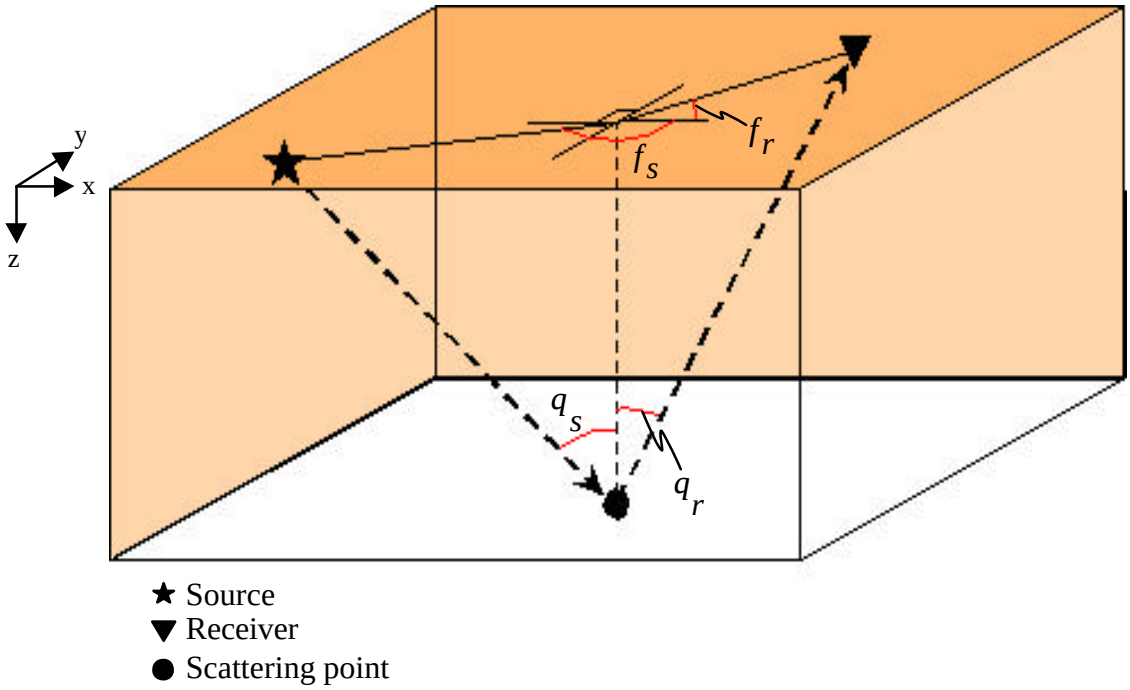

Figure 36. Illustration of angular coverage and azimuth associated with source, receiver and scattering point not in the same acquisition plane.

the higher density of coverage relates to better resolution.

Towed-streamer vs. marine vertical cable

The implementation of vertical cable surveying in the marine environment has several benefits. For one, the cables are suspended within the water column, hence, no drilling is required and cable spacing is not an issue as in the land scenario. As we stated previously, the seismic vessel is only towing the source array, consequently, we must determine source line intervals which provide adequate resolution. Therefore, we begin our 3-D resolution analysis by evaluating different vertical cable acquisition parameters to establish adequate resolution compared to the towed-streamer method.

We define our survey area as seen in Figure 37 considering only the scattering point located at the center of the survey area. We use 36 vertical cables at a 500 m spacing in the x and y directions with 41 receivers at 12.5 m intervals along each cable in the z direction. We simulate a vertical cable survey consisting of 6 source lines in the horizontal direction, each having 101 shotpoints at 25 m intervals. The resulting relative coverage is seen in Figure 38A. The data is displayed as azimuthal versus dip angle, with blue colors corresponding to low occurrences and poor coverage and red corresponding to very high occurrences and better coverage. All the plots use this same scale, so the relative intensity can be compared for all scenarios. In Figure 38A, we see the small dip angles (less than 10°) are poorly resolved. This is due to the large cable and source-line spacing; there are no small angle occurrences measured from the scattering point. Figure 38B shows the results of using 11 source lines at 250 m intervals. We see that the density of coverage is improving for all angles. By decreasing the source line spacing to 100 m, we see that the density of coverage for all azimuths is more consistent and we manage to capture some of the smaller dip angles (less than 10°) associated with the dip angle. Figure 38D demonstrates what happens if we increase our cable spacing to 1000 m in the x and y direction, still using shotlines at 100 m spacing. We see that we forfeit some of the smaller dip angles, but we maintain consistent coverage throughout the sampled area.

From these tests, we choose to use the results obtained in Figure 38C for the relative resolution analysis of the vertical cable data with towed-streamer and OBC data. Again, this is justified by the ease of data acquisition in the marine vertical cable survey

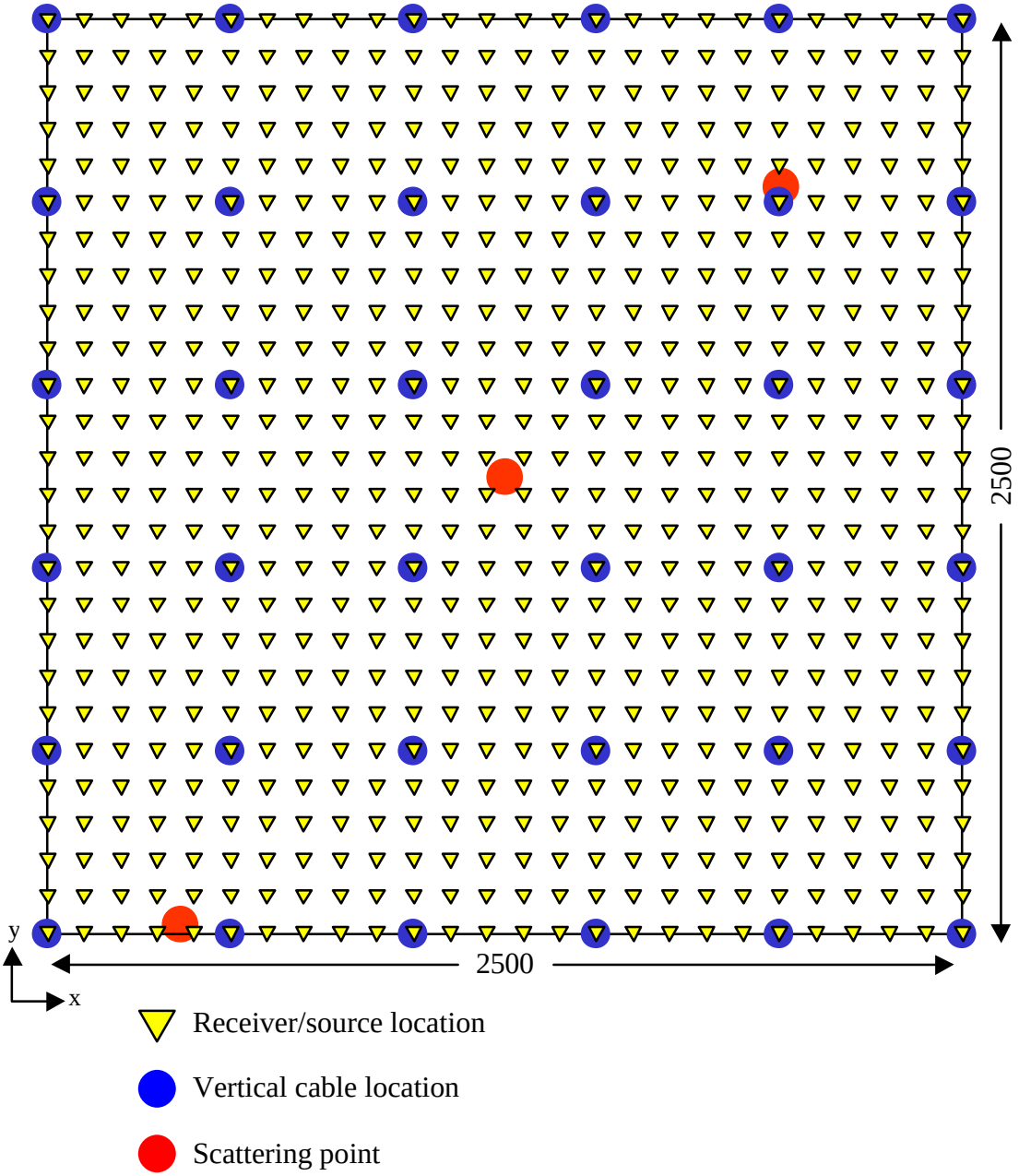

Figure 37. Acquisition geometry for OBC, land and vertical cables surveys. There are 26 horizontal receiver lines at 100 m intervals, each line consisting of 101 receivers at 25 m intervals. Source and receiver postions are coincident. The scattering point locations are at (1250, 1250, 2000), (450, 5, 2000) and (2000, 2050, 2000).

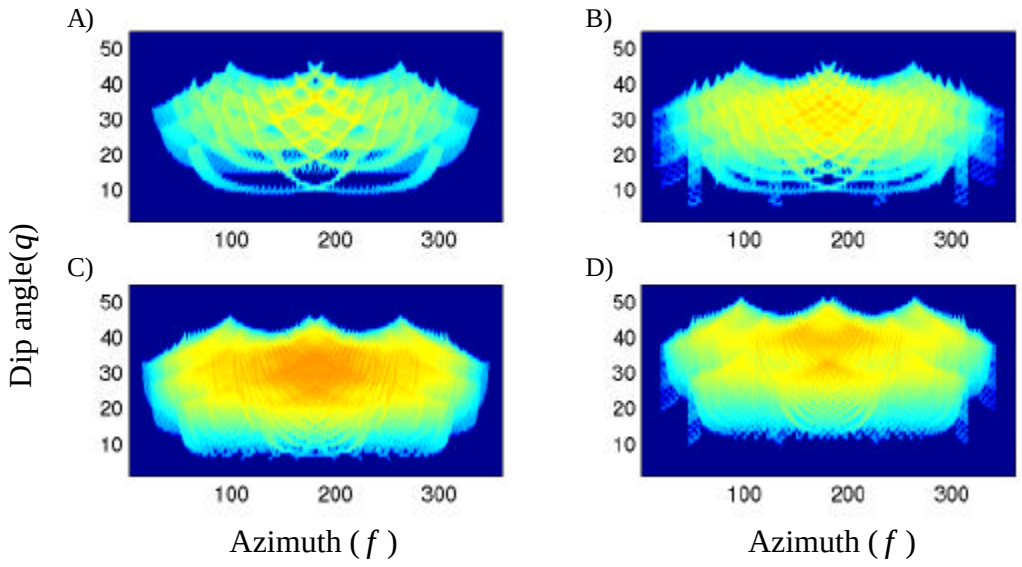

Figure 38. Resolution analysis for various vertical cable acquisition parameters. Figures A, B and C use vertical cables at 500 m intervals in the x and y directions with each cable length being 500 m. The number of source lines varies from 6, 11 and 26 for A, B and C, respectively. Plot D corresponds to vertical cable spacing of 1000 m in the x and y direction and 26 source lines. The scattering point is located at (1250, 1250, 2000) as seen in Figure 37.

namely, once the cables are deployed, the seismic vessel tows only the source array along parallel lines.

The towed-streamer acquisition geometry is unique in that the source position relative to the streamers is always the same. Figure 39 illustrates the towed-streamer acquisition geometry we use in our resolution analysis. We limit our source positions to a 2500 m by 2500 m area. We use 12 streamers with a streamer spacing of 50 m. The source to streamer offset is 150 m. The source line spacing is 500 m and each source line has 101 shotpoints at 25 m intervals. Figure 40 shows the resulting relative coverage for

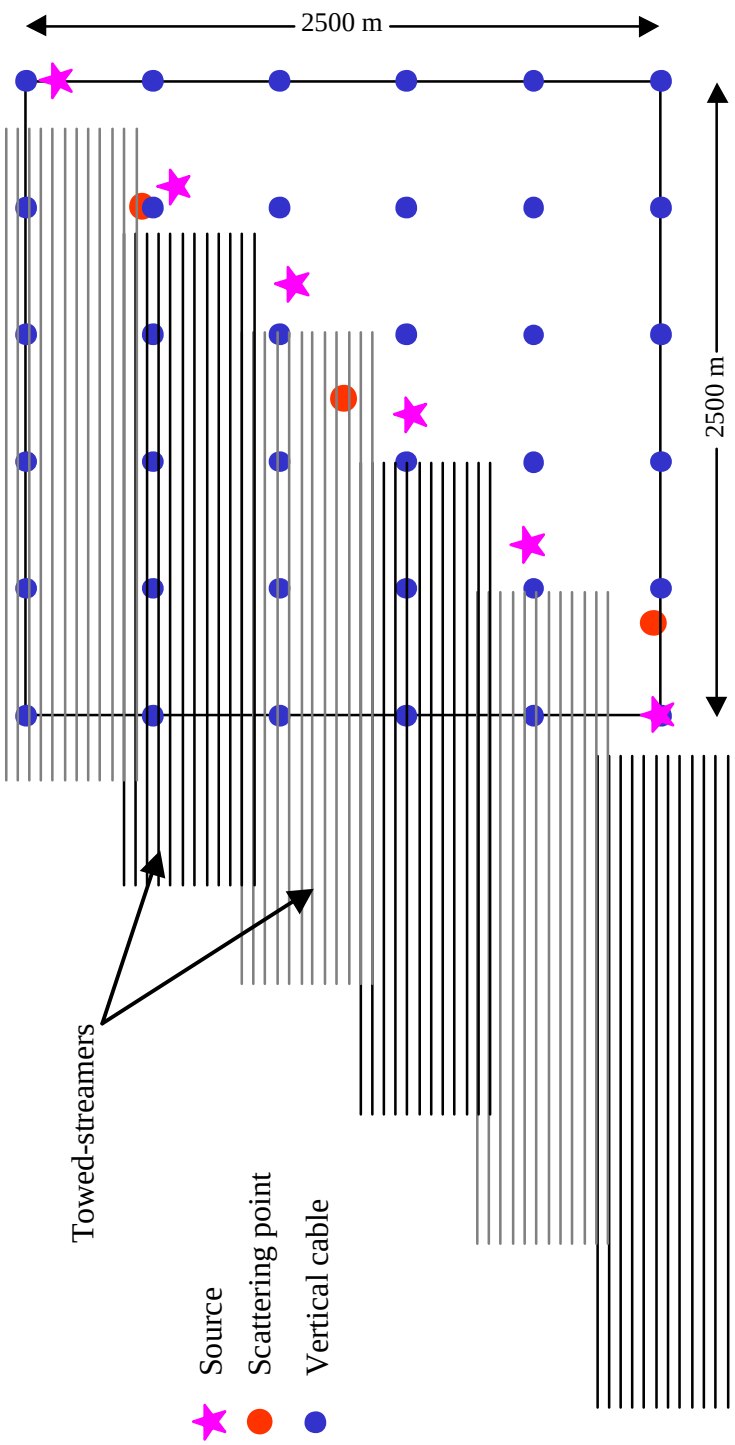

Figure 39. Towed-streamer acquisition geometry used for resolution analysis. Each source line consists of 101 shotpoints at 25 m intervals. Twelve streamers are used, each streamer contains 101 receivers at 25 m intervals. The scattering points are located at (1250, 1250, 2000), (450, 5, 2000) and (2000, 2050, 2000).

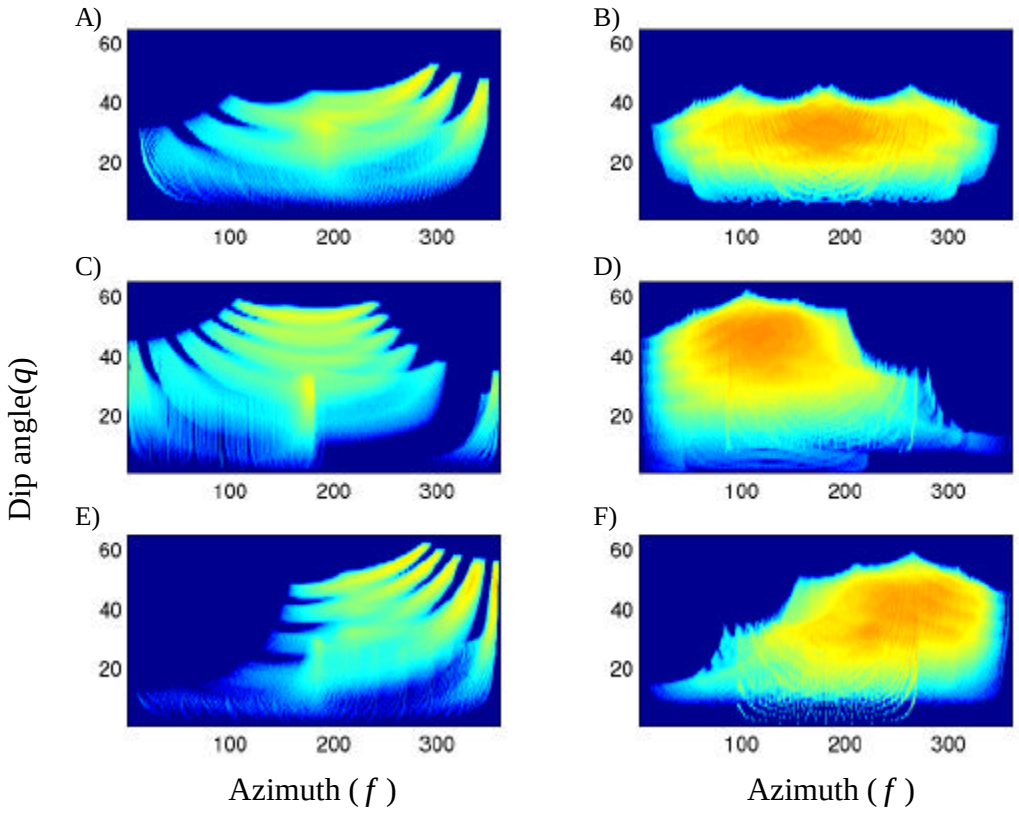

Figure 40. Resolution analysis for towed-streamer data and vertical cable data corresponding to three scattering point locations: (1250, 1250, 2000) in A and B, (450, 5, 2000) in C and D, and (2000, 2050, 2000) in E and F. The towed-streamer data (A, C, E) lacks uniform coverage due to the source-receiver geometry while the vertical cable data (B, D, F) provides higher density and uniform coverage within the sampled ranges.

the towed-streamer data and the vertical cable data at the three scattering points as shown in Figure 39. The towed-streamer data lacks uniform coverage and symmetry due to the asymmetric source-receiver configuration and interval between source lines. The vertical cable data provides higher density and uniform coverage relative to the towed-streamer data.

OBC vs. marine vertical cable

Now we would like to compare the relative resolution between OBC data and vertical cable data. Since we are still in the marine environment, we use the same parameters for the vertical cable data as the previous example. Receiver line deployment for the OBC data is much more difficult compared to vertical cable surveying. Issues like receiver coupling and positioning require more attention, especially with an undulating seafloor. For this resolution analysis, we use 26 receiver lines, each with 101 receivers at 25 m intervals, seen in Figure 37, and assume a flat seafloor. The resultant relative coverage for three scattering points is seen in Figure 41. The OBC data provide higher density and more uniform coverage for all azimuthal and dip angles. Furthermore, OBC surveying provides small dip angle (less than 10°) hits not recorded by the vertical cable data at many scattering points due to the larger intervals between vertical cable positions.

Land surface seismic vs. vertical cable

Up to this point, we have only considered the 3-D geometries associated with marine surveys. Here, we will analyze the resolution associated with land surveying. Land vertical cable surveying requires holes to be drilled at each vertical cable location. Deeper holes and smaller cable spacing provide higher resolution data but result in higher costs as well. Herein lies the challenge of balancing cable hole drilling costs and desired data resolution. We will analyze the resolution of vertical cable data with respect to three parameters to determine adequate sampling: 1) distance between vertical cables,

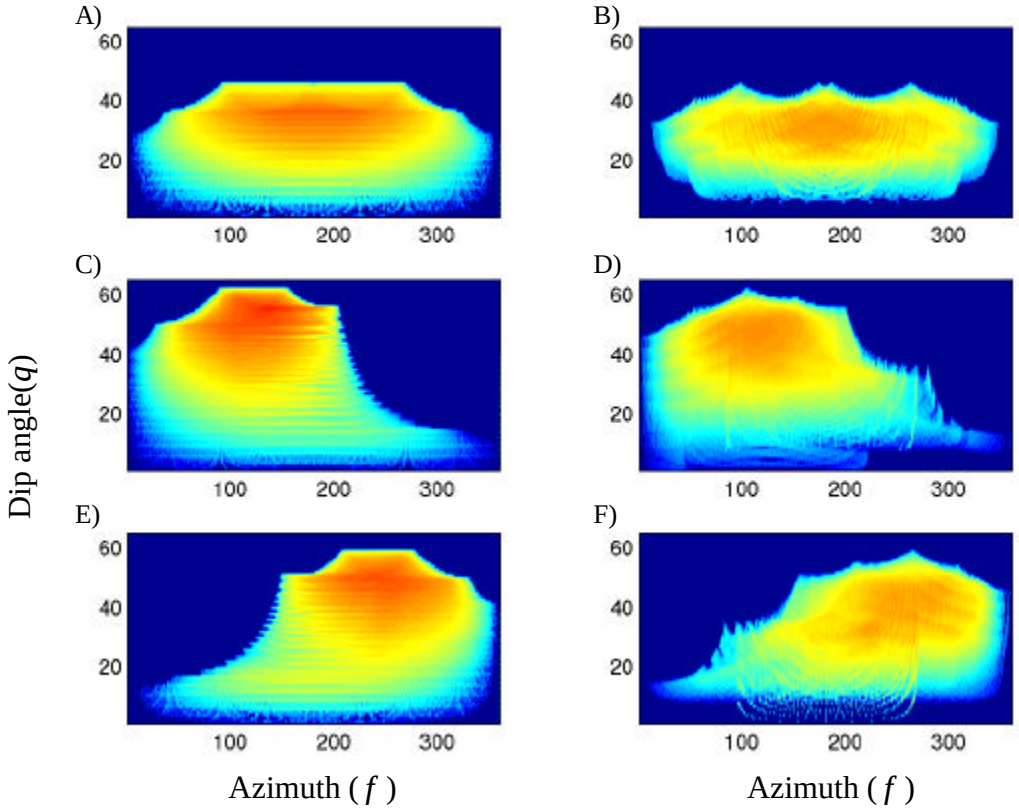

Figure 41. Resolution analysis for OBC data and vertical cable data corresponding to three scattering point locations: (1250, 1250, 2000) in A and B, (450, 5, 2000) in C and D, and (2000, 2050, 2000) in E and F. The OBC data (A, C, E) provides better resolution with higher density and uniform coverage within the sampled ranges compared to the vertical cable data.

2) depth of vertical cables, and 3) sampling density along each vertical cable. Figure 42 shows the relative coverage of vertical cable data using various acquisition parameters for a scattering point located in the center of the survey area. To obtain the coverage in Figure 42A, we use a cable spacing of 500 m and cable length of 500 m, with a sampling interval of 12.5 m along each cable. If we reduce the cable length to 250 m, we obtain

the coverage in Figure 42B and C, with the data in B using 12.5 m receiver intervals and the data in C using 6.25 m receiver intervals along each cable. What we see here is that even though we half the cable length, we can still acquire high density and uniform coverage for a scattering point by increasing the density of sampling along each vertical cable. Figure 42D corresponds to a cable interval of 1000 m and cable length of 250 m, maintaining the 6.25 m sampling interval along each cable. The relative coverage compared to Figure 42A is not as dense with a decrease of coverage of small reflection angles due to the large cable spacing and scatter point location.

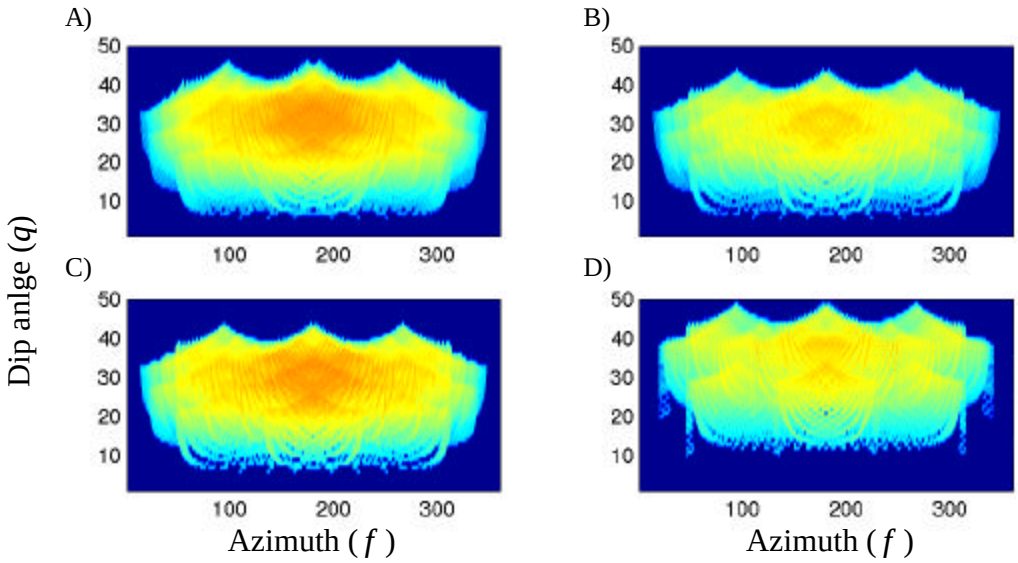

Figure 42. Resolution analysis for various vertical cable acquisition parameters in land scenario. Figures A uses vertical cables at 500 m intervals in the x and y directions with a cable length of 500 m. By reducing the cable length to 250 m, we produce the resolution plots in B and C, where the sampling along the cable is 12.5 m in B and 6.25 in C. Plot D corresponds to vertical cable spacing of 1000 m in the x and y direction The scattering point is located at the center of the survey area, (1250, 1250, 2000) as seen in Figure 37.

Since the relative coverage between Figures 42A and 42C is similar, we choose to use the 250 m cable length which would reduce acquisition costs.

The relative coverage between land surface seismic and vertical cable surveying is shown in Figure 43 for several scattering points corresponding to the survey design in Figure 37. The surface survey consists of 26 receiver lines with 101 receivers at 25 m intervals. The vertical cable survey uses 250 m cables at 500 m intervals with a receiver spacing 6.25 m along each cable. For both surveys, source positions are coincident with the surface receiver positions of the surface survey, such that there are 26 source lines with 101 shotpoints at 25 m intervals. Figure 43A and B show the relative coverage between the surface and vertical cable survey for a scattering point in the middle of the survey area (Figure 37). The land data captures more small angle reflections, higher density of total coverage and more uniform distribution of coverage compared to the vertical cable data. However, we see that the relative difference of coverage between the surface and vertical cable data is quite similar. Therefore, by using 250 m long cables at 500 m intervals, we can achieve near equivalent resolution compared to surface methods on land.

In summary, the implementation of vertical cable surveying requires different cable lengths and spacing to be economical compared to current horizontal methods. In the marine case, cable length is dependent on water depths, and cable spacing is dependent on the number of available cables. We have demonstrated superior resolution for marine vertical cable surveys relative to towed-streamer surveying and near equivalent resolution of marine vertical cable surveys and OBC surveys, as seen in

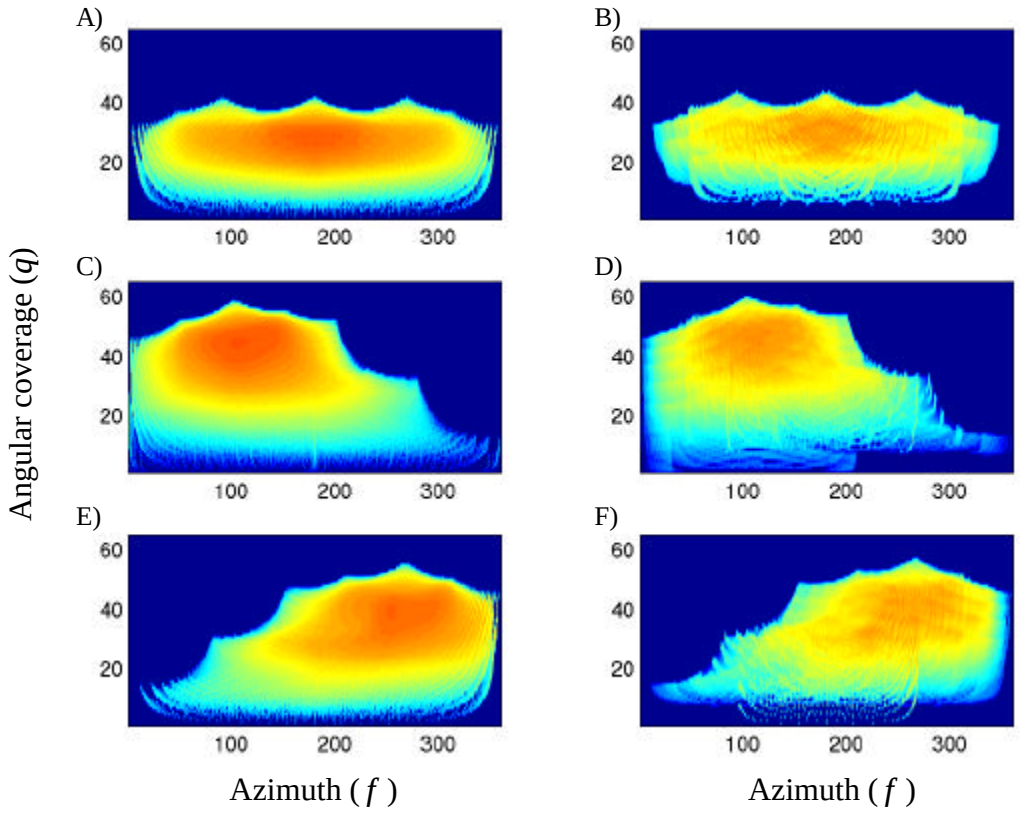

Figure 43. Resolution analysis for land surface seismic data and land vertical cable data corresponding to three scattering point locations: (1250, 1250, 2000) in A and B, (450, 5, 2000) in C and D, and (2000, 2050, 2000) in E and F. The land data (A, C, E) provides better resolution with higher density and uniform coverage within the sampled ranges compared to the vertical cable data. The vertical cable data uses 250 m long cables at 500 m intervals.

Figure 44. On land, the cable length may have to be decreased to make vertical cable surveying economic and a viable alternative to land surface surveying. We have demonstrated near equivalent relative resolution between vertical cable surveys using cable lengths of 250 m and surface land seismic data, as seen in Figure 44. In addition,

this analysis does not take into account coupling and data quality, which as we will see in Chapter V, make land vertical cable more attractive.

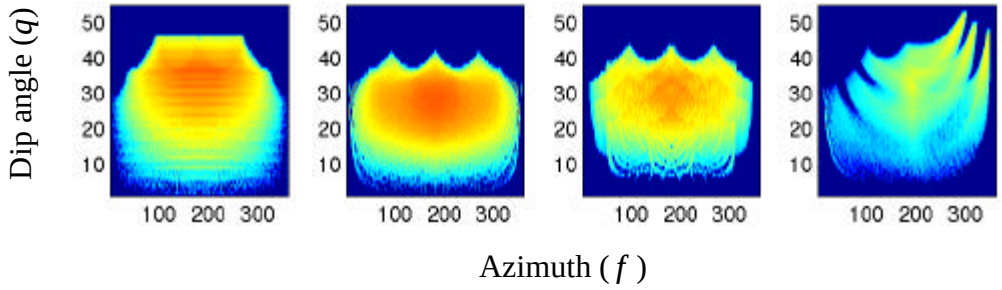

Figure 44. Relative resolution between OBC, land surface seismic, vertical cable and towed-streamer data for an image point located at the center of the survey area.

CONCLUSIONS

In the 2-D case, we have demonstrated that the imaging resolution of vertical cables can be superior to surface seismic methods for an image point, horizontal reflector and a dipping reflector. For a single point scatterer or image point, we analyze the image resolution by comparing the occurrence of rays between the vertical and horizontal receiver distributions. We find that for instance a vertical cable survey with 6 cables spaced every 500 m using 26 receivers at 20 m intervals achieves superior imaging resolution compared to the horizontal surface method consisting of 101 receivers spaced every 25 m. By treating the reflector as a series of closely spaced

scattering points, we were able to extend the resolution analysis of a point scatterer to horizontal reflector as well as a dipping reflector. Again, we find that 5 cables spaced every 625 m with a receiver interval of 12.5 m can achieve superior imaging resolution compared to the horizontal surface method consisting of 101 receivers spaced every 25 m.

Our resolution analysis using 3-D geometries provides us with encouraging results. In marine surveys, vertical cable surveying using 500 m cable intervals provides better resolution compared to towed-streamer surveys. Vertical cable surveying also provides near equivalent resolution compared with OBC data, without the expensive cable deployment. On land, vertical cables limited to 250 m at 500 m intervals can provide near equivalent resolution relative to surface seismic surveys. Vertical cable surveys have limited small dip angle (less than 10°) coverage at some image points due to the vertical cable spacing.

CHAPTER IV

MULTIPLE ATTENUATION OF MARINE VERTICAL CABLE DATA

INTRODUCTION

Marine vertical cable data contain primaries, multiples and ghosts just like traditional towed-streamer data. However, a unique approach must be taken when processing these events in a vertical cable experiment. Because the receiver ghost is well separated from the primary in vertical cable data, the traditional imaging algorithms used are being modified and/or abandoned. The emerging vertical cable imaging algorithms can use either the reflected primaries or the receiver ghost of primaries. Therefore, Ikelle (2001) has developed a method based on the inverse scattering series for attenuating free-surface multiples and receiver ghosts while preserving primaries, as well as an algorithm for attenuating primaries, free-surface multiples and receiver ghosts of multiples while preserving only receiver ghosts of primaries for vertical cable data. We use these results in this thesis.

The inverse scattering technique described by Carvalho and Weglein (1991), Ikelle and Weglein (1996), Matson and Weglein (1996), Weglein et al. (1997) and Ikelle (1999) is a model and subtract method for removing free-surface multiples from towed-streamer, VSP and ocean bottom cable data. The demultiple task is divided into two parts. First, a finite number of free-surface multiples are predicted from the field data.

Then, each order of free-surface multiple is scaled and subtracted from the data. This method is multi-dimensional and does not make any assumptions about the seafloor or the subsurface. The subtraction process does require knowledge of the source signature.

In adapting this method to vertical cable data (Ikelle 2001), or VSP data as in Ikelle and Weglein (1996), the key assumption is that surface seismic data be available alongside the vertical cable data. This assumption is often met since vertical cable experiments often occur in areas where surface seismic has failed. If towed-streamer data is not available, surface data can be constructed from the vertical cable data after an up/down wavefield separation and extrapolation of the up-going wavefield to the surface.

In the case of preserving the receiver ghost of primaries, the direct wave must be muted from the vertical cable data. As long as the direct arrivals are well separated from the primaries and refracted arrivals, this is not a problem. If the direct arrivals coincide with the primaries or other events, the recent method of removing direct arrivals based on a model then subtract approach by Ikelle et al. (1999b) can be used.

In this chapter, we define pertinent seismic events and discuss the reasoning for preserving the receiver ghosts of primaries. We then introduce the scattering series adapted to vertical cable data and explain the methodology for preserving primaries or receiver ghosts of primaries. We will follow with synthetic examples to demonstrate the effectiveness of these algorithms.

Seismic Events

Due to the geometry of the cables in a vertical cable experiment, it is important to take a moment to define the associated seismic events. We define free-surface multiples as up-going energy which has at least one reflection from the free surface, or water-air interface. These events carry the same information as the primary reflections so they offer no additional information about the subsurface and are considered noise.

Free-surface multiples can be further distinguished by the number of reflections from the free surface, i.e., one bounce is a first-order free-surface multiple, two bounces corresponds to a second-order free-surface multiple, and so on. Free-surface multiples and other seismic events are shown in Figures 45 and 46 for a streamer survey and vertical cable survey, respectively.

A ghost is defined as either up-going energy that travels directly from the source to the free surface and is reflected downward or down-going energy that travels from the free surface directly to the receivers. Ghosts are associated with the source position, referred to as source ghosts, and the receiver positions, or namely, receiver ghosts. The raypaths of ghost events associated with a towed-streamer survey are shown in Figure 47.

The source ghost travels directly from the source to the free surface and is reflected back down as seen in Figure 47B. Since the distance from the source to the surface is small compared to the wavelength of the seismic signal in both streamer and vertical cable surveys, the source ghosts are negligible and are treated as part of the effective source signature, or apparent source.

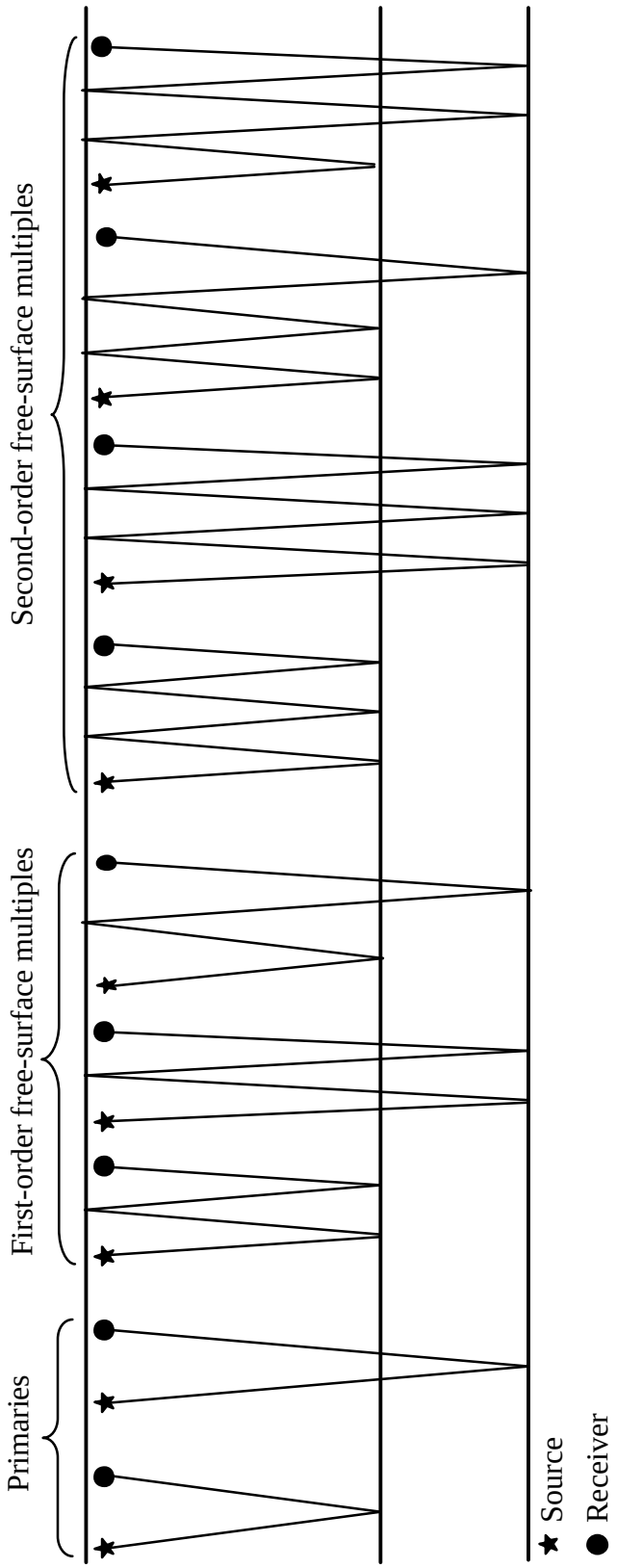

Figure 45. Example of primary events and free-surface multiples for streamer experiment. Free-surface multiples are defined as up-going energy with at least one reflection from the air-water interface. One reflection from the free surface is a first-order multiple, tow reflections is a second-order multiple and so on.

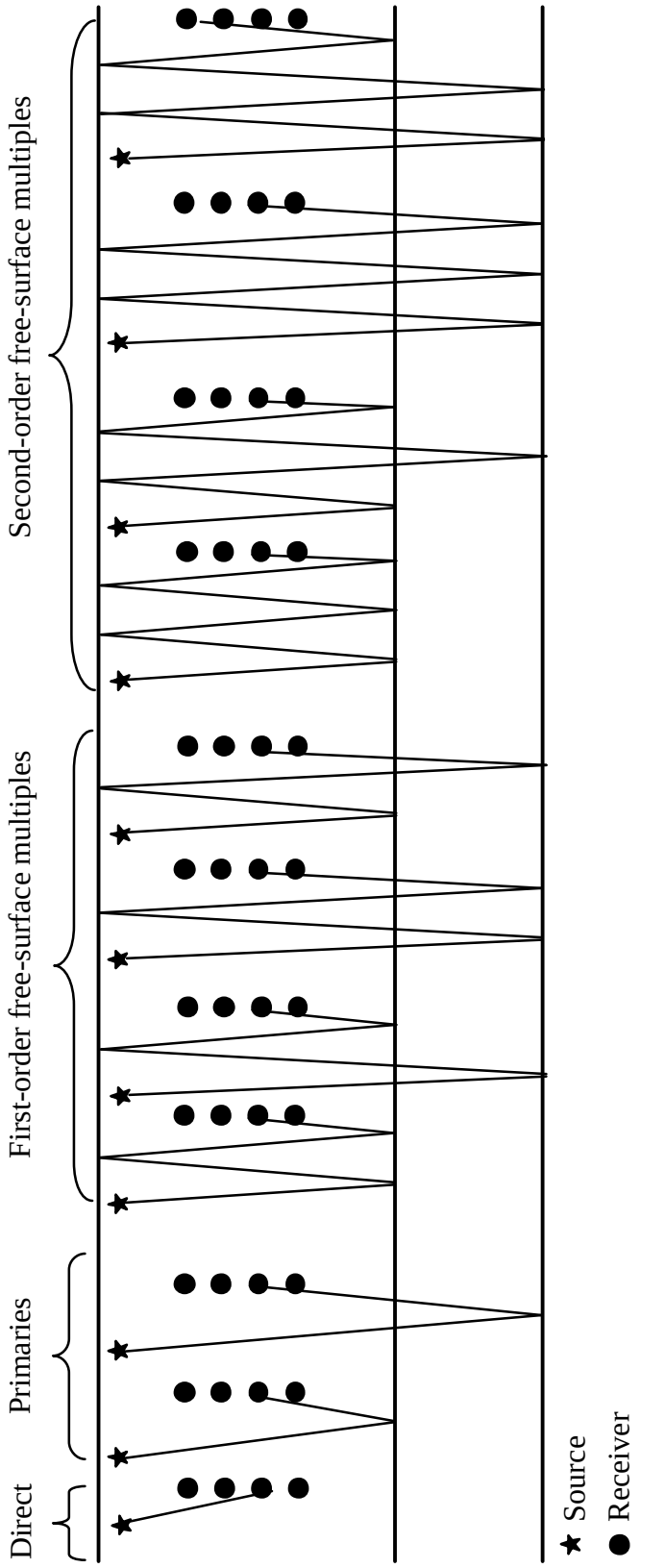

Figure 46. Example of direct arrival, primary events and free-surface multiples for vertical cable experiment.

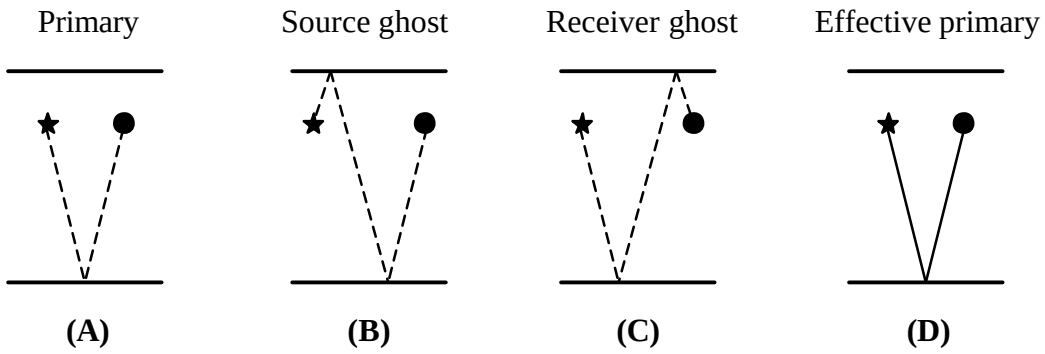

Figure 47. Example of raypaths associated with a primary (A) and its source ghost (B) and receiver ghost (C) in a streamer experiment. We treat these three events as the effective, or apparent, event seen in (D). The source and receiver depths are exaggerated for illustration.

Receiver ghosts are associated with energy coming from the subsurface, bouncing off the free surface and returning directly to the receivers as seen in Figure 47C. In the towed-streamer experiment, the distance between the free surface and receiver is small. Thus, we can treat the receiver ghost as part of the effective arrival for that particular seismic event.

So, the effective primary contains contributions from the primary event, source ghost and receiver ghost, ass seen in Figure 47. Again, since the source and receiver depths are small relative to the wavelength of the signal, the ghost effects are negligible and can be processed as part of the apparent signal.

In vertical cable surveys, the receiver to surface depth is very relevant; making the receiver ghosts a major concern. The vertical position of receivers results in time delays between the primary events and receiver ghosts as illustrated by raypaths in Figure 48. The receiver ghosts are separate, distinct events of the seismogram. The

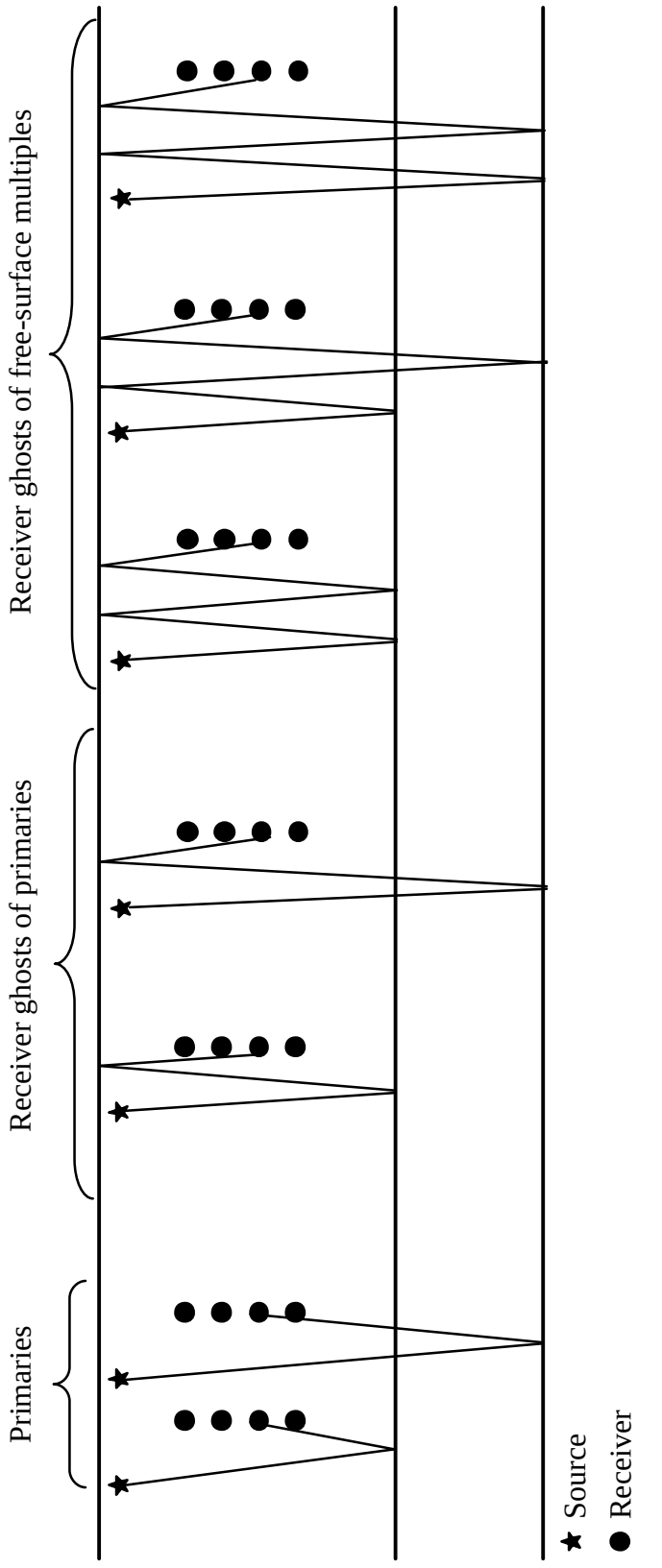

Figure 48. Example of primaries and receiver ghosts for vertical cable experiment.

receiver ghosts can further be classified based upon their reflections from the free surface. One reflection would be a first-order receiver ghost, or simply a receiver ghost of the primary; two reflections would be a second-order receiver ghost, or receiver ghost of the free-surface multiple, and so on. As noted earlier, some imaging algorithms attempt to use the receiver ghosts of primaries. Therefore, let us discuss these events in more detail.

The motivation for using receiver ghost of primaries rather than the primaries themselves can best be demonstrated using raypaths. Figure 49 illustrates the raypaths for a primary and receiver ghost of the primary for a series of source positions into a receiver. The primary reflection points occur over length R_p. The receiver ghost reflection points occur over length R_g. Distance R_g is greater than R_p, hence the receiver ghosts provide a larger subsurface aperture. However, the primary reflections occur closer to the receiver position and at a higher density relative to the receiver ghost reflections, which can be very beneficial in areas of steep dip (Guimaraes et al, 1998). Therefore, the ability to separate these events and use them independently or dependently can aid in imaging complex structures.

INVERSE SCATTERING MULTIPLE ATTENUATION (ISMA)

ISMA is a model and subtract data dependent technique that removes first and higher-order free-surface multiples while preserving primary energy, doing so with no knowledge of the subsurface. This is accomplished in a two-step process. First, a finite

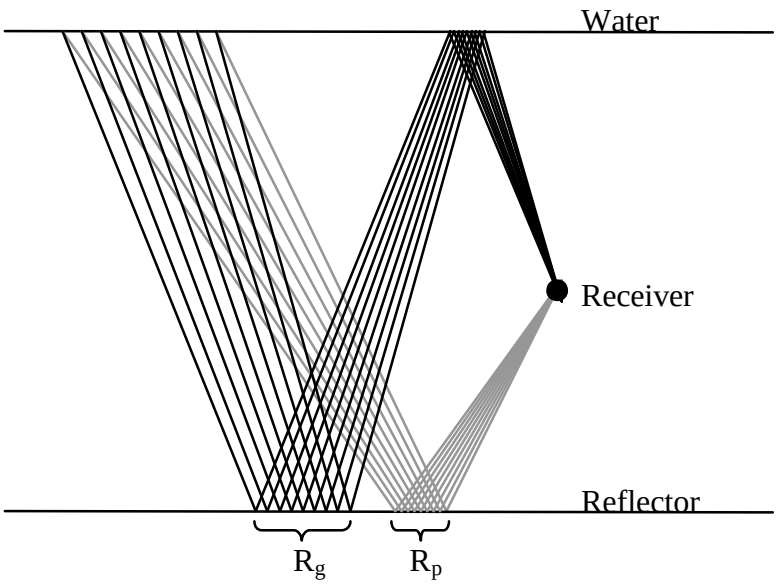

Figure 49. Difference of subsurface aperture for a series of primaries and receiver ghosts. The gray raypaths are the primaries and the black raypaths are the receiver ghosts. Distance R_g, corresponding to the receiver ghosts subsurface aperture, is larger than R_p, the subsurface aperture for the primaries. However, R_p has a greater density of sampling and is closer to the receiver compared to R_g. Adapted from Guimaraes, et al. (1998).

number of free-surface multiples are predicted. Then, each multiple wavefield is scaled and subtracted from the original data set.

The predictive process is similar to the retro-correlation, or auto-convolution, describe by Anstey (1966) and Anstey and Newman (1966). They demonstrated that the convolution of a seismic trace with itself would produce all orders of multiples contained within the original seismic trace, albeit with incorrect amplitude. They also demonstrated that in this process, primary events could not be generated.

Ikelle and Weglein (1996) have shown the inverse scattering series for the streamer experiment can be expressed in the following, simplified equation:

$$\mathbf{D}_p = \mathbf{D}_0 + \mathbf{A}\mathbf{D}_1 + \mathbf{A}^2\mathbf{D}_2 + \mathbf{A}^3\mathbf{D}_3 + \ldots, \qquad (23)$$

where

$$\mathbf{D}_n = \mathbf{D}_0\mathbf{G}_0^{-1}\mathbf{D}_{n-1}, \qquad n = 1,2,3,\ldots. \qquad (24)$$

$\mathbf{D}_p$ is the data without the free-surface multiples. $\mathbf{D}_0$ is the actual streamer data. . $\mathbf{D}_1$ corresponds to the first-order free-surface multiples, $\mathbf{D}_2$ corresponds to the second-order free-surface multiples, and so on. $\mathbf{A}$ is the inverse source signature and $\mathbf{G}_0^{-1}$ is the inverse Green's function describing wave propagation in a homogeneous acoustic medium, in the marine case, water

To adapt this method to vertical cable data, a complimentary wavefield must be used which contain raypaths needed for the construction of the multiples and receiver ghosts contained in the vertical cable data. Thus Eq. (24) is rewritten as

$$\mathbf{D}_n = \mathbf{E}_0\mathbf{G}_0^{-1}\mathbf{D}_{n-1}, \qquad n = 1,2,3,\ldots, \qquad (25)$$

where $\mathbf{E}_0$ is a complimentary wavefield and $\mathbf{D}_0$ is the vertical cable data. For this work, we simulate streamer data and vertical cable data simultaneously and use the streamer data as the complimentary wavefield, $\mathbf{E}_0$. Ikelle (2001) has also proposed that the complimentary wavefield can be generated from the vertical cable data by performing an up/down separation and extrapolating the up-going wavefield up to the sea surface. Also, Ikelle and Weglein (1996) have proposed using a seafloor model to generate the complimentary wavefield. This latter method assumes the seafloor is mainly responsible for generating multiples and the bathymetry is known.

Attenuating free-surface multiples and receiver ghosts while preserving primaries

Using the streamer data, $\mathbf{E}_0$, and vertical cable data, $\mathbf{D}_0$, we can now properly formulate the inverse scattering series for removing the free-surface multiples and receiver ghosts of vertical cable data. The only requirement of the streamer data is that the direct wave be muted. The direct wave is typically well separated from the reflected events in deep water. In this case, the direct wave can simply be muted. If the direct wave arrival coincides with reflected arrivals, the "model and subtract" approach proposed by Ikelle et al. (1999b) can be used to remove the direct wave in the streamer data.

The inverse scattering series can be formulated using the following notation. Let (x_s,z_s) denote the source position and (x_r,z_r) denote the receiver position, such that the streamer data is given by $E_0(x_s, z_s, t; x_r, z_r)$ and the vertical cable data is given by $D_0(x_s, z_s, t; x_r, z_r)$, where t is the time the source is activated. We set t equal to zero for each source activation. We datum the source depth and streamer receiver depth to zero for all positions, resulting in $E_0(x_s, x_r, t)$ for the streamer data and $D_0(x_s, x_r, z_r, t)$ for the vertical cable data.

For working in the Fourier domain, we introduce the variables k_s, k_r, and w as the transform pairs for x_s, x_r, and t, respectively. The 2D forward Fourier transform for a continuous function $f(x,t)$ is defined as

$$F(k,w) = \int_{-\infty}^{\infty}\int_{-\infty}^{\infty} f(x,t)e^{-i2p(kx+wt)}dxdt, \qquad (26)$$

and the inverse 2D forward Fourier transform defined as

$$f(x,t)=\int_{-\infty}^{\infty}\int_{-\infty}^{\infty}F(k,w)e^{i2p\,(kx+wt)}dkdw. \qquad (27)$$

The series is constructed similar to that of the demultiple of walkaway VSP data (Ikelle and Weglein, 1996) or OBC data (Ikelle, 1999) and is written as

$$D_p(x_s, x_r, z_r, w)=D_0(x_s, x_r, z_r, w)+A(w)D_1(x_s, x_r, z_r, w)$$

$$+A^2(w)D_2(x_s, x_r, z_r, w)+A^3(w)D_3(x_s, x_r, z_r, w)+\ldots, \qquad (28)$$

where $D_p(x_s, x_r, z_r, w)$ is the data without free-surface multiples and receiver ghosts, $D_0(x_s, x_r, z_r, w)$ is the vertical cable data and $A(w)$ is the Fourier transform of the inverse source signature which is assumed to be only time dependent. The free-surface multiple and receiver ghost wavefields $D_1(x_s, x_r, z_r, w)$ and $D_2(x_s, x_r, z_r, w)$,etc. are defined as

$$D_n(x_s, x, z_r, w)=\int_{-\infty}^{\infty}E_0'(x_s, k, w)D_{n-1}(k, x_r, z_r, w)\,dk, \qquad n=1,2,3\ldots, \qquad (29)$$

where

$$E_0'(x_s, k, w)=\frac{w}{c}\cos q\;\; E_0(x_s, k, w), \qquad (30)$$

and

$$\cos q=\sqrt{1-\frac{c^2k^2}{w^2}}\,. \qquad (31)$$

Cosq is the obliquity factor where *c* is the velocity of water and *k* is the generic horizontal wavenumber. The proof of equations (28)-(31) is demonstrated by Ikelle

(1996) and can found by substituting $D_p(x_s, x_r, z_r, t)$, $E_0(x_s, x_r, t)$ and $D_0(x_s, x_r, z_r, t)$ and the inverse of the Green's function for a homogeneous medium into equation (23) and (25). The inverse of the Green's function for a homogeneous medium is given by

$$G_0^{-1}(x,0,w;k_x,0) = 4piq\exp\{ ik_x x\}, \qquad (32)$$

where

$$q = \frac{w}{c}\sqrt{1-\frac{k_x^2 c^2}{w^2}}\,. \qquad (33)$$

From equation (29), we see that the prediction of the first-order multiples and receiver ghosts are constructed by a convolution over the wavenumber domain for each frequency of the streamer data with the vertical cable data with respect to the source and receiver positions. Thus, a streamer event is joined with a vertical cable event when the receiver position of the streamer event and the source position of the vertical event coincide The physical interpretation of equation (29), using streamer data as complimentary wavefield, can be seen in Figure 50. The original vertical cable data, $\mathbf{D}_0$, is convolved with the streamer data, $\mathbf{E}_0$. This generates the wavefield $\mathbf{D}_1$, which contains first-order free-surface multiples and receiver ghosts with correct travel times, as well as higher-order multiples and ghosts with the correct travel times but not the proper amplitudes. Using higher-order terms in the series corrects these scaling problems. Wavefield $\mathbf{D}_1$ is then convolved with the streamer data, $\mathbf{E}_0$, to generate the wavefield corresponding to the second-order free-surface multiples, $\mathbf{D}_2$, and receiver ghosts. This process is carried out to $\mathbf{D}_n$. Wavefields $\mathbf{D}_1$, $\mathbf{D}_2$, $\mathbf{D}_3$, ...$\mathbf{D}_n$ are then scaled by $\mathbf{A}$ and

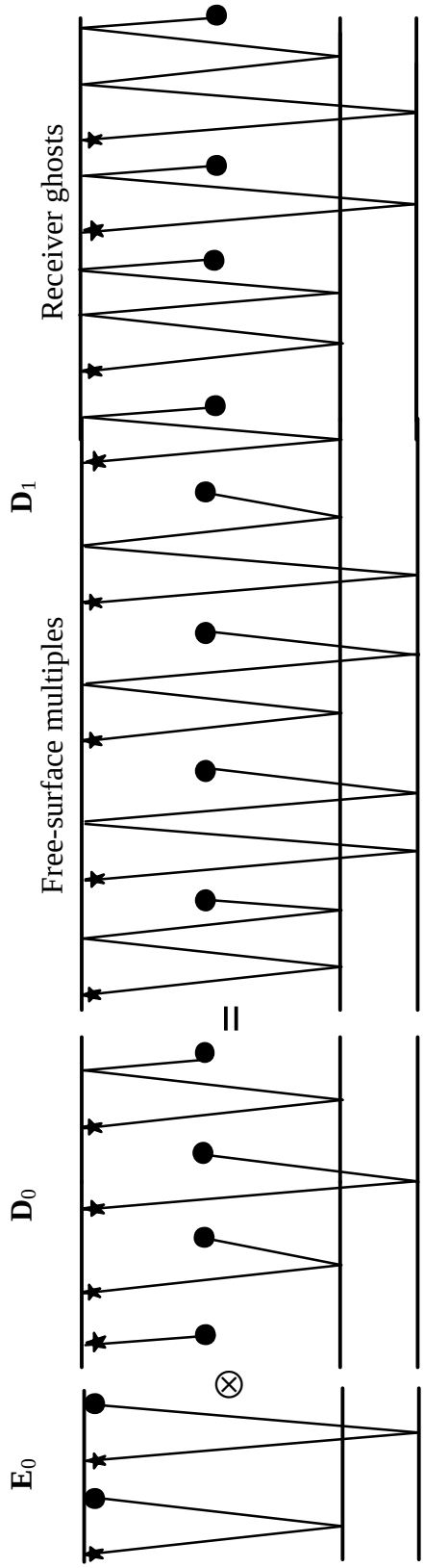

Figure 50. Physical interpretation of the construction of the $\mathbf{D}_1$ term for vertical cable data using vertical cable data, $\mathbf{D}_0$, and streamer data, $\mathbf{E}_0$, as a complimentary wavefield. Here, we see the construction of the first-order free-surface multiples and receiver ghosts. The $\otimes$ denotes convolution. The streamer data provides the missing raypaths needed to construct the events in $\mathbf{D}_1$.

subtracted from $\mathbf{D}_0$, effectively removing free-surface multiples and receiver ghosts to order *n*. It is important to note that primaries can never be modeled in this process, thus primaries are never directly subtracted out of the original data.

As stated previously, A(w) is the inverse source signature, such that A(w)=1/ S(w). S(w) is estimated as done in Ikelle et al. (1997). The authors formulate the problem of estimating the source signature by finding the S(w) that best reduces or minimizes the energy content of the seismic data, $\mathbf{D}_p$, after removal of the first-order free-surface multiples, $\mathbf{D}_1$. This assumption is based on the idea that the energy content of the seismic data should be less after the removal of the first-order free-surface multiples. This same source signature can then be used to attenuate all orders of free-surface multiples.

Therefore, the authors begin the estimation of S(w) by truncating the series in equation (28) to

$$D_p(x_s, x_r, z_r, w) = D_0(x_s, x_r, z_r, w) + A(w)D_1(x_s, x_r, z_r, w). \qquad (34)$$

To find $A(w)$, they minimize

$$S(\mathbf{A}) = \|\mathbf{D}_p\|^2 + \|\mathbf{A}\|^2, \qquad (35)$$

where

$$\|\mathbf{D}_p\|^2 = \iiint D_p(k_s, k_g, w) W_D(k_s, k_g, w) D_f^*(k_s, k_g, w)\, dw\ dk_s\ dk_g \qquad (36)$$

and

$$\|A\|^2 = s^2 \iint A(w) W_A^{-1}(w, w') A^*(w')\, dw'\, dw. \qquad (37)$$

The variables k_s, k_r, and w correspond to the Fourier transform variables x_s, x_r, and t. W_D and W_A are weighting functions describing errors in the data and a priori information about the source, respectively. s^2 is a constant. The asterisk (*) denotes the complex conjugate.

After some optimization algebra, similar to Ikelle et al. (1986), they arrive at

$$A^{(0)}(w) = -\frac{\int W_A(w,w')N(w')dw'}{s^2 + \int W_A(w,w')Q(w')dw'}, \qquad (38)$$

where

$$N(w) = \iint D_0(k_s,k_g,w)W_D(k_s,k_g,w)D_1^*(k_s,k_g,w)\,dk_s dk_g \qquad (39)$$

and

$$Q(w) = \iint D_1(k_s,k_g,w)W_D(k_s,k_g,w)D_1^*(k_s,k_g,w)\,dk_s dk_g . \qquad (40)$$

$A^{(0)}(w)$ is the first estimation of the source which removes a significant amount of multiple energy. We see that the source is estimated by a crosscorrelation of the data, $\mathbf{D}_0$, with the predicted first-order free-surface multiples, $\mathbf{D}_1$, where W_D is a weighting function which windows the first-order free-surface multiple events. This crosscorrelation, which measures the similarity between $\mathbf{D}_0$ and $\mathbf{D}_1$, is normalized by the autocorrelation of the predicted first-order free-surface multiples, $\mathbf{D}_1$, using W_D to window the events. The autocorrelation contains all the amplitude and frequency information contained in $\mathbf{D}_1$. Multiple iteration of $A^{(n)}(w)$ can be calculated if noticeable residual energy is left after the first iteration. For a more in depth discussion of the source estimation, please refer to Ikelle et al. (1997).

Attenuating free-surface multiples and their receiver ghosts while preserving primaries and their receiver ghosts

Now, we want to preserve primaries and their receiver ghosts while removing free-surface multiples and receiver ghosts of free-surface multiples. This is accomplished by removing the direct wave from the vertical cable data. Thus, the series in equation (28) becomes

$$D_{PG}(x_s, x_r, z_r, w) = D_0^{(wd)}(x_s, x_r, z_r, w) + A_G(w) D_1'(x_s, x_r, z_r, w)$$

$$+ A_G^2(w) D_2'(x_s, x_r, z_r, w) + A_G^3(w) D_3'(x_s, x_r, z_r, w) + \ldots, \qquad (41)$$

where

$$D_n'(x_s, x, z_r, w) = \int_{-\infty}^{\infty} E_0'(x_s, k, w) D_{n-1}'(k, x_r, z_r, w)\, dk, \qquad n = 1,2,3\ldots. \qquad (42)$$

Here, $\mathbf{D}_{PG}$ contains only primaries and the receiver ghosts of primaries. $\mathbf{D_0^{(wd)}}$ is now the vertical cable data without the direct arrival, such that $\mathbf{D_0'} = \mathbf{D_0^{(wd)}}$. $\mathbf{A}_G$ is the Fourier transform of the inverse source signature which is assumed to be only time dependent. The wavefields $\mathbf{D}_1'$, $\mathbf{D}_2'$, … $\mathbf{D}_n'$ are constructed by a convolution similar to that in equation (29).

The physical interpretation equation (42) is shown in Figure 51. From these events, it is impossible to predict primaries *or* the receiver ghost of primaries. Thus, making it possible to preserve both primaries and receiver ghosts of primaries.

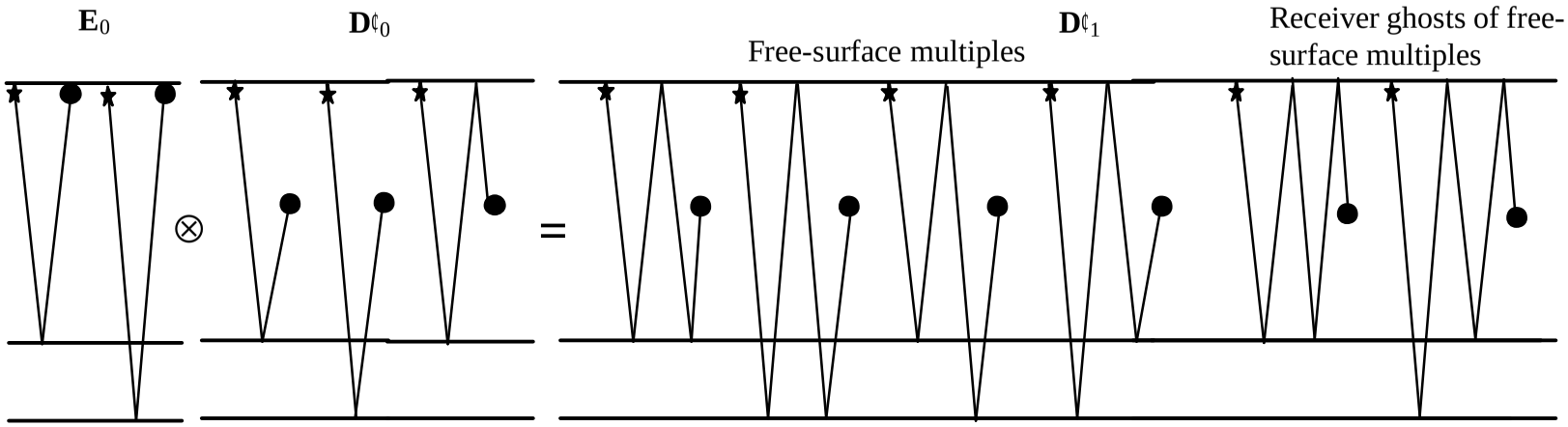

Figure 51. Physical interpretation of the construction of the $\mathbf{D}\mathbb{C}_1$ term using vertical cable data without the direct arrival, $\mathbf{D}\mathbb{C}_0$, and streamer data, $\mathbf{E}_0$, as a complimentary wavefield. Here, we see the construction of the first-order free-surface multiples and receiver ghosts of multiples. Primaries and receiver ghosts of primaries are not generated. Compare with Figure 50. The streamer data provides the missing raypaths needed to construct the events in $\mathbf{D}\mathbb{C}_1$. The ⊗ denotes convolution.

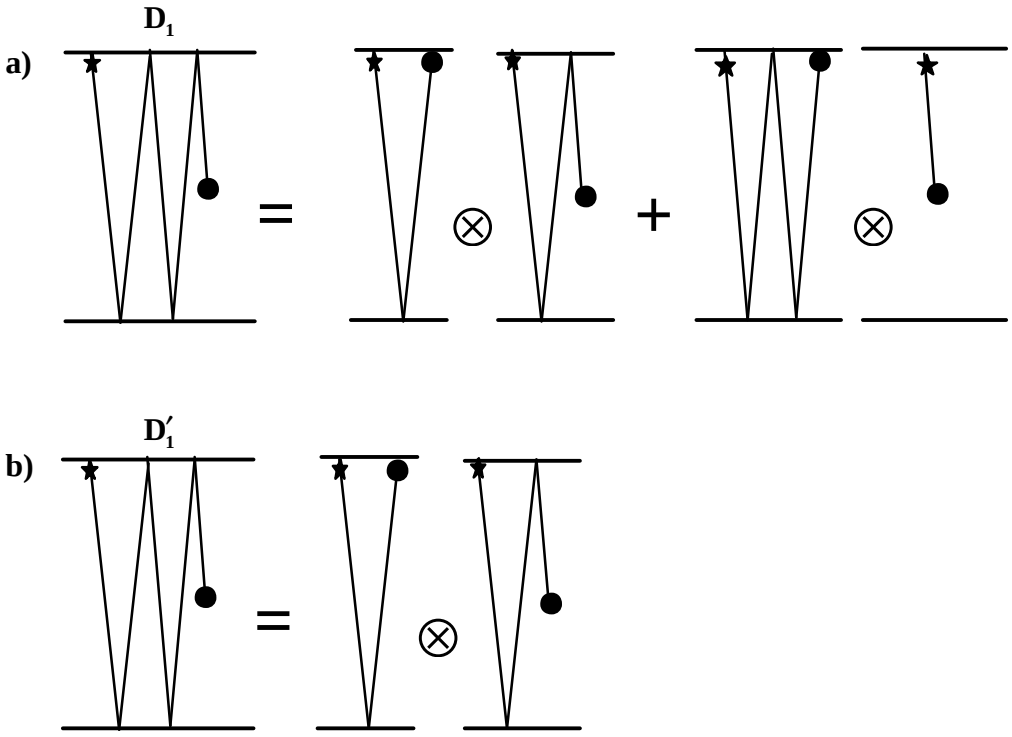

Figure 52. The receiver ghost in wavefield $\mathbf{D_1}$ is constructed by the combination of primaries, receiver ghosts, free-surface multiples and the direct wave. The receiver ghost in $\mathbf{D_1'}$ is constructed from primaries and receiver ghosts only. Therefore, the scaling factor, **A**, is different for the removal process of these two events.

The inverse source, $\mathbf{A}_G$, in equation (41) is not equal to the inverse source, $\mathbf{A}$, in equation (28). Figure 52 illustrates the components of a particular receiver ghost contained in the recorded wavefield $\mathbf{D}_0$. $\mathbf{D}_1$ is constructed from the vertical cable data containing the direct wave. Therefore, all combinations of primaries, receiver ghosts, free-surface multiples and the direct wave can sum to produce the receiver ghost with the correct amplitudes in the convolutional process. $\mathbf{D}_1'$ is constructed from vertical cable data without the direct wave, $\mathbf{D}_0^{(wd)}$. Hence, the receiver ghosts are built from only primaries and other receiver ghosts and do not include the effects of the direct wave. Therefore, a different source signature will be required to remove the same event from $\mathbf{D}_1$ and $\mathbf{D}_1'$. However, both $\mathbf{D}_1$ and $\mathbf{D}_1'$ can predict free-surface multiples with proper travel times and amplitudes because they are independent of the down-going direct wave and can be removed with the same $\mathbf{A}$. Therefore, the results of the series in equation (41) will preserve primaries and the receiver ghosts of primaries as well as small contributions of receiver ghosts of multiples not predicting in equation (42) while removing free-surface multiples.

Attenuating primaries, free-surface multiples and receiver ghosts of multiples while preserving receiver ghosts of primaries

We now want to remove primaries, free-surface multiples and receiver ghosts of multiples while preserving receiver ghosts of primaries. Using the results described above, this task becomes one of subtracting the results of $\mathbf{D}_P$, the data derived with the

direct wave, from $\mathbf{D}_{PG}$, the data derived without the direct wave. This results in the following equation

$$\mathbf{D_G = D_{PG} - D_P}, \tag{43}$$

where $\mathbf{D}_G$ contains the receiver ghost of primaries. The scaling difficulties related to $\mathbf{D}_{PG}$ discussed above will be carried into equation (43). Thus, we will not entirely remove the receiver ghosts of multiples. Alternately, if we substitute the expressions $\mathbf{D}_{PG}$ for [equation (41)] and $\mathbf{D}_P$ [equation (28)] into equation (43), we arrive at

$$\mathbf{D}_G=\mathbf{A}(\mathbf{D}_1'-\mathbf{D}_1) + \mathbf{A}^2(\mathbf{D}_2'-\mathbf{D}_2) + \mathbf{A}^3(\mathbf{D}_3'-\mathbf{D}_3) + \ldots, \tag{44}$$

or

$$\mathbf{SD}_G = (\mathbf{D}_1'-\mathbf{D}_1) + \mathbf{A}(\mathbf{D}_2'-\mathbf{D}_2) + \mathbf{A}^2(\mathbf{D}_3'-\mathbf{D}_3) + \ldots, \tag{45}$$

where

$$\mathbf{S}=\frac{\mathbf{1}}{\mathbf{A}}. \tag{46}$$

This new series for attenuating primaries, free-surface multiples and receiver ghosts of multiples while preserving the receiver ghosts of primaries does not depend explicitly on $\mathbf{D}_0$. Therefore, we can overcome the scaling problems associated with $\mathbf{D}_{PG}$.

The physical interpretation of equation (45) is quite simple. The $\mathbf{D}_1$ term corresponds to the wavefield containing first-order free-surface multiples and the receiver ghosts of first-order multiples, as well as the receiver ghosts of primaries. The $\mathbf{D}_1'$ term corresponds to the wavefield containing first-order free-surface multiples and the receiver ghosts of first-order multiples, but not the receiver ghosts of primaries. Therefore, the difference between the $\mathbf{D}_1$ and $\mathbf{D}_1'$ is the ghosts of primaries. This process

is the same for higher-order terms. Again, ($\mathbf{D}_1'$-$\mathbf{D}_1$) contains residual amplitudes from the receiver ghosts of multiples from the computation of $\mathbf{D}_1'$, as discussed previously. Including higher-order terms in equation (44) or (45) corrects these errors and, we arrive at the solution we desired, namely, preserving only the receiver ghosts of primaries.

NUMERICAL SYNTHETIC EXAMPLES

Here we present 2D numerical examples to illustrate the applicability of ISMA as seen in equation (28) for preserving primaries while attenuating free-surface multiples, receiver ghost of multiples and receiver ghosts of primaries, equation (41) for preserving primaries and receiver ghosts of primaries while attenuating free-surface multiples and receiver ghosts of multiples and equation (45) for preserving receiver ghosts of primaries while attenuating primaries, free-surface multiples and receiver ghosts of multiples.

We use an elastic, faulted-earth model described in Figure 53. It shows a homogeneous water layer over an inhomogeneous solid consisting of three homogeneous media. Four vertical cables are deployed within the model with receivers densely spaced along each cable. A surface streamer consisting of 135 hydrophones is also active for each source position. We simulate 135 sources with each source position coinciding with a streamer receiver position, corresponding to offsets ranging between 0 and 1876 m. We use the fully elastic finite-difference method discussed in Chapter II to generate the vertical cable and streamer data simultaneously.

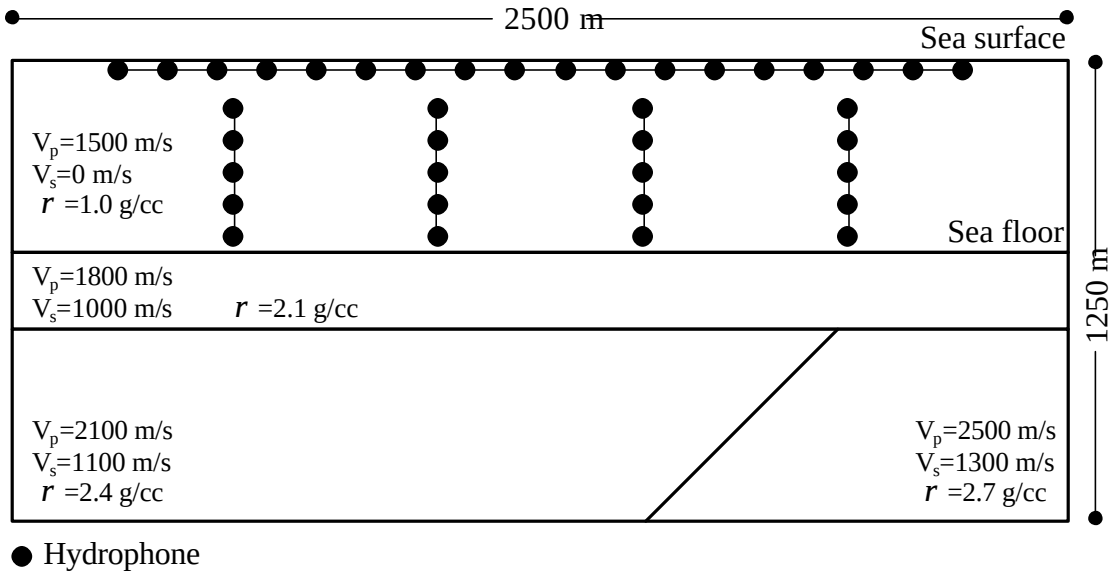

Figure 53. Model used to generate streamer data and vertical cable data.

Predicting and removing free-surface multiples, receiver ghosts of multiples and receiver ghosts of primaries while preserving primaries

Figure 54 shows a common shot gather and a common receiver gather for the vertical cable data, $\mathbf{D}_0$. The seismogram contains primaries, receiver ghosts of primaries, free-surface multiples, receiver ghosts of free-surface multiples and the direct wave. The goal here is to preserve the primaries while attenuating the free-surface multiples, receiver ghosts of multiples and receiver ghosts of primaries. Figure 55 shows the term $\mathbf{D}_1$ from equation (29) consisting of the predicted first-order free-surface multiples, receiver ghosts of multiples and receiver ghosts of primaries. The first-order free-surface multiples have correct travel times and amplitudes while the higher-order multiples have the correct travel times, but incorrect amplitudes. This is corrected by using the higher-order terms of the series in equation (29). Figure 56 shows the term $\mathbf{D}_2$, from equation (29), consisting of the predicted second-order free-surface multiples, receiver ghosts of multiples and receiver ghosts of primaries. Only two terms of equation (29) are used in accordance with the data length. Figure 57 shows the resulting wavefield $\mathbf{D}_P$, containing primaries only, as constructed in equation (28). Although the exact source signature, $A(w)$**,** was known, it was not used because the finite-difference modeling generates events such as source ghosts, the actual source and the apparent source are not identical. This makes these data examples more like the real data sets.

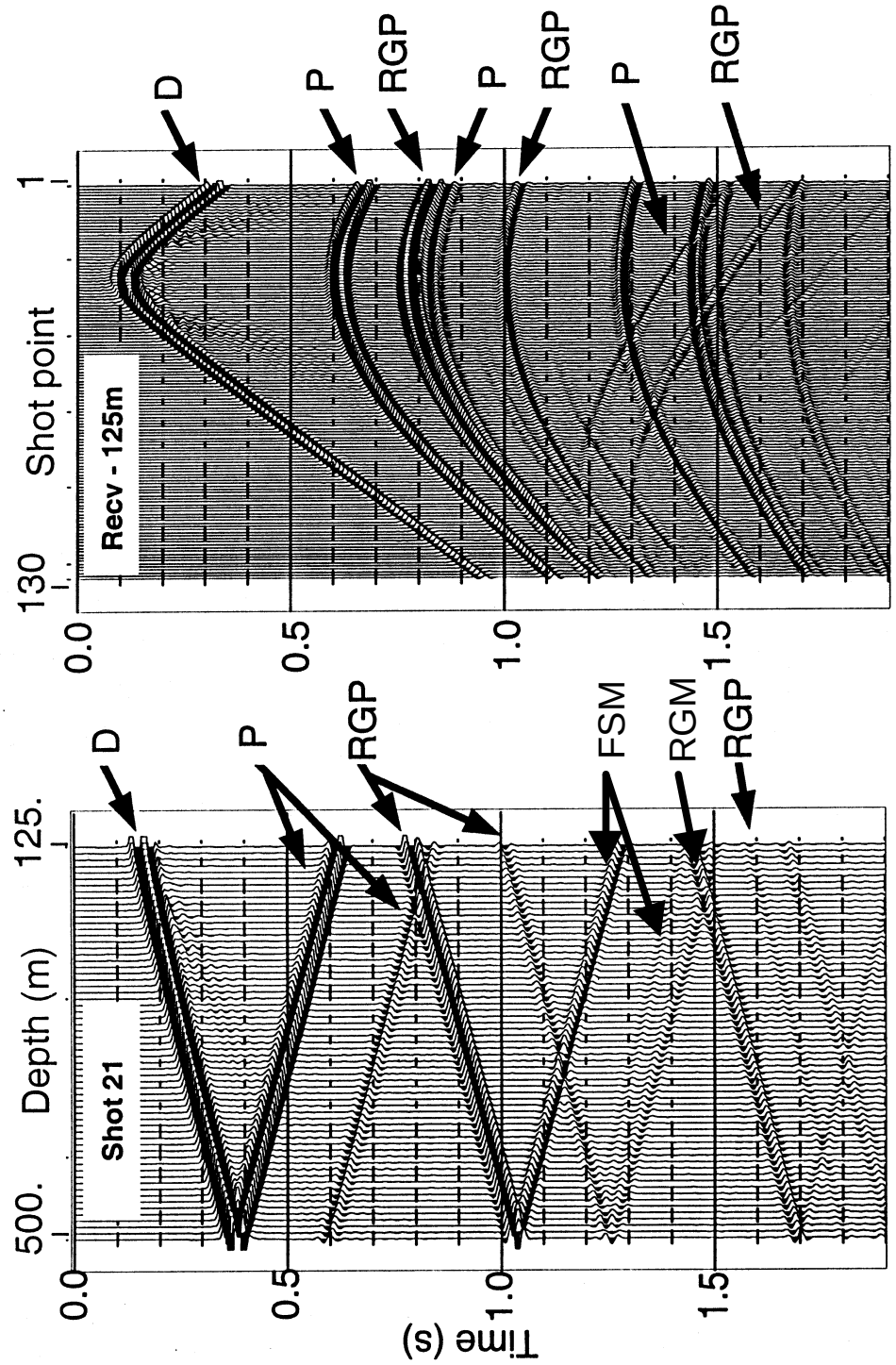

Figure 54. Common shot gather and common receiver gather corresponding to the 2-D model in Figure 53. The seismograms contain the direct wave (D), primaries (P), free-surface multiples (FSM), receiver ghosts of primaries (RGP) and receiver ghosts of multiples (RGM).

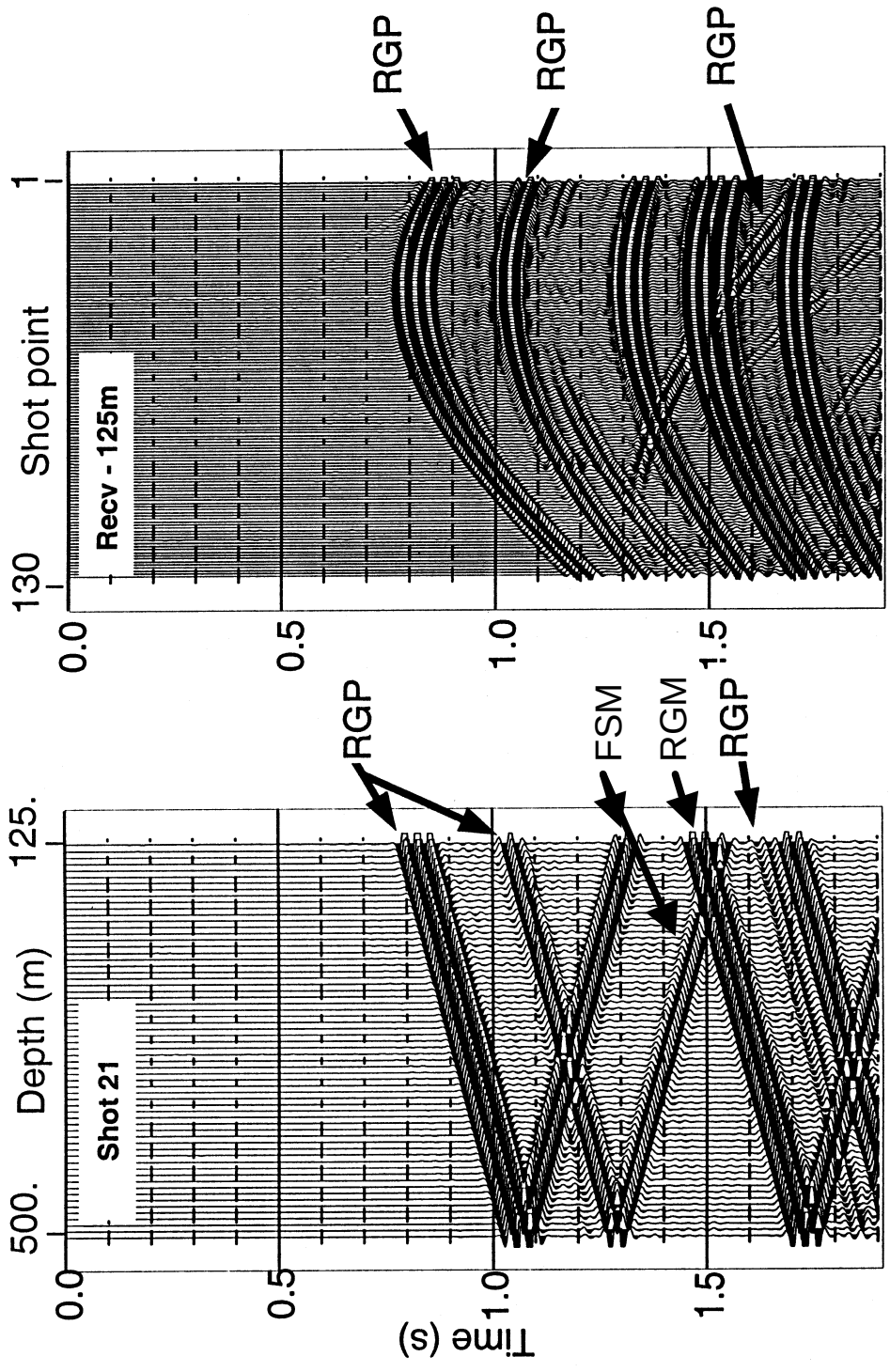

Figure 55. Predicted first-order free-surface multiples and receiver ghosts of primaries and multiples corresponding to the $\mathbf{D}_1$ term in equation (29).

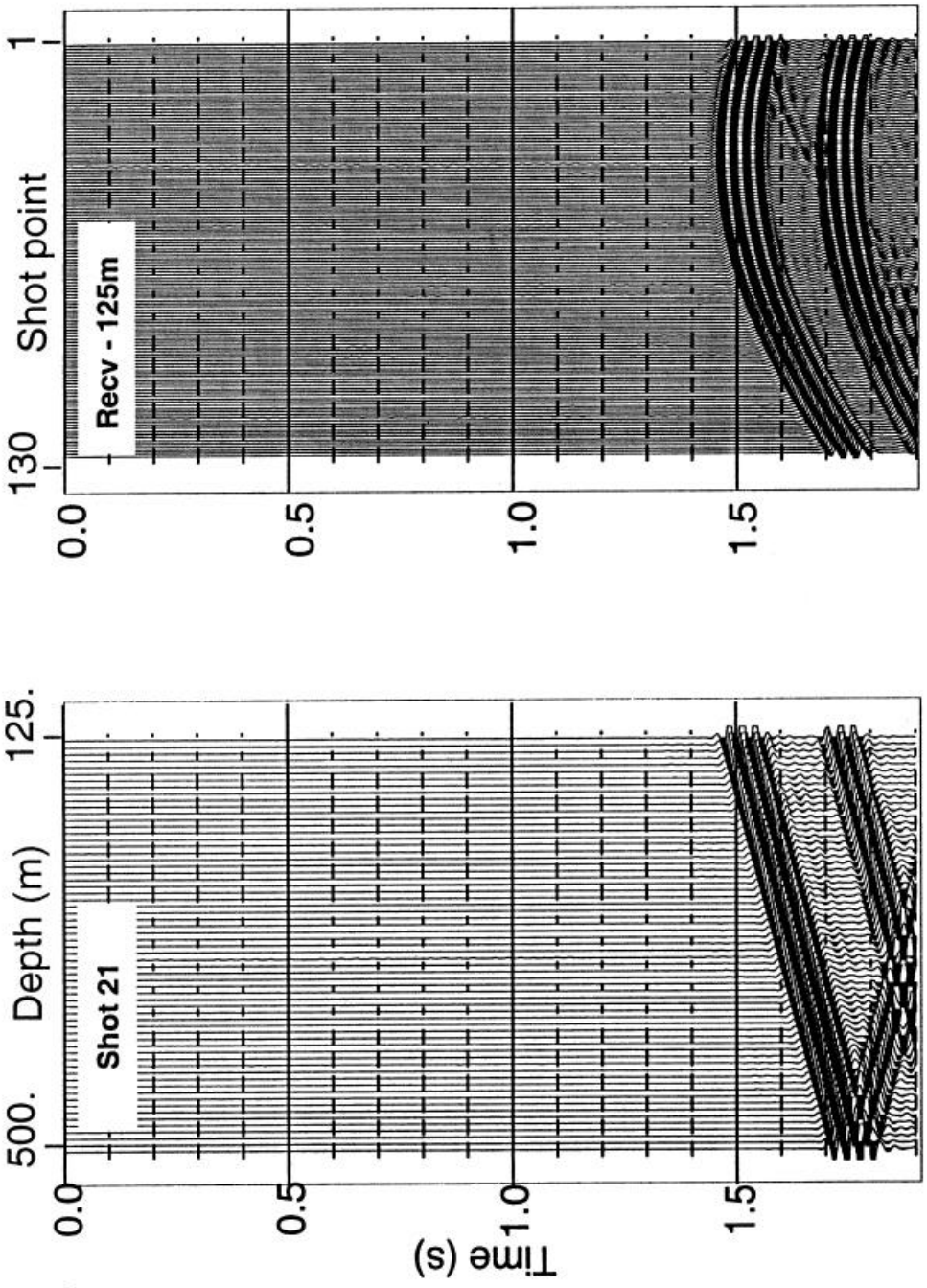

Figure 56. Predicted second-order free-surface multiples and receiver ghosts of primaries and multiples corresponding to the $\mathbf{D}_2$ term in equation (29).

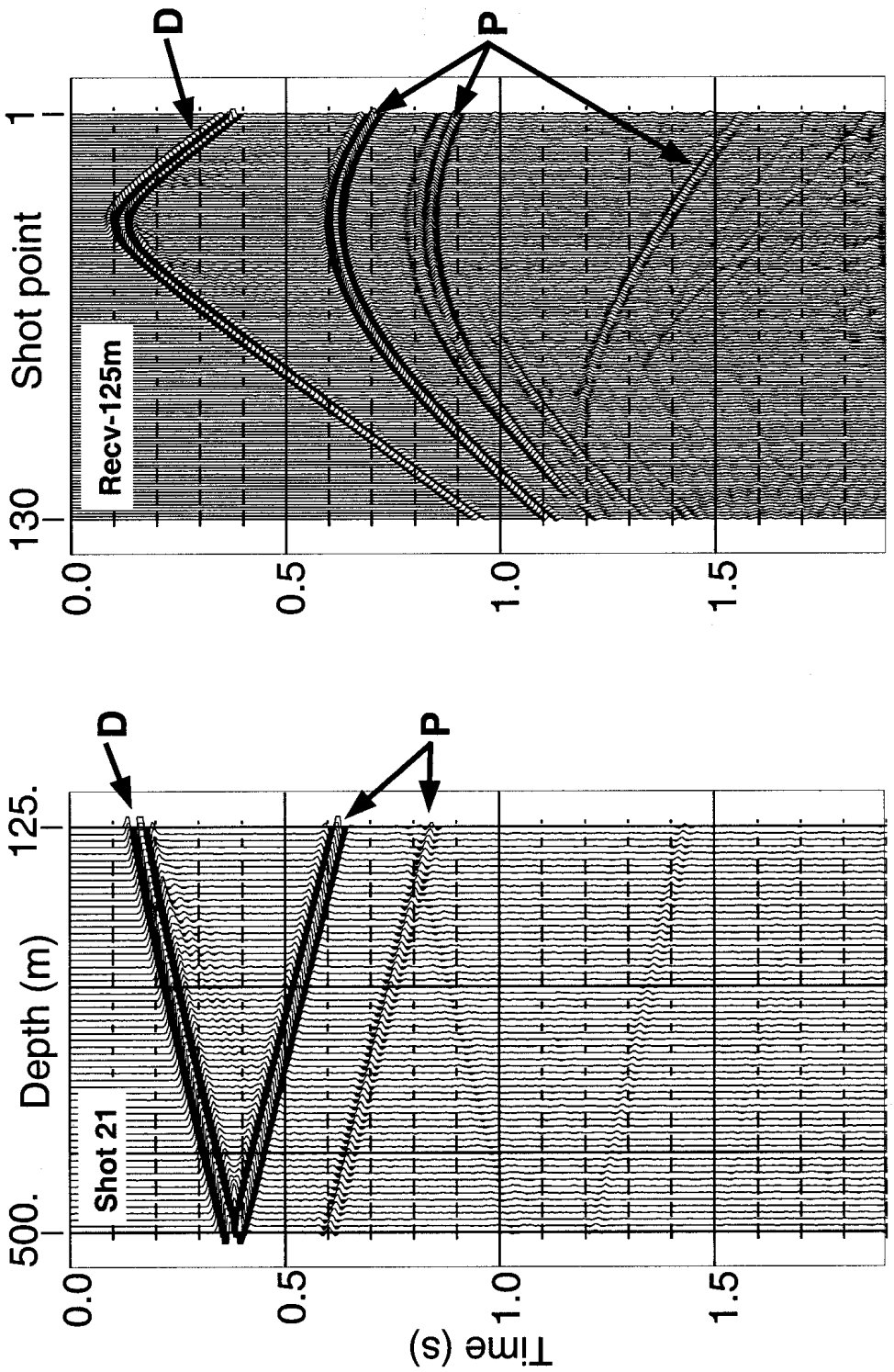

Figure 57. Result of attenuating free-surface multiples, receiver ghosts of primaries and receiver ghosts of multiples using the solution in equation (28).

Predicting and removing free-surface multiples and receiver ghosts of multiples while preserving primaries and receiver ghosts of primaries

The task now is to preserve the primaries and receiver ghosts of primaries while attenuating free-surface multiples and receiver ghosts of multiples. To do this, we will use the vertical cable data without the direct arrivals and the series in equation (41). Figure 58 shows the same common shot gather and common receiver gather for vertical cable data without the direct wave. Figure 59 shows the application of equation (42) in predicting $\mathbf{D}_1'$ containing first-order free-surface multiples and receiver ghosts of multiples. Again, this is accomplished by combining the streamer data with the vertical cable data without the direct wave. The free-surface multiples and receiver ghosts of free-surface multiples are predicted with correct travel times, but incorrect amplitudes. Again, this is due to the removal of the direct wave, effectively eliminating the raypath necessary to construct all ghosts of free-surface multiples, see Figure 52. Figure 60 illustrates the $\mathbf{D}_2'$ term containing the predicted second-order free-surface multiples and receiver ghosts of multiples using equation (42). Only two terms are computed in accordance with data length. Figure 61 shows the resulting wavefield, $\mathbf{D}_{\mathrm{PG}}$, as provided by the solution in equation (41). Again, although the exact source signature, $A(w)$, was known, it was not used in the application of equation (41).

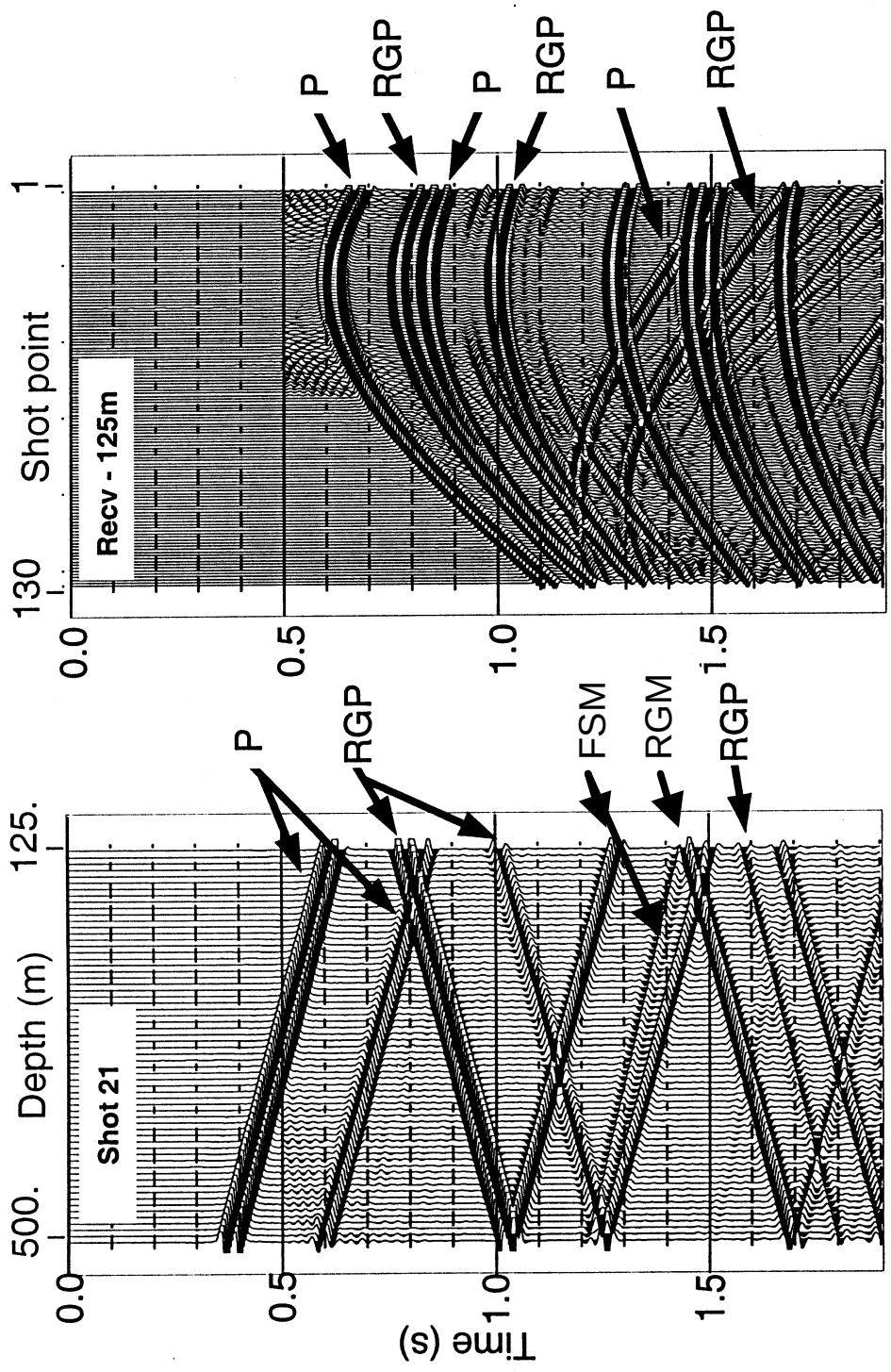

Figure 58. Common shot gather and common receiver gather without the direct wave arrivals corresponding to the 2-D model in Figure 53. The seismograms contain primaries, free-surface multiples, receiver ghosts of primaries and receiver ghosts of multiples.

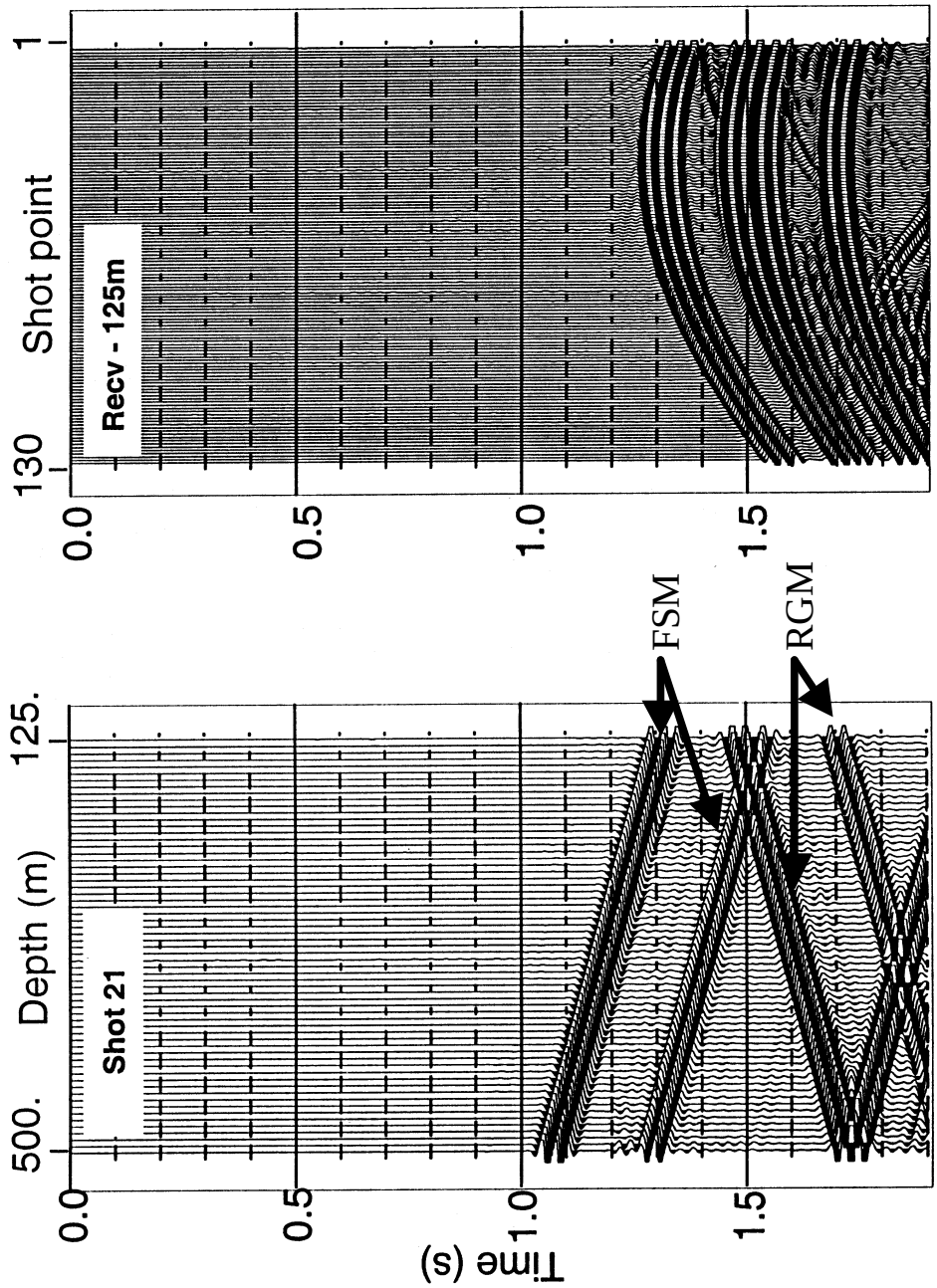

Figure 59. Predicted first-order free-surface multiples and receiver ghosts of multiples corresponding to the term $\mathbf{D}_1'$ in equation (42) and the vertical cable data without the direct wave arrivals.

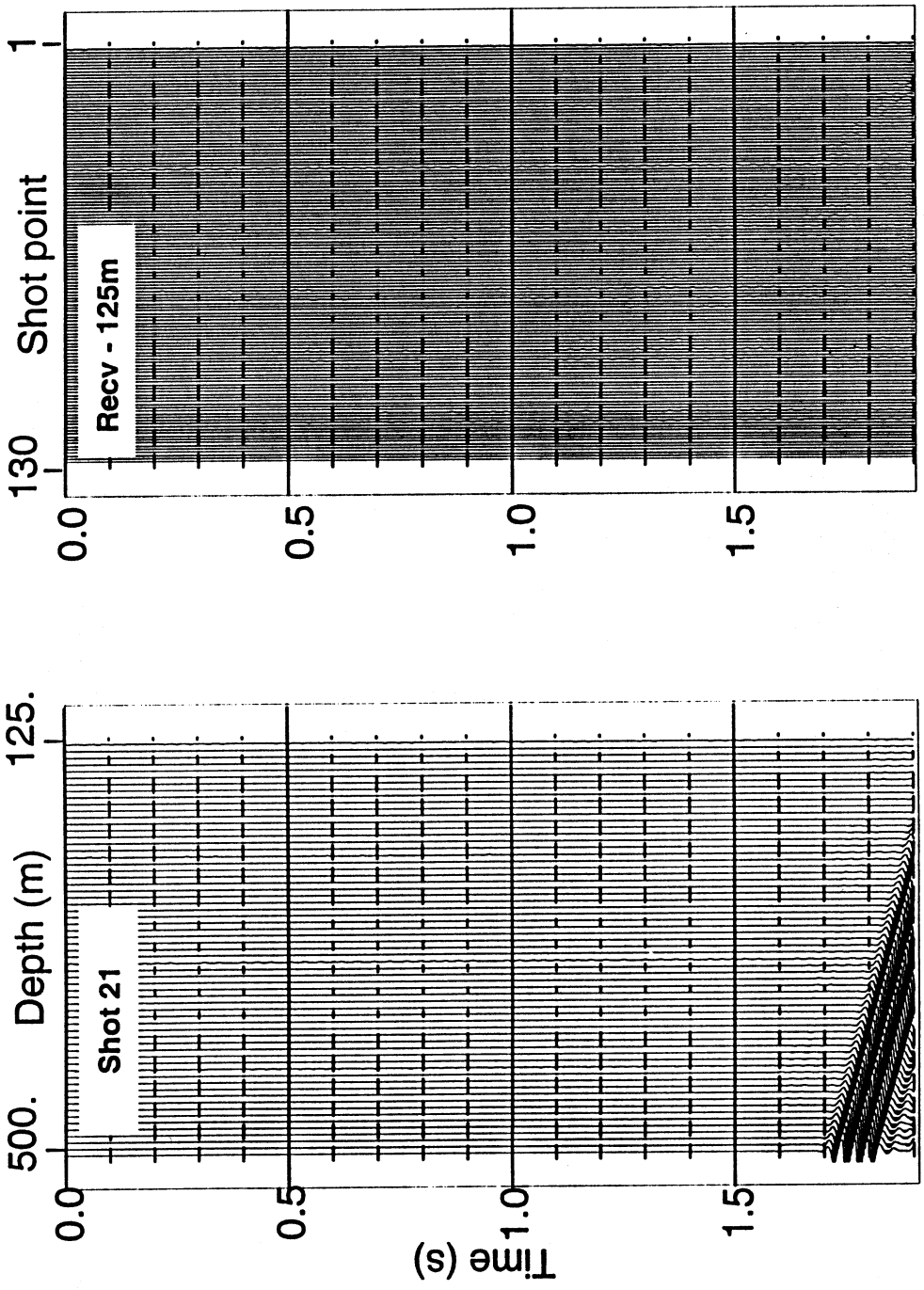

Figure 60. Predicted second-order free-surface multiples and receiver ghosts of multiples corresponding to the $\mathbf{D}_2'$ term in equation (42) and the vertical cable data without the direct wave arrivals.

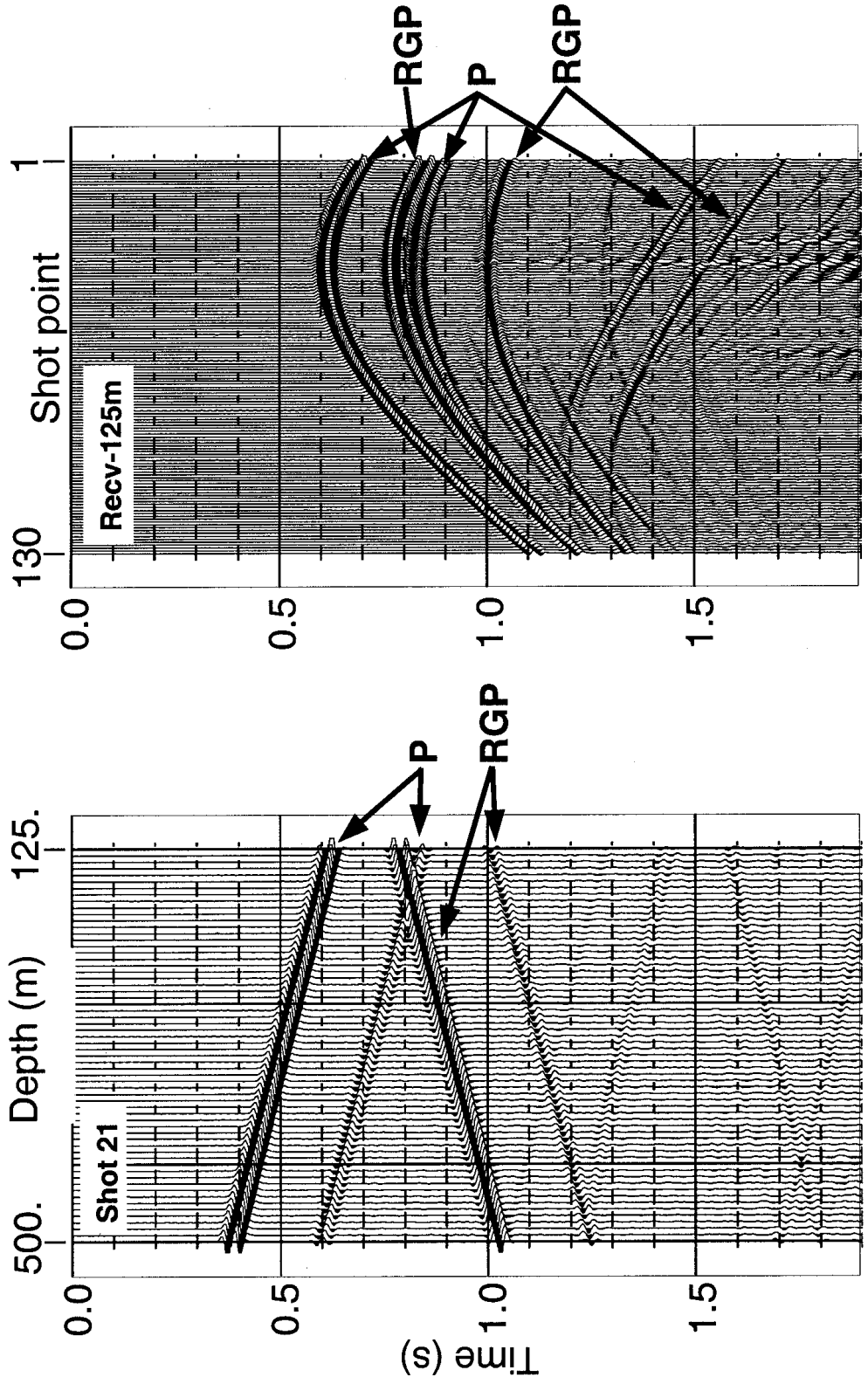

Figure 61. Result of attenuating free-surface multiples and receiver ghosts of multiples using the solution in equation (41).

Preserving receiver ghosts of primaries while attenuation primaries, free-surface multiples and receiver ghosts of multiples.

We would now like to remove primaries, free-surface multiples and receiver ghosts of multiples while preserving only the receiver ghosts of primaries. Equation (43) requires the direct subtraction of $\mathbf{D}_P$, which contains only primaries, from $\mathbf{D}_{PG}$, which contain primaries and receiver ghosts of primaries, shown in Figures 57 and 61, respectively. Unfortunately, this result contains the residual amplitudes of some receiver ghosts associated with the estimation of $\mathbf{A}_G$ as discussed previously and illustrated in Figure 52.

A better solution to preserving only receiver ghosts of primaries can be accomplished using equation (44) or (45). Equation (45) requires the difference of the predicted wavefields using the original vertical cable data and the vertical cable data without the direct wave. These wavefields, $\mathbf{D}_1$, $\mathbf{D}_2$, $\mathbf{D}_1'$ and $\mathbf{D}_2'$, are shown in Figures 55, 56, 59 and 60, respectively. Thus, following equation (45), wavefield ($\mathbf{D}_1'$-$\mathbf{D}_1$) is calculated and shown in Figure 62 and wavefield ($\mathbf{D}_2'$-$\mathbf{D}_2$) is calculated and shown in Figure 63. Notice the ($\mathbf{D}_1'$-$\mathbf{D}_1$) and ($\mathbf{D}_2'$-$\mathbf{D}_2$) wavefield contain only down-going events, i.e., receiver ghosts of primaries and receiver ghosts of multiples, confirming the earlier statement that the free-surface multiples had the same amplitudes. Application of the full series in equation (45) provides us with the result we are after, namely, preserving only receiver ghosts of primaries as seen in Figure 64.

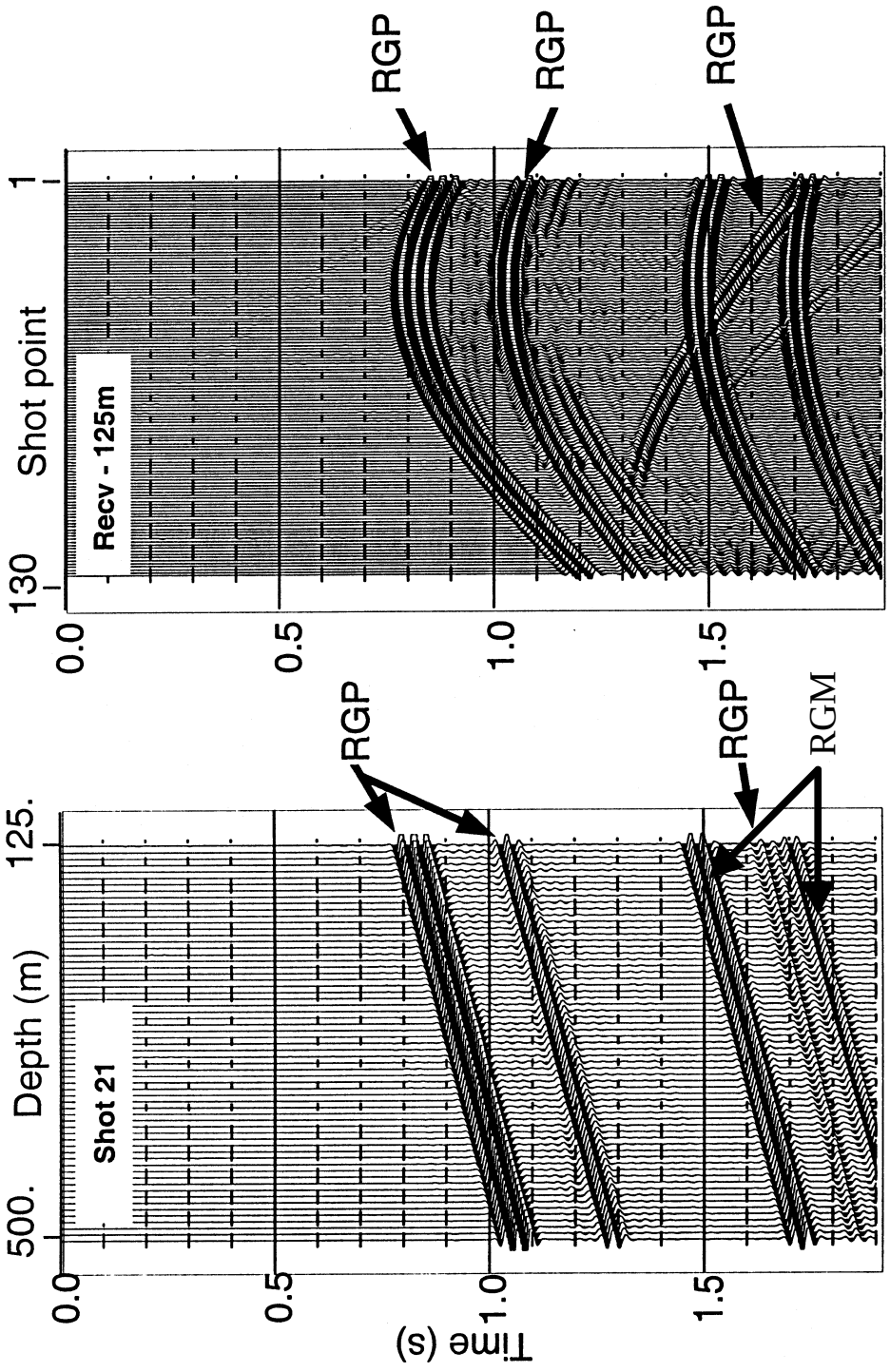

Figure 62. Difference between the predicted first-order term using the vertical cable data with the direct wave arrivals and the predicted first-order term using the vertical cable data with the direct wave arrivals.

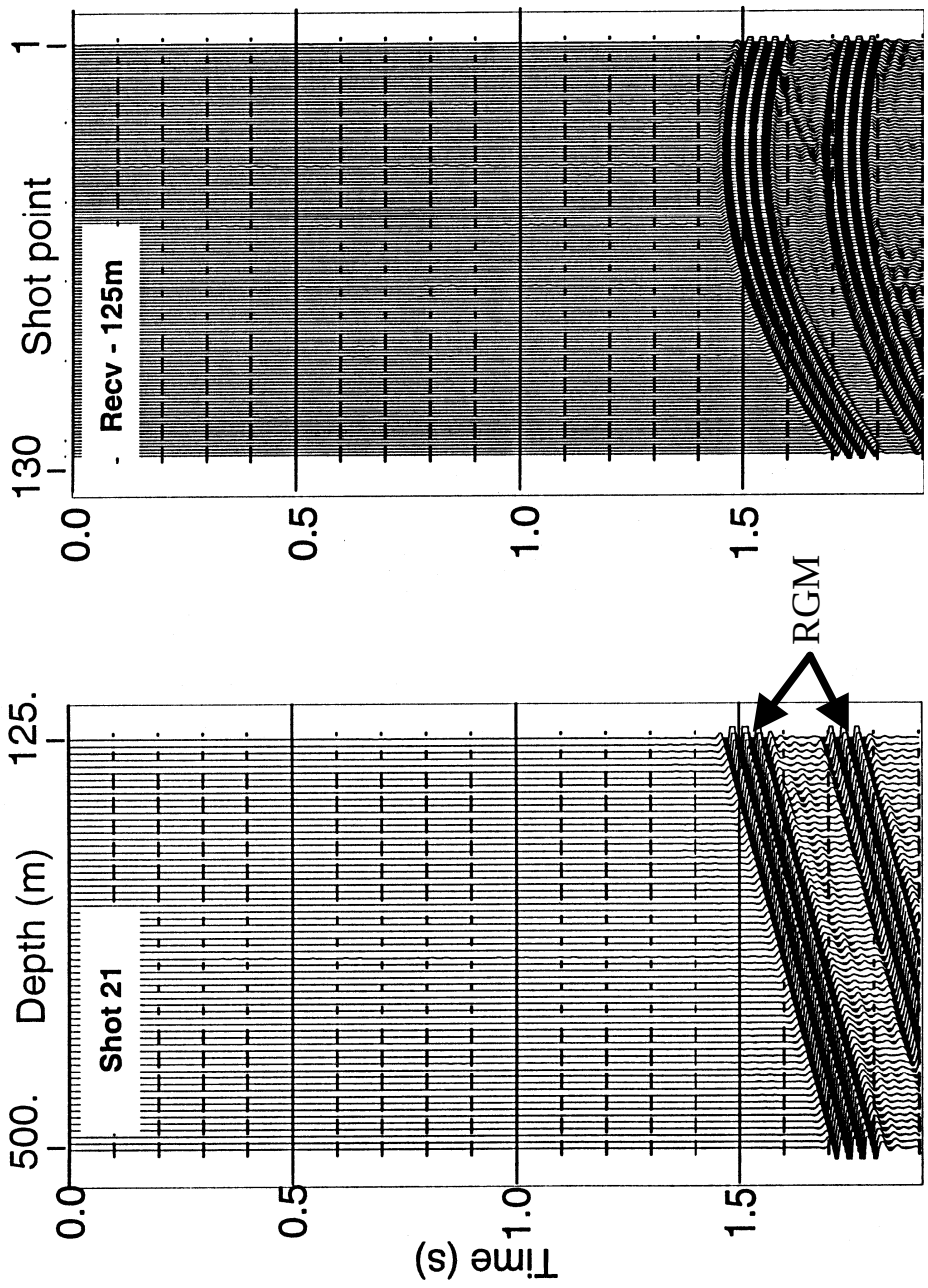

Figure 63. Difference between the predicted second-order term using the vertical cable data with the direct wave arrivals and the predicted second-order term using the vertical cable data with the direct wave arrivals.

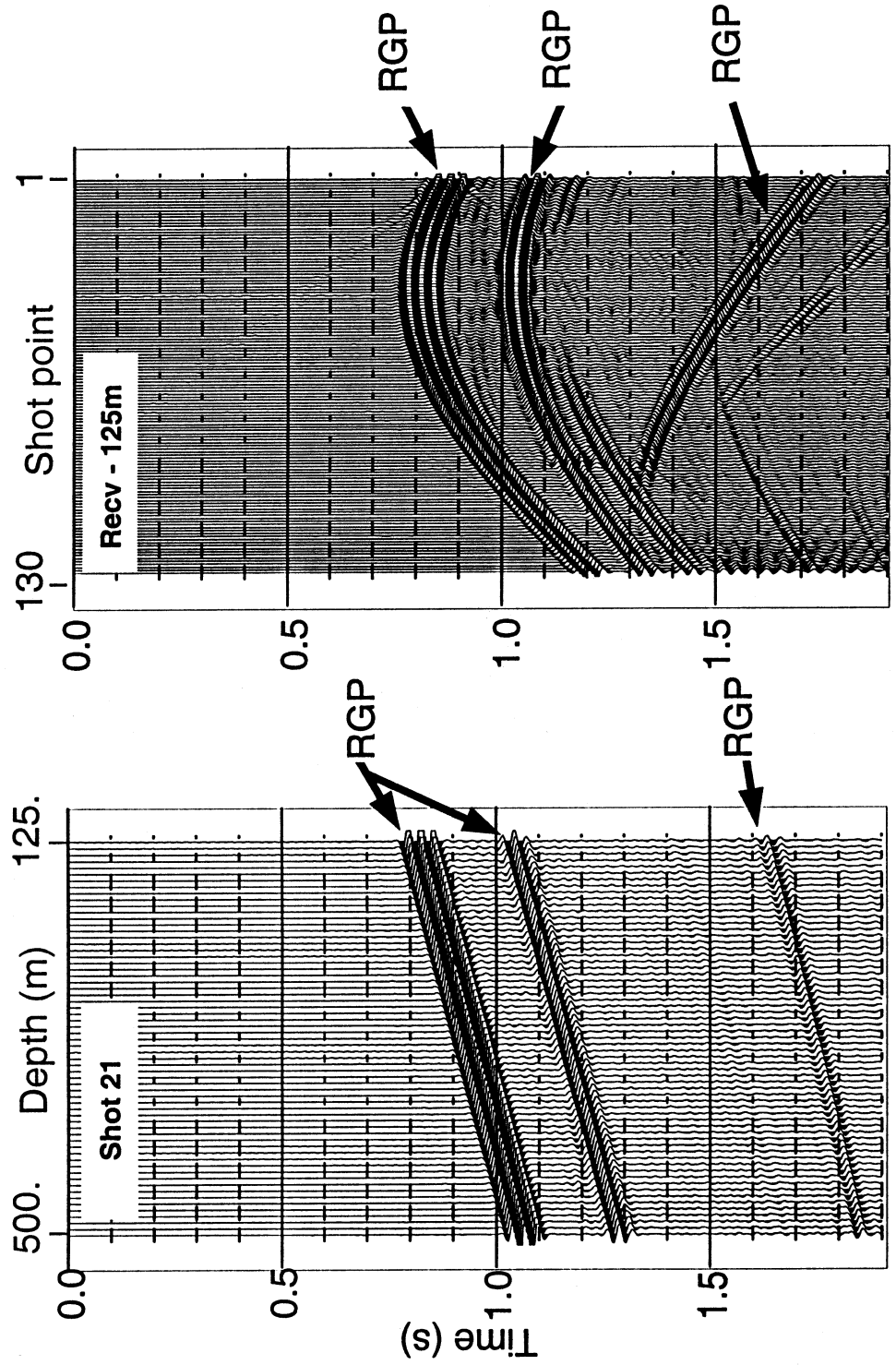

Figure 64. Results of attenuating primaries, free-surface multiples and receiver ghosts of multiples using the solution in equation (45).

CONCLUSIONS

Vertical cable data contains primaries and receiver ghosts of primaries that require special treatment for either preservation or attenuation in the processing flow. The method for preserving either primaries or the receiver ghosts of primaries based on the inverse scattering series proposed by Ikelle (2001) provides solution for either case. The traditional application of ISMA to vertical cable data preserves the primaries while attenuating the free-surface multiples, the receiver ghosts of multiples and the receiver ghosts of primaries. By removing the direct wave of the vertical cable data, we can now attenuate the primaries, free-surface multiples and the receiver ghosts of multiples while preserving the receiver ghosts of primaries. This method does not require any knowledge of the subsurface.

CHAPTER V

LAND VERTICAL CABLE SEISMIC

INTRODUCTION

Here, we propose extending vertical cable surveying to the land environment. This chapter appears as published in The Leading Edge (1999)*.

Traditionally, the quality of land seismic data has been poor due to the energy trapped in the low velocity layers in the shallow subsurface. These low-velocity zones generate ground roll and statics that interfere with primary reflection data. Also, undersampling, poor coupling and imprecise orientation of multi-component geophones result in low signal to noise ratio. In this paper we demonstrate how vertical cable (VC) technology can overcome these problems.

Vertical cable technology has been applied in marine surveys with encouraging results (e.g. Guimaraes, et al., 1998: Krail, 1994), and we feel that adapting it to onshore exploration could significantly improve data quality.

Land VC surveys can be described as multi-survey, multi-offset walkaway vertical seismic profiling (VSP) (Figure 65). Vertical receiver arrays are positioned in boreholes at specified intervals, just as in a VSP. Multi-component geophones are coupled to the borehole wall and shooting occurs at the surface. VSP target near-hole

---

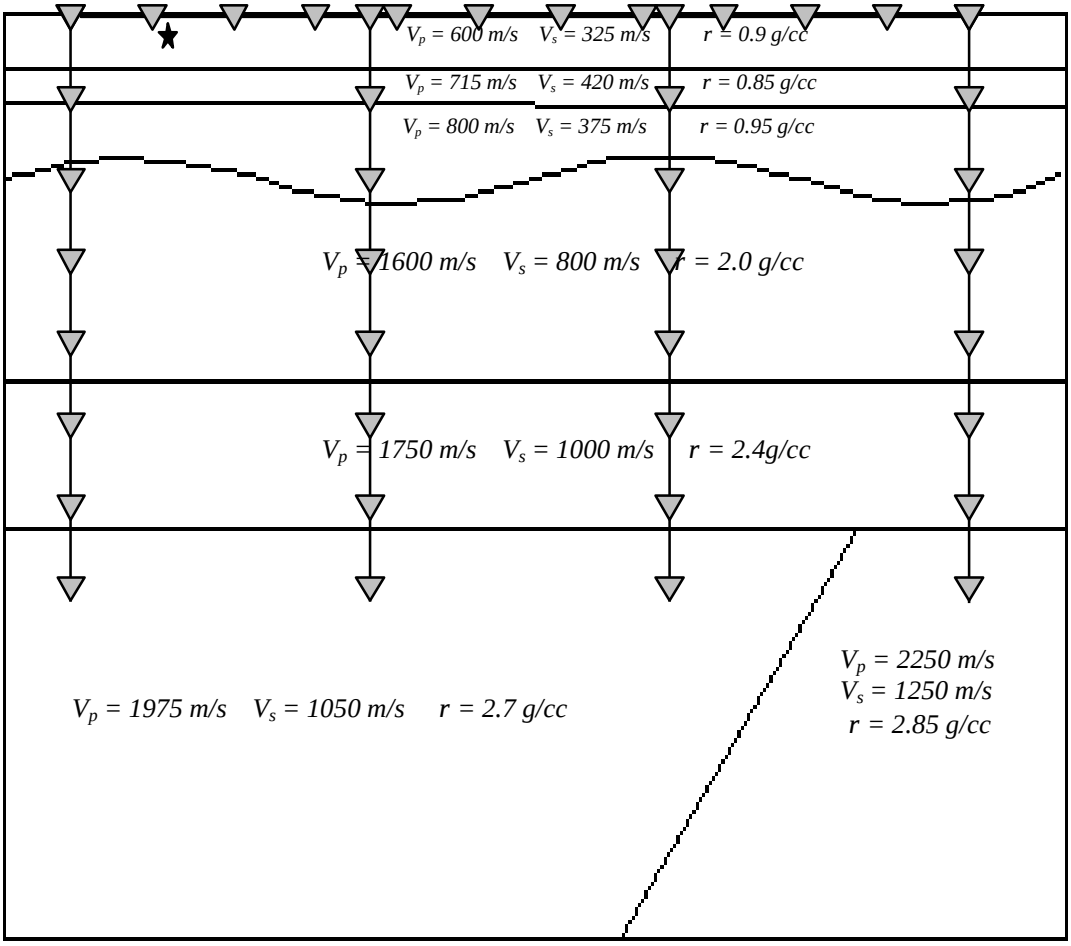

Figure 65. Earth model showing onshore vertical cables and surface receiver array.

reflectors, but VC's aim is to image the entire subsurface a la a traditional surface seismic survey. Another difference is that VSP experiments take place in production boreholes, but VC surveys occur in less costly and shallower sub-production boreholes.

As stated earlier, VC surveys can theoretically overcome many processing problems associated with land surface seismic, but, in order to achieve these goals, we must properly sample the wavefield. This will require a minimum sampling interval in cable spacing and receiver spacing along the cable that can equal that of surface surveys

VC LAND DATA

Using a faulted earth model with undulating low-velocity layers, we generated synthetic data using full elastic finite-difference modeling. This allows us to model primaries, multiples and converted waves at any point within the model. Surface data and VC data were recorded simultaneously for each shot. Figure 66 is a plot of the vertical particle displacement for a common-shot record for an explosive source 10 m below the earth surface and in the low-velocity zone.

The first panel corresponds to the surface data; each successive panel corresponds to a separate vertical cable array. The near-surface, low-velocity zones produce ground roll that propagates with a low velocity. It appears on the seismogram as low-frequency, high-amplitude, dispersive noise. The undulating low-velocity zone can deform the data similar to statics.

The surface data in Figure 66 are an example of poor quality often obtained with traditional surface methods. Ground roll is severely corrupting primary arrivals. Attempts to remove this ground roll using a f-k filter were unsuccessful. Adaptive noise suppression and polarization filters also failed to remove ground roll properly (Shieh and Herrmann, 1990; Samson and Olson, 1981).

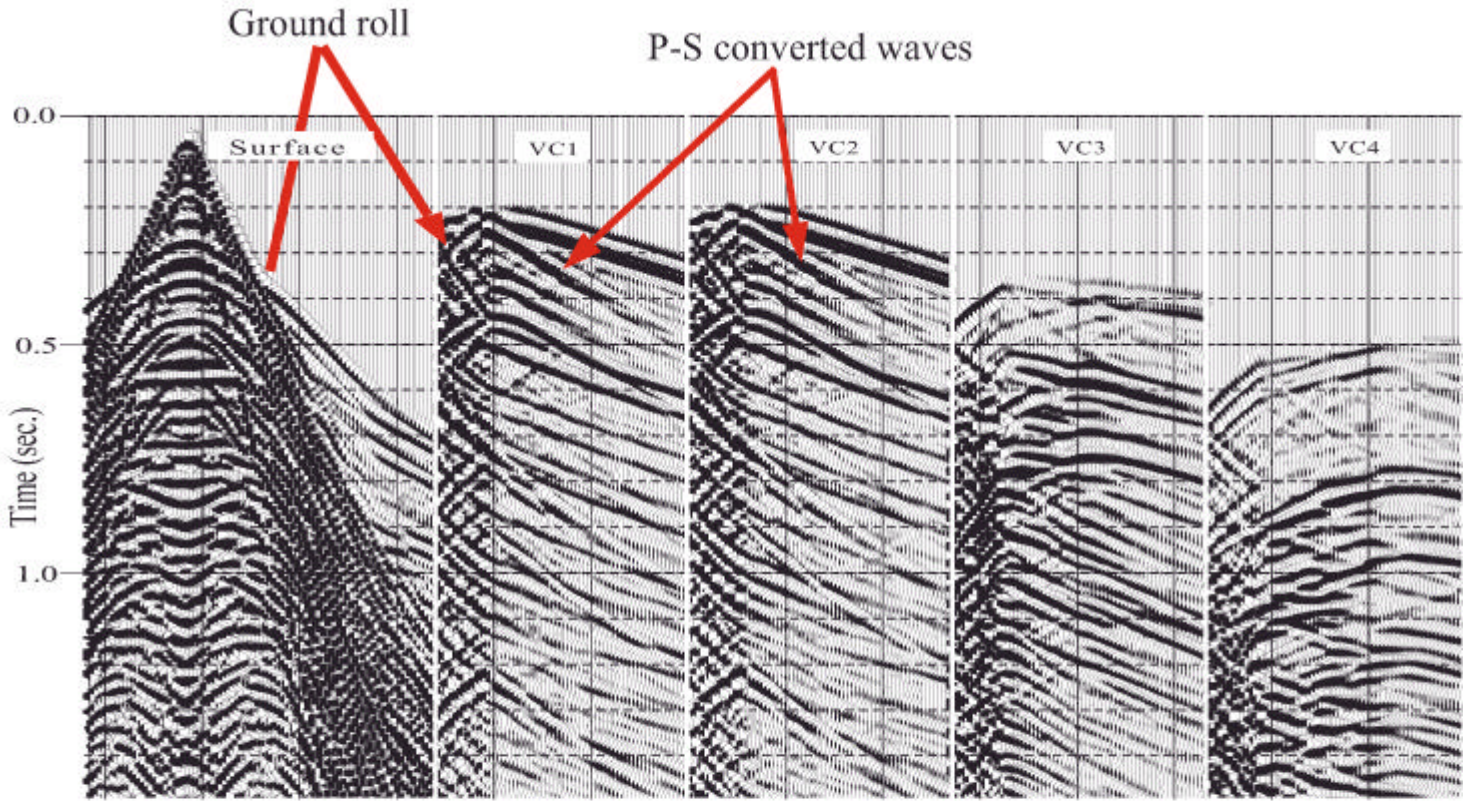

Figure 66. Synthetic common-shot gather (vertical component of the particle velocity) for surface receiver array and vertical cables as seen in Figure 65. Source was in the low-velocity zone. The ground roll in the surface data is disrupting the primary events, while the ground roll in the vertical cable data is limited to shallow receivers in the low-velocity layers.

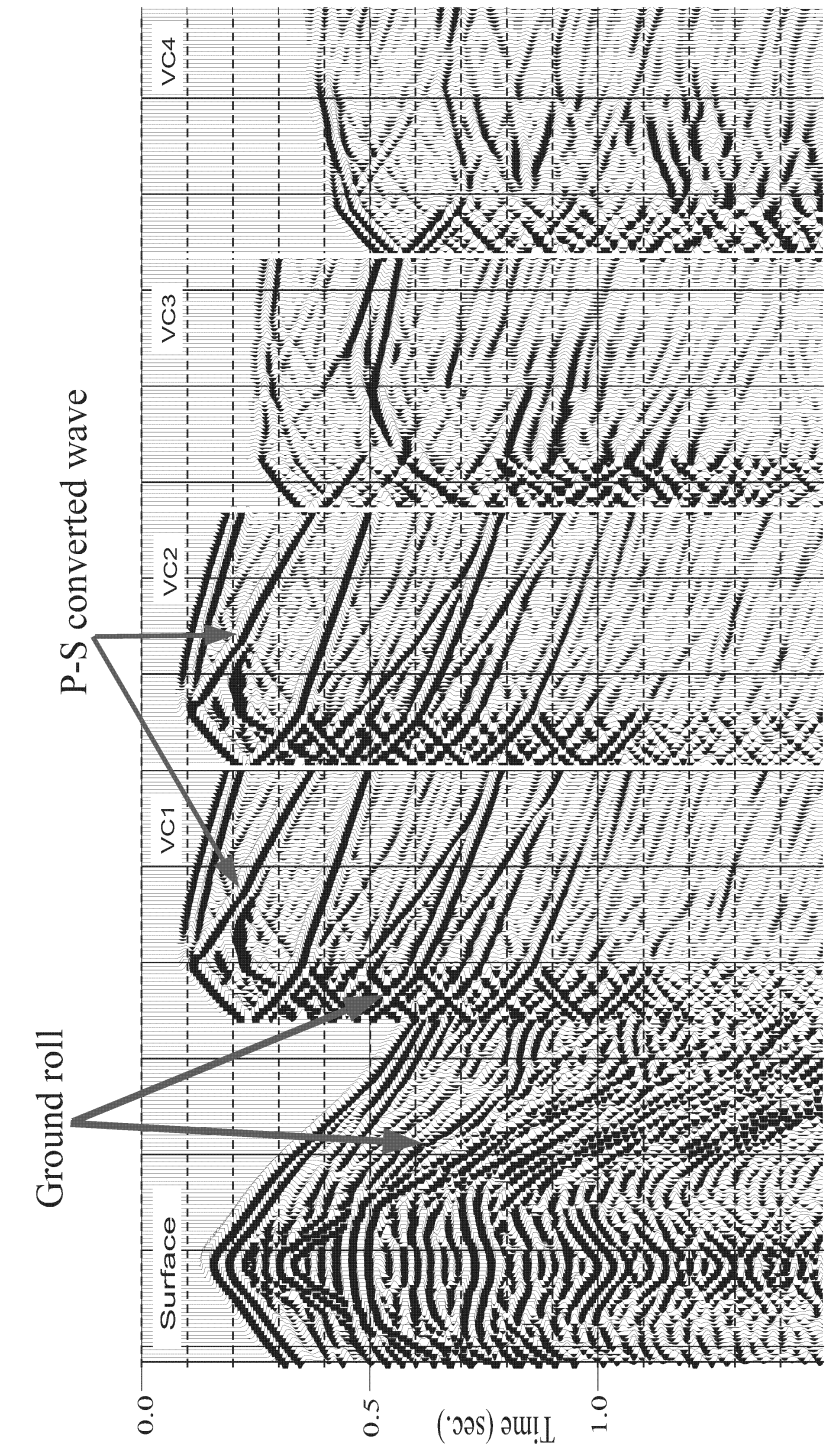

Figure 67. Synthetic common-shot gather (vertical component of the particle velocity) for surface receiver array and vertical cables as seen in Figure 65. Source was below the low-velocity zone. VC data quality is improved and lacks "ringiness".

velocity layers at the same offset. Even though the source is now beneath the low

Figure 67 shows a common shot-gather for a source located below the low velocity layers at the same offset. Even though the source is now beneath the low velocity zone, the surface data still contain significant ground roll. This illustrates why surface data quality is inherently poor. The receivers are always influenced by the shallow subsurface heterogeneities.

VC acquisition overcomes many problems associated wit surface seismic. The very nature of land seismic implies the ability to use a three-component source and record multi-component data. By coupling the cable onto the walls of fluid-filled boreholes, we gain the opportunity to record four-component data versus three-component surface data (in other words, VC can be characterized as a 12-component survey versus current 9-component surface surveys). The added pressure data can aid in the up/down separation. Also, the orientation and coupling of each receiver is guaranteed when positioned on a fixed vertical cable.

The VC data in Figure 66 have more or less the same appearance as VSP data. There are strong down-going events and weaker up-going events. Also, the P-S converted waves are more important on the VC data due to the larger incidence angles than those achieved in the surface seismic. But more importantly, data quality is significantly better than that of the surface data.

High-amplitude ground roll is limited to receivers in the low-velocity zone. The high amplitudes can be attributed to the large impedance contrasts at the surface and base of the low-velocity zone which effectively traps much of the seismic energy.

Ground roll is eliminated by simply removing the receivers from the low velocity layers. Receivers below the low-velocity zone display data quality similar to that in typical marine-streamer surveys. The simulated static effects due to the irregular base of weathering are still present but are not as significant compared to the equivalent surface data.

Figure 67 shows that further improvements result from placing the source below the low velocity zone. Again, we notice the ground roll is only present in receivers in the low-velocity zone. Many multiples in the VC data are now much weaker than in the prior data set. When the source is beneath the low-velocity zone, the base of weathering acts more or less as a free surface with a reflection coefficient of ~-0.6, which reflects the majority of the up-going energy back down.

VC RESOLUTION VERSUS SURFACE RESOLUTION

To fully analyze the applicability of VC, we must discuss the fundamental problem of spacing between cables and sampling within the cable. We pose the problem of vertical cable sampling as that of finding the spacing between cables which allows us to image at least as well as surface surveys. Due to the difference of data quality between surface and VC data caused by the low-velocity zone, our imaging resolution analysis uses an earth model that does not contain a low-velocity zone.

The two factors controlling the imaging resolution are the total angular coverage and the density of sampling within this angular coverage. Let us first define these two characteristics as they pertain to both surface and vertical seismic surveys. Figure 68

illustrates how we define angular coverage for both the surface and vertical cable survey. $q^{\mathrm{S}}_{\max}$ is the maximum angle of reflection for the surface array. $q^{V}_{\max}$ is the maximum angle of reflection for the vertical cables. To achieve equal or superior resolution using vertical cables, $\Delta q = q^{V}_{\max} - q^{S}_{\max}$ must be greater than zero. In addition, the ray coverage between (0, $q^{V}_{\max}$) must be sampled as densely or greater as the equivalent surface seismic in this interval. For a given image point of depth *Z* and cable length *h*, we can calculate the increased angular coverage VC can achieve by

$$\tan(\Delta q) = \frac{hX}{Z^2 + X^2 - Zh} \ . \qquad (47)$$

So for a given $q^{S}_{\max}$ and the corresponding density coverage from the surface data, the problem becomes one of how to properly sample the wavefield using vertical cables to achieve superior coverage for a given Δq . Figure 5 compares the resolution between the surface data and vertical cable data for an image point at a depth of 2000 m. The surface survey consists of 101 shots and 101 receivers, each spaced at a 25 m interval. Receivers are static in this survey. For this surface survey, $q^{S}_{\max}$ is approximately 64° and the angular coverage is represented by the black line. This line was obtained by grouping all angles in the interval (0, $q^{S}_{\max}$) as a function of their occurrences. The angle was sampled every 1°. Each of the following vertical cable surveys assume a maximum borehole depth of 500 m, which at maximum would yield a $\Delta q = 7.8^{\circ}$. To achieve equivalent vertical cable coverage, six cables spaced every 500 m with 17 receivers spaced every 25 m were used (red line, Figure 69). If this sampling is retained within each cable but cable

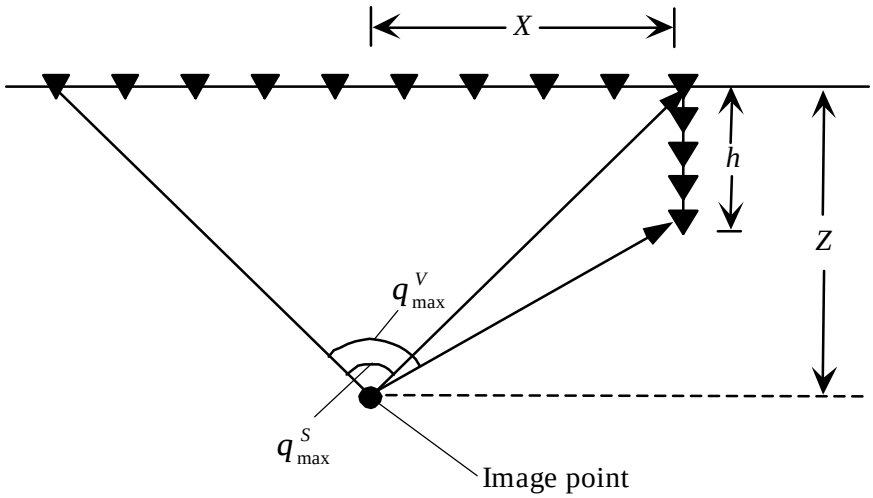

Figure 68. Schematic representation of raypaths reflected from an image point at a depth Z. $q^{S}_{\max}$ is the maximum angle of reflection for the surface array and $q^{V}_{\max}$ is the maximum angle of reflection for the vertical cable.

spacing is increased to 833 m, inadequate sampling density with respect to cable spacing results (green line, Figure 69). Superior vertical cable coverage is obtained by using 8 cables spaced every 357 m (blue line, Figure 69).

We can also determine the sampling criteria assuming we keep a constant distance between cables (500 m) and only vary the sampling within the cable for a cable length of 500 m. Figure 70 shows the results of varying only the sampling within the cable. The black line represents the surface data using the parameters previously mentioned. The red line corresponds to equivalent VC data using 17 receivers with a 31 m interval. The blue line is obtained by sampling every 12.5 m along each cable. The

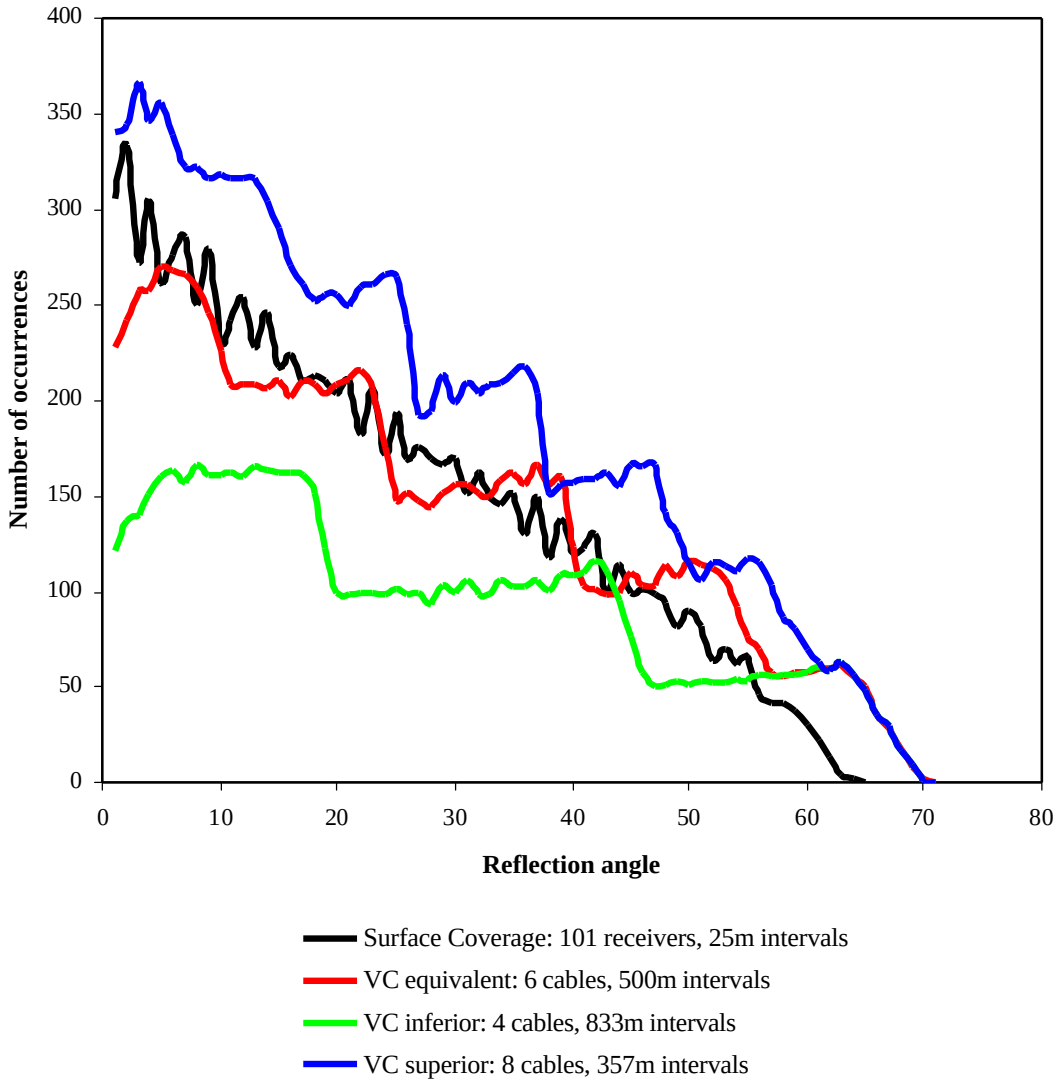

Figure 69. Angular coverage for an image point at a depth of 2000 m and simulating 101 shots spaced every 25 m for surface array and vertical arrays. For this experiment, only vertical cable spacing was varied. The receiver spacing along the vertical cables was constant, 17 receivers spaced every 25 m, and the vertical cable length was no longer than 500 m for any simulation.

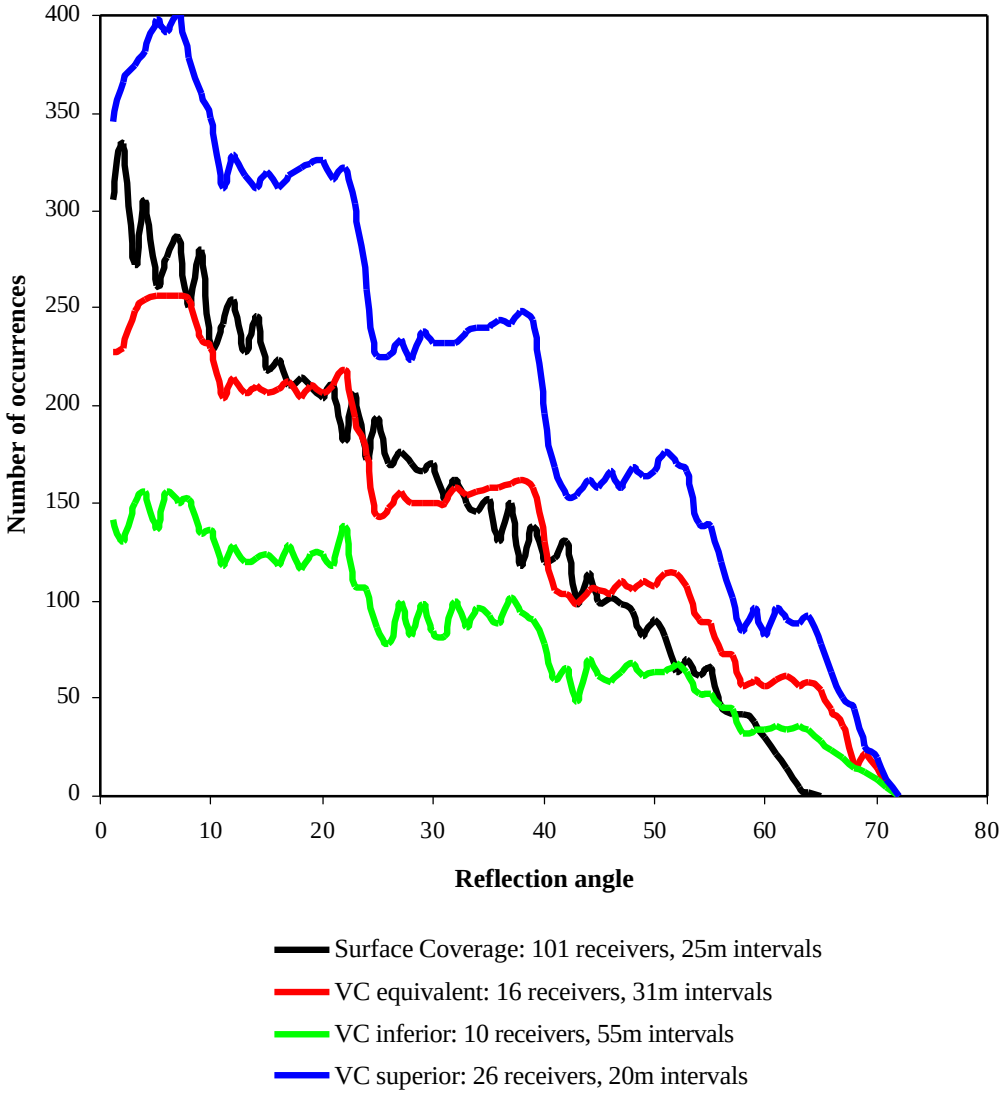

Figure 70. Angular coverage for an image point at a depth of 2000 m and simulating 101 shots spaced every 25 m for surface array and vertical arrays. For this experiment, the maximum vertical cable depth was 500 m and the cable spacing was constant, 6 cables at 500m intervals, while the sampling within cables varied.

green line is obtained by sampling every 50 m along each cable. The stair-step appearance of the VC data is attributed to the gap between cables. The results show we can achieve more superior imaging resolution than surface surveys with a 500 m cable interval and sampling densely along each cable.

CONCLUSIONS

Land seismic surveys may turn out to be the real beneficiary of VC technology. We have demonstrated its ability to overcome traditional land surface seismic problems like ground roll and statics. Correctly sampled VC surveys obtain equivalent or higher quality data than surface surveys and increase imaging resolution. Cable intervals of 500 m can achieve superior imaging with proper sampling within the cables. Thus, VC may be a cost-effective method for onshore acquisition.

CHAPTER VI

SUMMARY AND CONCLUSIONS

Vertical cable seismic surveying provides an alternative method for acquiring high quality seismic data in both the marine and land environment.

In the marine setting, we find that the data quality is consistent with traditional towed-streamer data quality. However, problems of acquiring data using towed-streamers in areas congested by drilling platforms or production facilities are overcome using vertical cables. Furthermore, since the current imaging algorithms for vertical cable data use either the primaries or the receiver ghosts of primaries, we demonstrate the inverse scattering method proposed by Ikelle (2001) to preserve either primaries only or receiver ghosts of primaries only.

On land, vertical cables have a larger impact. We have demonstrated that surface seismic problems such as ground roll, guided waves and statics can be almost entirely avoided using vertical cables. Moreover, vertical cable surveying is naturally suited for multi-component acquisition and time-lapse surveying because the receivers can be permanently placed in the subsurface.

We have also demonstrated that the resolution of vertical cable data, in both the marine and land scenarios, can be superior to that of surface seismic data. For instance, by using vertical cables of no more than 500 m in length and a 500 m cable spacing, we can achieve superior resolution compared to surface seismic data for an image point, horizontal reflector or dipping reflector.

REFERENCES

Anstey, N.A., 1966, The sectional auto-correlogram and the sectional retro-correlogram-part 1: Geophysical Prospecting, **14**, 389-411.

Anstey, N.A. and Newman, P., 1966, The sectional retro-correlogram and the sectional retro-correlogram-part 2: Geophysical Prospecting, **14**, 411-426.

Bayliss, A., Jordan, R.E., LeMesurier, B.J., and Turkel, E., 1986, A fourth-order accurate finite-difference scheme for the computation of elastic waves: Bull. Seis. Soc. Am., **76**, 1115-1132.

Carvalho, F.M. and Weglein, A.B., 1991, Examples of a nonlinear inversion method based on the T matrix of scattering theory: Application to multiple suppression: Soc. Expl. Geophys., Expanded Abstracts, 1319-1322.

Cerjan, C.D., Kosloff, D., Kosloff, R. and Reshef, M, 1985, A nonreflecting boundary condition for discrete acoustic and elastic wave equations: Geophysics, **50**, 705-708.

Chapman, C.H., 1971, On the computation of seismic ray travel times and amplitudes: Bulletin of Seismological Society of America, **61**, 1267-1274.

Clayton, R. and Engquist, B., 1977, Absorbing boundary conditions for acoustic and elastic wave equations: Bulletin of the Seismological Society of America, **71**, 1529-1540.

Dablain, F.A., 1986, The application of higher-order differencing to the scalar wave equation: Geophysics, **51**, 54-66.

Frasier, C.W., 1970, Discrete time solution of plane *P-SV* waves in a plane layered medium: Geophysics, **35**, 197-218.

Guimaraes, M.G, Sekkaran, K.K., Sukup, D., and Krail, P. 1998, 3-D pre-stack depth migration of vertical cable data over SEG/EAGE physical model: Soc. Expl. Geophys. Expanded Abstracts, 1182-1186.

Havig, S.O. and Krail, P.M., 1996, Vertical cable seismic applications: World Oil, **217**, 72.

Ikelle, L.T., Diet, J.P., Tarantola, A., 1986, Linearized inversion of multioffset seismic reflection data in the omega-k domain: Geophysics, **51**, 1266-1276.

Ikelle, L.T., and Weglein, A,B., 1996, Attenuation of free-surface multiples in multi-offset Walkaway VSP data: Jrnl. Seis. of Expl., **5**, 363-378.

Ikelle, L.T., Roberts, G., and Weglein, A.B., 1997, Source signature estimation based on the removal of the first-order multiples: Geophysics, **62**, 1904-1920.

Ikelle, L.T., 1999, Using even terms of the scattering series for deghosting and multiple attenuation of OBC data: Geophysics, **64**, 579-592.

Ikelle, L.T., Min, J., and Spears, H., 1999a, Multi-shooting for simulating seismic surveys: Application to 3-D finite-difference modeling: CASP, **1**, 263-272.

Ikelle, L.T., Walsh, J.R., and Min, J., 1999b, Inverse scattering multiple attenuation (ISMA): Preprocessing for the shallow-water seismic case: CASP, **1**, 167-175.

Ikelle, L.T. and Wilson, R.J., 1999, Potential impacts of vertical cable (VC): The Leading Edge, **18**, 1154-1157.

Ikelle, L.T., 2001, Attenuating primaries and free-surface multiples of vertical cable (VC) data while preserving receiver ghosts of primaries: Geophysics, **66**, 953-963.

Kelly, K.R., Ward, R.W., Treitel, S., and Alford, R.M., 1976, Synthetic seismograms: A finite-difference approach: Geophysics, **41**, 2-27.

Krail, P.M., 1994, Vertical cable as a subsalt imaging tool: The Leading Edge, 885-887.

Krail, P.M., 1997, Vertical cable marine seismic acquisition, Offshore Technology Conference, Houston, Texas, 5-8 May, 347-355.

Lavender, A.R., 1988, Fourth-order finite-difference *P-SV* seismograms: Geophysics, **53**, 1425-1436.

Leach, P.E., 1999, Strathspey vertical-cable seismic survey, a North Sea first: Petroleum Geology of Northwest Europe, **5**, 1384-1398.

Madariaga, R., 1976, Dynamics of an expanding circular fault: Bulletin of the Seismological Society of America, **66**, 639-665.

Matson, K. and Weglein, A.B., 1996, Removal of elastic interface multiples from land and ocean bottom data using inverse scattering, Soc. Expl.Geophys. Expanded Abstracts, 1526-1529.

Samson, J.C. and Olson, J.V., 1981, Data-adaptive polarization filters for multi-channel geophysical data: Geophysics, **46**, 1423-1431.

Shieh, F.C. and Hermann, R.B., 1990, Ground roll: Rejection using polarization filters: Geophysics, **55**, 1216-1222.

Virieux, J., 1984, SH-wave propagation in heterogeneous media: Velocity-stress finite-difference method: Geophysics, **49**, 1933-1957.

Virieux, J., 1986, P-SV wave propagation in heterogeneous media: Velocity-stress finite-difference method: Geophysics, **51**, 889-901.

Ward, J.A., 1997, Towed streamer and vertical cable: A comparison of the two forms of seismic data acquired over Fuji Prospect, US Gulf of Mexico: Offshore, March 1997, 40-43.

Weglein, A.B., Gasparotto, F.A., Carvalho, P.M., and Stolt, R.H., 1997, An inverse Scattering series for attenuating multiples in seismic reflection data: Geophysics, **62**, 1975-1989.

VITA

Ryan Justin Wilson was born in 1974 in Houston, Texas. In 1999, he received his B.S. in hydrogeology from Western Michigan University, Kalamazoo, Michigan. His permanent mailing address is: 8948 Sunset Park Lane, Conroe, TX 77302. He currently works for Anadarko Petroleum Corporation in Houston, TX.